



Flows in foams: The role of particles, interfaces and slowing down in microgravity

Pavel Yazhgur

► To cite this version:

Pavel Yazhgur. Flows in foams: The role of particles, interfaces and slowing down in microgravity. Soft Condensed Matter [cond-mat.soft]. Université Paris Saclay (COmUE), 2015. English. NNT: 2015SACLS055 . tel-01239898

HAL Id: tel-01239898

<https://theses.hal.science/tel-01239898>

Submitted on 8 Dec 2015

HAL is a multi-disciplinary open access archive for the deposit and dissemination of scientific research documents, whether they are published or not. The documents may come from teaching and research institutions in France or abroad, or from public or private research centers.

L'archive ouverte pluridisciplinaire **HAL**, est destinée au dépôt et à la diffusion de documents scientifiques de niveau recherche, publiés ou non, émanant des établissements d'enseignement et de recherche français ou étrangers, des laboratoires publics ou privés.

THÈSE DE DOCTORAT
DE
L'UNIVERSITÉ PARIS-SACLAY
PRÉPARÉE À
L'UNIVERSITÉ PARIS-SUD

LABORATOIRE DE PHYSIQUE DES SOLIDES

ECOLE DOCTORALE N°564
PHYSIQUE EN ÎLE-DE-FRANCE

SPÉCIALITÉ DE DOCTORAT: PHYSIQUE

Par

Pavel Yazhgur

**Flows in foams:
The role of particles, interfaces
and slowing down in microgravity**

Thèse présentée et soutenue à Orsay, le 27 octobre 2015

Directeur de thèse : Mme. Dominique Langevin Directeur de Recherche (LPS)

Composition du jury:

Président du jury:	Mme. Brigitte Pansu	Professeur (LPS)
Rapporteurs:	M. Benjamin Dollet	Chargé de recherche (Université Rennes 1)
	M. Hugues Bodiguel	Professeur (Grenoble-INP)
Examineurs:	Mme. Anniina Salonen	Maître de Conférence (LPS)
	M. Christophe Delaroche	Responsable du programme Science de la Matière en Microgravité (CNES)

Titre: Les écoulements dans les mousses: le rôle des particules, des interfaces et de la microgravité

Mots clés: Mousse, drainage, microgravité

Résumé Les mousses liquides sont des dispersions des bulles dans l'eau et elles sont largement utilisées dans un grand nombre de procédés technologiques et d'applications commerciales. Dans ma thèse, je me concentre sur les différents problèmes concernant les propriétés des mousses aqueuses et en particulier les écoulements gravitationnels dans les mousses.

Les mousses contiennent une grande quantité d'interfaces couvertes par des molécules amphiphiles, et l'échange des tensioactifs entre l'interface et la phase volumique joue un rôle important pour la génération et la stabilité des mousses. Donc, mon premier projet a été d'étudier la dynamique d'adsorption de systèmes modèles aux interfaces air/eau. Les résultats obtenus nous ont aidés à comprendre comment l'adsorption lente des tensioactifs lors de la génération de la mousse peut influencer la mobilité des interfaces et changer le drainage de la mousse. Pour étudier les différents aspects de la physique de la mousse à l'échelle des bulles, des mousses pseudo-bidimensionnelles (des monocouches des

bulles serrées entre deux plaques) sont largement utilisées. Dans ma thèse un modèle pour décrire la géométrie d'une mousse pseudo-bidimensionnelle a été introduit, cette description a été utilisée pour modéliser les conductivités électriques et hydrauliques de ces mousses. Dans certaines applications (par exemple, dans les industries du papier et de la peinture) la formation de la mousse peut causer de graves problèmes et des agents antimoussants appropriés sont utilisés. Dans ma thèse l'influence de la gravité sur l'efficacité antimoussante des gouttes d'huile de silicone a été étudiée expérimentalement en utilisant des vols paraboliques. Les résultats montrent que les particules antimoussantes ont besoin de la gravité pour être transportées d'une manière efficace, et la microgravité rend les antimousses très efficaces pratiquement inutiles. Etant initialement motivé par le transport des particules dans les mousses, j'ai également examiné la sédimentation des particules solides dans les capillaires de verre verticaux et inclinés.

Title: Flows in foams: The role of particles, interfaces and slowing down in microgravity

Keywords: Foam, drainage, microgravity

Abstract Liquid foams are dispersions of bubbles in water and they are widely used in a large number of technical processes and commercial applications. In the present thesis I focus on different problems concerning properties of aqueous foams and especially gravity-driven flows in foams.

Foams contain a large quantity of interfaces covered by surfactant molecules and the surfactant exchange between bulk and interface plays a crucial role for foam generation and stability. So my first project was to study the adsorption dynamics of model surfactant systems at air/water interfaces. The obtained results helped us to understand how the slow surfactant adsorption during foam generation can influence the mobility of interfaces and change foam drainage. To study different aspects of foam physics at the bubble scale simpli-

fied quasi-2D foams (monolayers of bubbles squeezed between two plates) are widely used. In this thesis a model to describe the geometry of a quasi-2D foam was introduced, this description was used to model the electrical and flow conductivities of such foams. In some applications (for example, in the paper and paint industries) foam formation can cause serious problems and suitable antifoaming agents need to be used. In my thesis the influence of gravity on the antifoaming efficiency of silicone oil droplets has been experimentally studied using parabolic flights. The results show that antifoam particles need gravity to be efficiently transported, and microgravity can render highly efficient antifoam practically useless. Being initially motivated by particle transport in foams, I have also looked at the sedimentation of solid particles in vertical and inclined glass capillaries.

Acknowledgements

I am eternally grateful to my supervisor Dr. Anniina Salonen for her continuous support and patience during the production of this work. It was a honour for me to be her first PhD student. My very special thanks go to other members of MOUS group: Dominique Langevin, Emmanuelle Rio and Wiebke Drenckhan - without them I could never finish this work. I am also grateful to the engineers of MOUS group, I would like to thank Clément Honorez for his support in using Foamscan and Delphine Hannoy for her help with performing surface tension measurements.

I would like to thank Florence Rouyer, Franck Pigeonneau and Hervé Caps for fruitful scientific discussions about foam physics. I am also very thankful to Sascha Heitkam for the help in the Matlab simulations and Juho Lintuvuori and Giuseppe Foffi for their help in understanding of particle sedimentation hydrodynamics.

I thank all my lab mates who have contributed immensely to my time at LPS. I would also like to say thanks to all undergraduate students who helped me to accomplish this work: Mélanie Michaud, Bora Lim, Jean Berthou, Zheng Feng, Lydia Boudergui, Jérôme Hardoüin and Justine Robin.

I would like to thank all administrative and technical staff of LPS and especially Vincent Klein for his indispensable aid in preparation and performing of parabolic flight experiments.

My warmest thanks go, last but not least, to my parents who always support me and encourage me with their best wishes.

I acknowledge the financial support from French space agency (CNES) and Doctoral School "Ecole Doctorale N°564: Physique en Ile-de-France".

Introduction

Liquid foams are dispersions of bubbles in water and they are widely used in a large number of technical processes and commercial applications. Their high surface to volume ratio makes them particularly attractive for mass transfer operations. The most important example is froth flotation used to separate the minerals in the ore, such as copper or lead, from the gangue. Creating foam is a very efficient way to increase the liquid viscosity such that the system acquires the mechanical behaviour of solids. These are the properties that make foams so attractive for cosmetic and food products. A sufficiently elastic foam with finite yield stress slowly flows in the gravity field and can be employed to cover vertical surfaces, for example, in shaving foams. The high viscosity of foams is useful for displacing oil from porous media in enhanced petroleum recovery. Because the liquid content in foams can be relatively low, their use allows to reduce the amount of active ingredients without reducing their effect. This effect is used in decontamination treatments, for example, cleaning foams are exploited in the decommissioning of a nuclear power station. The liquid foams can be solidified to get light-weight materials which can be used as excellent sound and thermal insulators.

In view of the numerous applications a fine control of foam stability and foam properties, such as bubble size, liquid fraction, yield stress, is required. Unfortunately, foams are thermodynamically unstable and are destroyed through various mechanisms, making the generation of stable foam with the desired properties a hard task. Among the different destabilising effects, gravity-driven drainage is one of the most important. The drainage reduces the liquid content at the top and accumulates it at the bottom. The resulting drier foam at the top is also more unstable with respect to other destabilisation mechanisms, such as coalescence, (the rupture of a film between two adjacent bubbles) or coarsening (the exchange of gas between bubbles due to a pressure difference). Liquid content variation also creates gradients in optical and mechanical foam properties, which are often unacceptable in practical applications. It is no exaggeration to say that the slowing down of drainage is a key step in the generation of stable uniform foams.

The example of drainage shows that gravity is crucially important for foams. In the present thesis I will focus on two problems concerning gravity-driven flows in foams: i) an influence of surface state on foam drainage during generation ii) sedimentation of microparticles confined in foams.

I will touch some aspects of surface state influence on the foam drainage. The mechanical response of interface depend on the chemical state of the interface and kinetic coefficients for surfactant adsorption/desorption. We will see how the change of surface mobility can affect the generation of foam. During foam generation fresh

interfaces are continuously created. To better understand how it can influence the foam mobility, we will also study surfactant adsorption/desorption kinetics.

A special attention will be paid to the hydrodynamic behaviour of foams modified by the presence of micrometric size particles in the liquid phase. Properties of foams doped with microparticles now attract a great scientific interest, different types of particles are considered: solid particles and oil droplets which can be deformed inside foams. The presence of particles can significantly augment the effective viscosity of the liquid phase and increase the stability of foam by slowing down drainage. Such ultra-stable foams are now widely used in industry, for example in cosmetics or food products (such as whipped cream). At the same time silicone oil emulsions or hydrophobic solid particles are widely used to destroy undesirable foams, for example, in paper and paint industry or in oil recovery. The efficient antifoaming agents used in industry can destroy huge volumes of foam within seconds.

Having a density different from water, particles migrate under the influence of the buoyancy forces. In the case of particles more dense than water this process is well-known as sedimentation, while for light oil droplets it is usually referred to as creaming. This buoyancy-driven flow results in the redistribution of particles changing the properties of the final product.

In this thesis I will mainly consider sedimentation of particles in foams, however all obtained results are directly valid for the creaming process. One can expect that the sedimentation of particles in foams is quite different from sedimentation in a bulk suspension. Foam can be considered as a network of liquid channels, having usually a size comparable with the particle diameter. So the particles flow in a confined geometry, where the influence of channel walls is crucially important. Also a coupling between the foam drainage and sedimentation of particles should be taken into account. As a result, depending on the precise formulation, the mixtures of bubbles and particles can separate within seconds or be stable during days.

To study a distribution of particles in foams I have chosen to use vertical quasi-2D foams (monolayers of bubbles squeezed between two plates). In my thesis I will show how the structural properties of quasi-2D foams can be studied by electrical conductivity measurements and image treatment. In future the obtained results can be applied to study foams with microparticles in the quasi-2D configuration.

Outline of the thesis Part I of this thesis includes a theoretical background necessary to understand the experimental results. This part consist of 4 chapters and represents different aspects of the thermodynamic of surfaces, structure of foams in equilibrium, hydrodynamics of particle sedimentation and foam drainage, the properties of oil-based antifoaming agents.

The preparation of the experimental samples and description of the experimental techniques with a brief overview of data treatment are detailed in Part II.

The part III consist of 5 chapters discussing experimental results for different problems studied in this thesis.

Chapter 6 deals with the kinetic of surfactant adsorption and desorption at water/gas interfaces. The understanding of surfactant adsorption dynamic is crucially important for a proper description of liquid flows in foams as it can change the mobility of interfaces by modifying their surface rheology properties. We will study

a desorption kinetic of ionic surfactant with an excess of salt using a bubble profile analysis tensiometry.

In Chapter 7 we will study a foam rising in a column due to buoyancy force. By varying physical chemistry of the foaming solution, we will see how the change of surface rheology can influence the liquid fraction of the foam during generation.

In Chapter 8 I will establish a new way of quasi-2D foam analysis by the use of electrical conductivity data and image treatment. This technique can be used in future to study quasi-2D foams with dispersed microparticles.

Chapter 9 presents an ongoing work concerning sedimentation of solid particles under confinement in glass capillaries. The last can imitate liquid channels in foams.

In Chapter 10 we will continue by considering the influence of antifoam globules transport on the foam destabilisation.

Chapter 11 concludes the thesis and suggests some ideas for future work.

Contents

Acknowledgements	2
Introduction	3
I Theoretical background	9
1 Thermodynamic of surfaces	10
1.1 Surface tension	10
1.2 Geometry of curved surfaces and Laplace law	10
1.3 The surface excess	12
1.4 Internal energy and mechanical definition of the surface tension . . .	14
1.5 Gibbs adsorption equation	16
1.6 Application of the Gibbs adsorption equation to ionic surfactants . .	17
1.7 Equations of state	19
1.8 Dynamics of adsorption	20
1.9 Surface rheology	23
2 Structure of foams	25
2.1 Introduction	25
2.2 Dry foams	28
2.3 Wet foams	30
2.4 Quasi-2D foams	31
3 Hydrodynamics of particles and foams	34
3.1 Introduction	34
3.2 Governing equations of fluid mechanics	35
3.3 Sedimentation of a single particle	38
3.4 Sedimentation of suspensions	39
3.5 Velocity fluctuations	41
3.6 Boycott effect	43
3.7 Rayleigh-Taylor instability	44
3.8 Foam drainage	46
3.9 Pressure gradient in the foam	47
3.10 Forced drainage	48
3.11 Modelling the permeability of a foam	49

4	Antifoaming agents	52
II	Materials and methods	56
5	Materials and Methods	57
5.1	Materials	57
5.2	Sample preparation	58
5.3	Surface tension measurements	58
5.4	Methods of foam generation and characterization	60
5.4.1	FoamScan	60
5.4.2	Measurement of the bubble size	60
5.4.3	Hele-Shaw cell	61
5.5	Parabolic flights	64
5.5.1	Principle of parabolic flights	64
5.5.2	The experimental set-up	65
5.6	Sedimentation in capillaries	67
III	Experimental results and discussion	72
6	Kinetics of surfactant desorption at air-water interface	73
6.1	Introduction	73
6.2	Experimental procedure	74
6.3	Results and discussion	77
6.3.1	Equation of state	77
6.3.2	Desorption kinetics	81
6.4	Conclusion	82
7	Generation of rising foams	84
7.1	Introduction	84
7.2	Experimental procedure	86
7.3	Theoretical background	86
7.4	Results and discussion	88
7.5	Conclusion	95
8	Electrical and flow conductivity of quasi-two-dimensional foams	97
8.1	Introduction	97
8.2	Geometry of quasi-2D foams	98
8.3	Electrical conductivity	104
8.4	Flow conductivity	109
8.5	Conclusion	111
9	Sedimentation of microparticles under confinement	112
9.1	Introduction	112
9.2	Results and discussion	112
9.2.1	Sedimentation in vertical capillaries	112

9.2.2	A closer look on the onset of sedimentation: Rayleigh-Taylor instability	116
9.2.3	Sedimentation in inclined capillaries: Boycott effect	117
9.3	Conclusion	119
10	Antifoaming agents in microgravity	121
10.1	Introduction	121
10.2	Results and discussion	121
10.3	Conclusion	125
11	General conclusion	127
A	Resumé substantiel de la thèse	130
A.1	Introduction	130
A.2	Contexte de la thèse	132

Part I

Theoretical background

Chapter 1

Thermodynamic of surfaces

1.1 Surface tension

In all fluids there exist attractive forces between molecules. Such forces have an electromagnetic nature and ensure the stability of the liquid phase. When two fluids with molecules A and B are in contact there exist two possibilities: the interaction A-A and B-B can be either weaker or stronger than A-B. In the first case fluids start to dissolve into each other and to form a mixed phase. It is only in the second case that two fluids with a distinct interface between them can co-exist. In this case the molecules have higher energy at the interface and tend to go deeper in the bulk. This implies that in the interfacial region there is an excess of free energy compared to the bulk. If the volume V , the temperature T and the number of molecules N are constant, the variation of the surface free energy with a change of interfacial area dA can be written as

$$dF_{V,T,N} = \gamma dA, \quad (1.1)$$

where γ is defined as the *surface tension*.

The surface tension can be considered as an energy required to create a unit area or as a force per unit length. The surface tension is always positive since otherwise the interface would be unstable. It is only defined at a scale that is large comparable to the size of molecules, so the interface can be treated as continuous.

1.2 Geometry of curved surfaces and Laplace law

If an interface is not flat, the surface tension induces normal forces which are compensated at equilibrium by the pressures on each side. The effect of curvature is purely geometric, it is generally assumed that it does not change the surface tension. We will see later how the position of the interface should be chosen to make this assumption valid.

At each point M on the interface we can introduce a system of coordinates XYZ such that the Z direction is normal to the surface. In these coordinates the interface $Z(X,Y)$ in the vicinity of the point M can be written using Taylor expansion in a

quadratic form

$$Z(X, Y) = [X, Y] \begin{bmatrix} \frac{\partial^2 Z}{\partial X^2} & \frac{\partial^2 Z}{\partial X \partial Y} \\ \frac{\partial^2 Z}{\partial X \partial Y} & \frac{\partial^2 Z}{\partial Y^2} \end{bmatrix} \begin{bmatrix} X \\ Y \end{bmatrix} + O(X^3, Y^3). \quad (1.2)$$

The curvature matrix consisting of second derivatives is symmetric and therefore can be diagonalised in the basis of eigenvectors. Calling X' and Y' the new orthogonal axes, we have a new equation for the surface

$$Z(X', Y') = [X', Y'] \begin{bmatrix} \frac{1}{2R_1} & 0 \\ 0 & \frac{1}{2R_2} \end{bmatrix} \begin{bmatrix} X' \\ Y' \end{bmatrix} + O(X'^3, Y'^3), \quad (1.3)$$

which defines the principal radii of curvature R_1 and R_2 . Note that the signs of R_1 and R_2 depend on the arbitrary choice of the normal to the interface. An alternative description of the local curvature is given in terms of two invariants of the curvature matrix. The trace $R_1^{-1} + R_2^{-1} = 2H$ defines the mean curvature H , while the determinant $(R_1 R_2)^{-1} = K$ defines the Gaussian curvature K .

Let us now consider a surface element $dS = dx_1 dx_2$ as illustrated in Figure 1.1. The surface divides two phases α and β with pressures P^α and P^β , respectively. Orienting the normal to the surface towards the phase β we set $dx_1 = R_1 d\theta_1$ and $dx_2 = R_2 d\theta_2$. Then the balance of forces in the normal direction yields

$$\Delta P dx_1 dx_2 - \gamma dx_1 d\theta_2 - \gamma dx_2 d\theta_1 = 0, \quad (1.4)$$

where $\Delta P = P^\alpha - P^\beta$ is a pressure difference between the interior and exterior

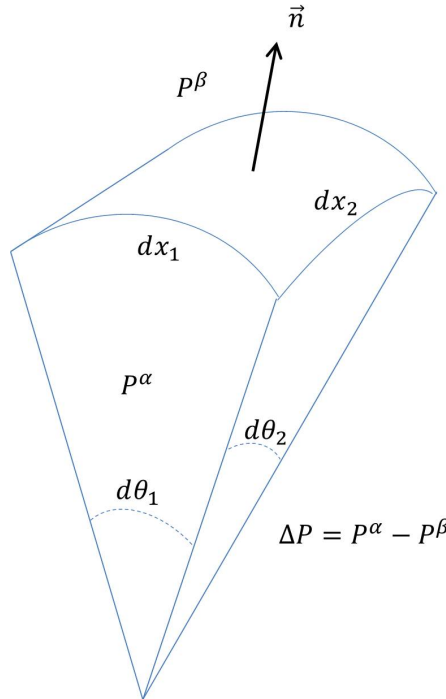


Figure 1.1: Element of the curved surface dS

sides. So we easily conclude

$$\Delta P = \gamma \left(\frac{1}{R_1} + \frac{1}{R_2} \right) = 2\gamma H. \quad (1.5)$$

This equation is called Young-Laplace law, after Pierre-Simon de Laplace (1749-1827) and Thomas Young (1773-1829), or sometimes just Laplace law.

1.3 The surface excess

In the proximity of an interface between two phases all parameters describing the system such as the concentration of components or the internal energy density rapidly change along the axis perpendicular to the interface. To treat such systems different approaches have been developed. The most well-known are the Gibbs and Guggenheim models (see Figure 1.2). In the first one the two phases α and β are thought to be separated by an infinitely thin layer σ , called the *Gibbs dividing plane*. The Guggenheim approach takes an extended interfacial region with a finite thickness and volume. In the following discussion we will adhere to the Gibbs convention as it is more useful for most applications.

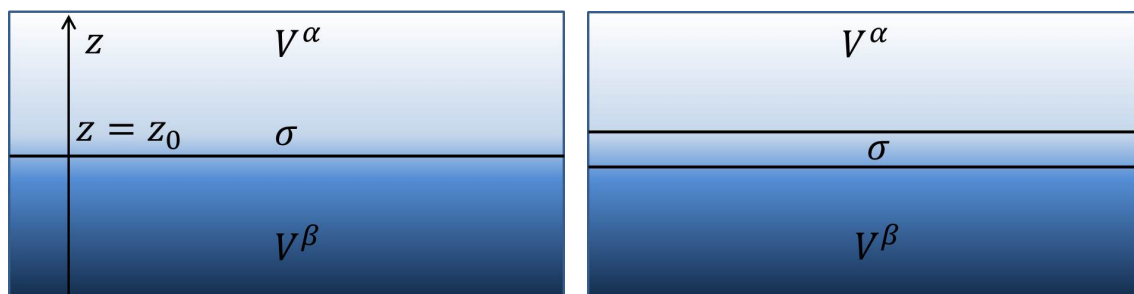


Figure 1.2: On the left: In the Gibbs convention the two phases α and β are separated by an infinitely thin interface σ . The axis z is perpendicular to the interface. On the right: In the Guggenheim approach the interface is treated as a region σ with finite thickness and volume

In the Gibbs model the real system is compared with the corresponding idealized one, where the densities of all extensive parameters are constant everywhere in each phase and equal to the bulk values, but undergo an abrupt jump at the dividing interface. The interface is ideally thin, so the total volume is equal to the sum of individual phase volumes

$$V = V^\alpha + V^\beta. \quad (1.6)$$

All other extensive quantities can be written as a sum of three components: one of the ideal phase α , one of the ideal phase β and an excess quantity attributed to the surface σ . For example, for the internal energy U , the entropy S and the number of molecules of the i -th substance N_i one has

$$U = u^\alpha V^\alpha + u^\beta V^\beta + U^\sigma, \quad (1.7)$$

$$S = s^\alpha V^\alpha + s^\beta V^\beta + S^\sigma, \quad (1.8)$$

$$N = c_i^\alpha V^\alpha + c_i^\beta V^\beta + N_i^\sigma, \quad (1.9)$$

where u , s and c correspond to the densities of internal energy, entropy and concentration of i -th substance. We can also define an excess of molecules per unit area which is called the *surface concentration*

$$\Gamma_i = \frac{N_i^\sigma}{A}. \quad (1.10)$$

For a planar interface when the concentration changes only along the axis z perpendicular to the interface the surface concentration can be explicitly written as

$$\Gamma_i = \int_{-\infty}^{z_0} (c_i(z) - c_i^\alpha) dz + \int_{z_0}^{\infty} (c_i(z) - c_i^\beta) dz, \quad (1.11)$$

where $c_i(z)$ is a continuous concentration profile and $z = z_0$ is the position of the interface.

The surface concentration introduced by Equation 1.10 depends on the position of the dividing interface. In Figure 1.3 a typical profile for liquid-vapour interface of pure liquid is shown. The density decreases continuously from the high density of the bulk liquid to the low density of the vapour. One can see that by moving the dividing plane Γ_i can be made positive or negative. In the case of a planar interface we have from Equation 1.11

$$\frac{\partial \Gamma_i}{\partial z_0} = c_i^\beta - c_i^\alpha. \quad (1.12)$$

It shows that the bigger the difference between the bulk concentrations in two phases, the more sensitive Γ_i is to the position of the dividing plane.

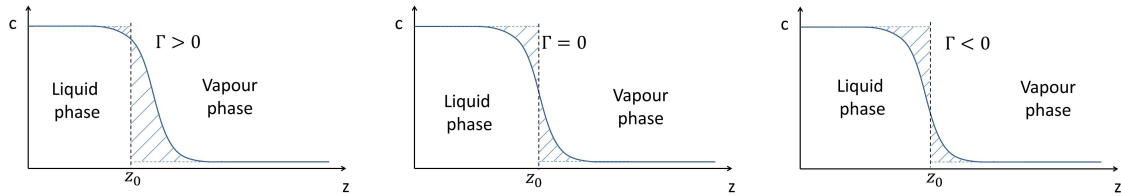


Figure 1.3: Dependence of the surface excess Γ on the position of the Gibbs dividing plane

There exist different methods to fix the position of the dividing plane. For two- or multi-component liquids such as a solvent with dissolved substances the most widely used one is a concept of relative adsorptions offered by Gibbs. Substituting $V^\alpha = V - V^\beta$ in Equation 1.9 we can write

$$N_i^\sigma = N_i - c_i^\alpha V + (c_i^\alpha - c_i^\beta) V^\beta. \quad (1.13)$$

Writing a similar equation for component 1 which is taken to be the solvent and eliminating V^β we get

$$N_i^\sigma - N_1^\sigma \frac{c_i^\alpha - c_i^\beta}{c_1^\alpha - c_1^\beta} = N_i - c_i^\alpha V - (N_1 - c_1^\alpha V) \frac{c_i^\alpha - c_i^\beta}{c_1^\alpha - c_1^\beta}. \quad (1.14)$$

The right-hand side of the equation does not depend on the position of the Gibbs dividing plane and thus, also, the left-hand side is invariant. We divide this quantity by the surface area and obtain the invariant *relative adsorption* of component i with respect to component 1

$$\Gamma_i^{(1)} = \Gamma_i - \Gamma_1 \frac{c_i^\alpha - c_i^\beta}{c_1^\alpha - c_1^\beta}. \quad (1.15)$$

If we choose the position of the dividing plane such that $\Gamma_1 = 0$, the relative adsorption of i -th component is just equal to its interfacial excess

$$\Gamma_i^{(1)} = \Gamma_i. \quad (1.16)$$

The relative adsorption does not depend on the choice of the dividing plane and as we will see later it can be determined experimentally.

1.4 Internal energy and mechanical definition of the surface tension

Let us consider a reversible process in our two-phase system. Using Equation 1.7 a variation of the internal energy can be split into three parts

$$dU = dU^\alpha + dU^\beta + dU^\sigma, \quad (1.17)$$

where dU^α and dU^β stand for the variations of the internal energies for the idealized phases α and β , while dU^σ is an excess energy showing a difference between idealized and real systems. We assume that the system is always in thermal and chemical equilibrium, so the temperature T and the chemical potential μ_i are constant everywhere. Then, according to the first and second principles of thermodynamics, we write

$$dU^\alpha = TdS^\alpha - P^\alpha dV^\alpha + \sum_i \mu_i dN_i^\alpha, \quad (1.18)$$

$$dU^\beta = TdS^\beta - P^\beta dV^\beta + \sum_i \mu_i dN_i^\beta, \quad (1.19)$$

$$dU^\sigma = TdS^\sigma + \sum_i \mu_i dN_i^\sigma + \delta W^\sigma. \quad (1.20)$$

Here δW^σ is an additional mechanical work related with the deformation of the surface layer. In the case of isotropic fluid-fluid interfaces it can be reasonably assumed that this excess work is proportional to the variation of the area dA and can be written as $\delta W^\sigma = \gamma dA$, where γ is the surface tension.

1.4. INTERNAL ENERGY AND MECHANICAL DEFINITION OF THE SURFACE TENSION

We will illustrate it in the simple case of a planar interface. We introduce Cartesian coordinates such that the axis z is perpendicular to the surface (see Figure 1.2). Assuming that we can define a continuous stress tensor in the system, the total work of deformation of a given volume V can be written as

$$\delta W = -P^\alpha dV^\alpha - P^\beta dV^\beta + \delta W^\sigma = \iiint_V \sigma : \delta \epsilon dV, \quad (1.21)$$

where σ and ϵ are Cauchy stress and strain tensors, respectively. We consider an isotropic fluid at rest, so all non-diagonal elements of the stress tensor are zero. From the mechanical equilibrium we can conclude that the normal component of the stress is constant in the whole system, so $P^\alpha = P^\beta = P_N = -\sigma_{zz}$. Due to the symmetry of the system the tangential components are equal at each point $\sigma_{xx} = \sigma_{yy} = -P_T$. The tangent pressure P_T depends on the coordinate z . Far away from the interface it coincides with P_N , but close to the dividing plane the symmetry is broken and normal and tangent pressures are different. Then the mechanical work can be written as

$$\begin{aligned} \delta W &= - \iiint_V P_N (\delta \epsilon_{xx} + \delta \epsilon_{yy} + \delta \epsilon_{zz}) dV + \iiint_V (P_N - P_T(z)) (\delta \epsilon_{xx} + \delta \epsilon_{yy}) dV = \\ &= -P \delta V + \delta A \int (P_N - P_T(z)) dz. \end{aligned} \quad (1.22)$$

The integral on the right side gives us a mechanical definition of the surface tension for planar interface:

$$\gamma = \int_{-\infty}^{\infty} (P_N - P_T(z)) dz. \quad (1.23)$$

As we have discussed early the surface tension of the stable system should be positive. This means that the integral in the right part is always positive. The mechanical definition of γ shows that it does not depend on the position of the dividing plane. However this equation is not very useful for calculating the surface tension as it is usually very difficult to define $P_T(z)$.

In the case of curved interfaces the mechanical description of the system is much more complicated. The pressures inside two phases P^α and P^β are not equal as follows from the Young-Laplace law. In this case the excess stress δW^σ depends on the position of the dividing plane and in general it is not simply proportional to area variation. For example, in a case of a spherical surface δW^σ can be written for a given radius of dividing interface r^σ as

$$\delta W^\sigma(r^\sigma) = \gamma(r^\sigma) dA + A(r^\sigma) \frac{\partial \gamma}{\partial r^\sigma} dr^\sigma. \quad (1.24)$$

It was shown by Gibbs that there exists a unique choice of dividing plane for which $\partial \gamma / \partial r^\sigma = 0$ and δW^σ is simply equal to γdA . It is only for this choice of dividing plane that the surface tension can be interpreted as a force stretching the interface and the Young-Laplace equation is valid in the form 1.5.

1.5 Gibbs adsorption equation

The excess energy U^σ is an extensive property. Then from the Euler's homogeneous function theorem we can write for the excess internal energy

$$U^\sigma = TS^\sigma + \sum_i \mu_i N_i^\sigma + \gamma A. \quad (1.25)$$

Subtracting from Equation 1.20 the differential of Equation 1.25 one arrives at the surface equivalent of the bulk Gibbs-Duhem relation

$$S^\sigma dT + \sum_i N_i^\sigma d\mu_i + A d\gamma = 0, \quad (1.26)$$

or dividing through by the surface area A this can be written in the form of the *Gibbs adsorption equation*

$$s^\sigma dT + \sum_i \Gamma_i d\mu_i + d\gamma = 0, \quad (1.27)$$

where s^σ is a surface density of excess entropy.

At constant temperature it can be simplified to

$$d\gamma = - \sum_i \Gamma_i d\mu_i. \quad (1.28)$$

The simplest application of the Gibbs adsorption isotherm is a system of two components, a solvent 1 and a solute 2. Defining the ideal interface such that $\Gamma_1 = 0$ we get

$$d\gamma = -\Gamma_2^{(1)} d\mu_2. \quad (1.29)$$

In thermodynamic equilibrium the chemical potential is constant everywhere. In the bulk it can be written as

$$\mu_2 = \mu_2^0 + RT \ln(a/a_0), \quad (1.30)$$

where a is activity and μ_2^0 is a standard chemical potential corresponding to a standard activity a_0 . Then the Gibbs adsorption equation can be written as

$$\Gamma_2^{(1)} = -\frac{a}{RT} \left(\frac{\partial \gamma}{\partial a} \right)_{T, \Gamma_1=0}. \quad (1.31)$$

For a solute the standard state is usually chosen to correspond the hypothetical state where the solute has a concentration of 1 mol/l but exhibits an infinite-dilution behaviour. Then in dilute solutions the activity is approximately equal to the concentration $a \approx c$ and the Gibbs adsorption equation can be expressed as

$$\Gamma_2^{(1)} \approx -\frac{c}{RT} \left(\frac{\partial \gamma}{\partial c} \right)_{T, \Gamma_1=0} = -\frac{1}{RT} \left(\frac{\partial \gamma}{\partial \ln c} \right)_{T, \Gamma_1=0}. \quad (1.32)$$

This equation directly tells us that when a solute is enriched at the interface ($\Gamma_2^{(1)} > 0$), the surface tension decreases when the solute concentration in the bulk increases. Such solutes are called *surfactants* or surface active agents. Such molecules play an important role in many practical applications and products, such as cleaning, wetting, dispersing, emulsifying, foaming and anti-foaming agents. They are generally amphiphilic organic compounds, meaning that the surfactant molecules contain both hydrophobic regions (known as surfactant tails) and hydrophilic regions (known as surfactant headgroups), the typical representation of the surfactant structure is shown in Figure 1.4. The surface tension is lowered with an addition of surfactant until a concentration, the *critical micelle concentration* (CMC), is reached at which the surface is saturated with amphiphilic molecules. Above this concentration the added surfactant molecules form aggregates, *micelles*, in the bulk and the surface tension becomes almost constant.

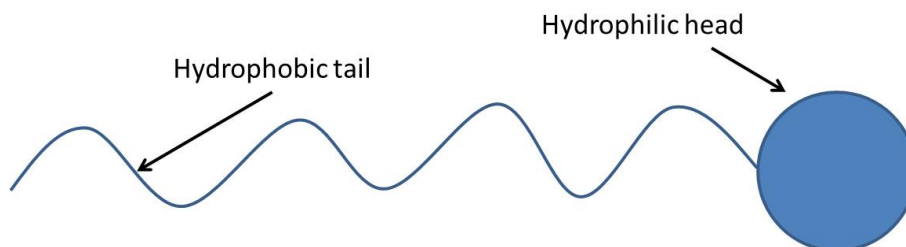


Figure 1.4: Structure of a surfactant molecule

When a solute avoids the interface ($\Gamma_2^{(1)} < 0$), the surface tension increases by addition of the solute. Such solutes are said to be surface inactive. Classic examples of surface inactive substances are inorganic salts. Their surface activity $\frac{\partial \gamma}{\partial c}$ is typically very small; they do not change the surface tension significantly.

The Gibbs adsorption equation is of great importance, as it allows the relative adsorption to be directly determined by measuring the surface tension versus the bulk concentration. By taking the derivative of surface tension γ by the logarithm of bulk concentration $\ln c$ the surface concentration $\Gamma_2^{(1)}$ can be estimated. Using this method, the surface equation of state $\gamma(\Gamma_2^{(1)})$ (equilibrium surface tension as a function of the surface concentration) can be acquired and eventually compared with theoretical models.

1.6 Application of the Gibbs adsorption equation to ionic surfactants

The Gibbs adsorption equation can be generalized to ionic surfactants, either with or without added electrolyte. For the sake of clarity we will consider the simplest possible case of a 1:1 ionic surfactant (like CTAB) and a 1:1 inorganic salt (like NaBr) with the same counterion as the surfactant. Both are strong electrolytes and completely dissociate in water giving 3 types of ions. The surfactant dissociation is given as



where R^+ is a surface active ion which can adsorb on the interface and M^- is a counterion which may bind to the adsorbed surfactant ion. Similarly the dissociation for the supporting electrolyte gives



where X^+ is an indifferent coion.

Such solution is intrinsically non-ideal due to long range electrostatic forces. The non-ideality leads to the change of activity coefficients $f_i = a_i/c_i$ which can be modelled using the Debye-Hückel theory. The adsorption of surfactant ions also creates a surface charge and leads to the formation of a double layer. The last can be described by Gouy-Chapman theory. The presence of the double layer significantly complicates the theoretical description. The classical approach to simplify the calculations is to treat the system as pseudo-nonionic. In this case only dissociation of molecules is taken into account, all electrostatic effects are ignored. This approach is valid if the thickness of the double layer is sufficiently small. If the presence of the double layer can be neglected, the solution can be considered as electroneutral at any point and the electrical potential is constant everywhere. Then for the diluted solution Equation 1.28 can be expanded over all ionic species in the ideal solution

$$d\gamma = -RT(\Gamma_{M^-}^{(1)} d \ln c_{M^-} + \Gamma_{R^+}^{(1)} d \ln c_{R^+} + \Gamma_{X^+}^{(1)} d \ln c_{X^+}). \quad (1.35)$$

The more accurate analysis shows that the key approximation allowing us to use concentrations instead of activities is not that the concentration of solutes is small $c \rightarrow 0$ but rather that the change in the activity coefficient with concentration will be negligible, $d \ln f / d \ln c \approx 0$ [1].

The electroneutrality of the interfacial region and the bulk phase gives us

$$c_{M^-} = c_{R^+} + c_{X^+}, \quad (1.36)$$

$$\Gamma_{M^-}^{(1)} = \Gamma_{R^+}^{(1)} + \Gamma_{X^+}^{(1)}. \quad (1.37)$$

Assuming that the adsorption of salt is negligible, Equations 1.35, 1.36 and 1.37 yield upon rearrangement

$$d\gamma = -RT\Gamma^{(1)}(d \ln(c_s + c) + d \ln c), \quad (1.38)$$

where $\Gamma^{(1)}$ is a relative surfactant adsorption, c and c_s are bulk concentrations of surfactant and salt, respectively.

Usually the concentration of salt is kept constant and a dependence of surface tension on the surfactant concentration is recorded. Then two important limiting cases can be considered. If the concentration of salt is much smaller than surfactant concentration $c_s \ll c$ Equation 1.38 reduces to

$$d\gamma = -2RT\Gamma^{(1)} d \ln c. \quad (1.39)$$

Of course, this expression is also valid for a solution of surfactant without added salt ($c_s = 0$).

If the concentration of salt is much bigger than surfactant concentration $c_s \gg c$ Equation 1.38 transforms into

$$d\gamma = -RT\Gamma^{(1)}d\ln c. \quad (1.40)$$

This equation coincides with the corresponding one for nonionic surfactants (See Equation 1.32). Generally it agrees well with the experiment because when c_s is large the main assumption of the pseudo-nonionic model is valid: the double layer is indeed very thin and charge of ions does not play a big role.

1.7 Equations of state

If we consider the surface as an individual 2D phase, which is generally valid for surfactant monolayers, we can introduce a concept of the surface chemical potential μ^s . Then the Gibbs adsorption equation 1.28 gives a relationship between adsorption Γ , surface tension γ and surface chemical potential μ^s . A surface equation of state relating surface tension γ and adsorption Γ can be obtained by integrating the Gibbs adsorption equation 1.28 using an appropriate expression for the surface chemical potential.

In the following discussion we will consider only the simplest case of nonionic surfactants but we will keep in mind that all derived equations can be used as well for the case of ionic surfactants with excess salt.

One of the first adsorption models was proposed by Irving Langmuir for ideal solutions and ideal interfaces. In the Langmuir model it is assumed that the surfactant forms a monolayer at the interface. The adsorbed surfactant monolayer may be viewed as a simple two-dimensional lattice in which the total number of sites represents the maximum number of surfactant molecules Γ_∞ which can geometrically fit on the surface. All interactions between adsorbed molecules are neglected, both interface and bulk are assumed to be ideal. Taking into account only the entropic effect of mixing, the chemical potential of an ideal surfactant monolayer can be written as (see [2] for more details)

$$\mu^s = \mu^{s^0} + RT \ln \left(\frac{\Gamma/\Gamma_\infty}{1 - \Gamma/\Gamma_\infty} \right). \quad (1.41)$$

By introducing Equation 1.41 into Equation 1.29 and performing integration, a link between surface tension and adsorption can be established

$$\gamma = \gamma_0 + RT\Gamma_\infty \ln(1 - \Gamma/\Gamma_\infty), \quad (1.42)$$

where γ_0 is a surface tension of the bare interface without surfactant. This surface equation of state is well-known as Szyszkowski equation. It is worth noting that Equation 1.42 is valid even out of the equilibrium between surface and a bulk phase, the only requirement is that the surface is in equilibrium with itself. In the case of surface/bulk equilibrium two additional relationship can be derived. First, the equality of bulk μ^b and surface μ^s chemical potentials gives us the Langmuir isotherm

$$\frac{\Gamma}{\Gamma_\infty} = \frac{Kc}{1 + Kc}. \quad (1.43)$$

In this equation the equilibrium constant is defined as $K = \frac{1}{c_0} \exp\left(\frac{\mu^{b^0} - \mu^{s^0}}{RT}\right)$, where μ^{b^0} is a standard bulk chemical potential corresponding to a standard concentration c_0 .

Substituting Equation 1.43 in Equation 1.42 one also derives a relationship between the equilibrium surface tension and surfactant bulk concentration

$$\gamma = \gamma_0 - RT\Gamma_\infty \ln(1 + Kc). \quad (1.44)$$

The Langmuir model is often used for its simplicity and it can qualitatively describe behaviour of the system. However it does not take into account the physics of molecular interactions in the monolayer and between the monolayer and the bulk solution. A more appropriate description of the system can be achieved by using the Frumkin model. In the Frumkin model the adsorbed monolayer is not assumed to be ideal, but rather non-ideal allowing for either net attractive or net repulsive interactions among head groups. Such interactions are supposed to occur only between neighbouring adsorbed surfactant molecules in a pair-wise fashion. An interaction energy term $w_{22}\Gamma/\Gamma_\infty$ should be added to the expression of the surface chemical potential 1.41. Then the Frumkin equation of state can be obtained

$$\gamma = \gamma_0 + RT\Gamma_\infty \left(\ln\left(1 - \frac{\Gamma}{\Gamma_\infty}\right) - \frac{A_F}{2} \left(\frac{\Gamma}{\Gamma_\infty}\right)^2 \right). \quad (1.45)$$

In the case of equilibrium between bulk and surface we can also write

$$\frac{\Gamma}{\Gamma_\infty} = \frac{Kc \exp(-A_F\Gamma/\Gamma_\infty)}{1 + Kc \exp(-A_F\Gamma/\Gamma_\infty)}, \quad (1.46)$$

where the interaction parameter A_F is given as

$$A_F = \frac{w_{22}}{RT}. \quad (1.47)$$

The interaction parameter A_F represents the energy of interactions between adsorbed surfactant molecules normalized by the thermal energy RT . The parameter A_F can be positive, reflecting net repulsive interactions which may occur between the charged surfactant head groups, or A_F can be negative, reflecting attractive interactions. When A_F is equal to 0, the Frumkin equation of state 1.45 reduces to the Langmuir one (see Equation 1.42).

More complicated and sophisticated models can be used to account for the interactions between the monolayer and the bulk. In the case of ionic surfactants more exact models take into account the presence of the double layer. The classical examples of such theories are the Davies and Frumkin-Davies isotherms. An overview of several other surface equations of state is given in [3–6].

1.8 Dynamics of adsorption

Alongside the surface properties at equilibrium, the time-scales of adsorption also matter in many industrial applications. Frequently they are even more important

than the equilibrium properties. Accordingly, intense attention has been paid to the research on the dynamic surface tension of surfactant solutions [5, 7]. If we introduce surfactants into a pure solution we observe a decrease in surface tension, but this is not instantaneous. In the absence of convection, the adsorption of the surfactant molecules from the bulk onto the interface is often described by two steps: diffusion of surfactant molecules from the bulk to the region close to interface (sub-surface) and transfer of surfactant molecules from the sub-surface to the interface overcoming the associated energy barrier. Depending on the characteristic times of diffusion t_{diff} and adsorption t_{ads} , either of these processes may control the dynamics.

Experimentally it is easier to measure the dynamic surface tension $\gamma(t)$, however theoretically we usually predict kinetic dependences of surface concentration $\Gamma(t)$. In the following consideration we assume that the surface equation of state linking Γ and γ is known and it is sufficient to predict $\Gamma(t)$.

Diffusion limited case In the diffusion-limited case, where $t_{diff} \gg t_{ads}$, the surfactants adsorb onto the interface much faster than they arrive by diffusion. A sub-surface region is depleted of surfactants compared to the bulk, and the local sub-surface concentration c_s is smaller than the bulk one c . The thickness of this region can be estimated as Γ/c and the typical timescale for diffusion controlled adsorption can be determined as

$$t_{diff} = \frac{\Gamma^2}{Dc^2}, \quad (1.48)$$

where D is the diffusion coefficient of the surfactants in the bulk phase.

A diffusion model for the adsorption of surfactant molecules onto an air/water interface has been developed by Ward and Tordai for a surface initially free of surfactant by solving the Fick's diffusion equation for the bulk liquid. The Ward-Tordai equation [8] predicts the time variation of the surface concentration Γ as

$$\Gamma(t) = \sqrt{\frac{D}{\pi}} \left(2c\sqrt{t} - \int_0^t \frac{c_s(\tau)}{\sqrt{t-\tau}} d\tau \right), \quad (1.49)$$

where t the ageing time of the interface and τ is the time variable. The first term represents the adsorption from the bulk, while the second term accounts for the desorption events occurring at long times. This equation is not explicit as c_s itself depends on Γ . Assuming that exchange of molecules between the surface and the sub-surface is much faster than the diffusion in the bulk, the surface region can be considered to be in equilibrium with the sub-surface at any time. In this case Γ and c_s can be linked via the appropriate adsorption isotherm, such as Equation 1.43 or 1.46.

At short times, before the surface concentration becomes sufficiently high, desorption is negligible and the Ward-Tordai equation simplifies to $\Gamma(t) \sim \sqrt{t}$. This relationship is very useful to check if surfactant adsorption is diffusion-controlled.

It was shown that diffusion models satisfactorily account for the adsorption kinetics of non-ionic surfactants [9, 10]. In the case of ionic surfactants with high concentrations of added electrolyte, the electrostatic repulsion from the charged surfactant molecules already present at the surface is screened, and therefore the

electrostatic adsorption barrier is suppressed. As a result, the adsorption behaviour is to that of non-ionic surfactants, i.e., diffusion controlled [11, 12].

Case limited by adsorption/desorption barrier In the second case, where $t_{diff} \ll t_{ads}$, observed for example at high concentrations where diffusion is rapid, the surfactant concentration c is uniform, but the surface concentration Γ is no longer in equilibrium with the sub-phase due to the presence of adsorption/desorption barriers. Energy barriers to adsorption are generally caused by electrostatic or steric forces. Leaving the interface also can have an energy cost due to hydrophobic interactions.

In the Langmuir model, considering an ideal interface adjacent to the ideal solution, the rate of adsorption is taken to be proportional to the sub-phase concentration of surfactant and the fraction of the surface lattice unoccupied by the surfactant. The rate of surfactant desorption is taken to be proportional to the fraction of the area occupied by the surfactant. Then the change of surface concentration can be written as

$$\frac{d\Gamma}{dt} = k_a c_s (\Gamma_\infty - \Gamma(t)) - k_d \Gamma(t), \quad (1.50)$$

where the adsorption and desorption rate constants k_a and k_d can be related with adsorption E_a and desorption E_d energies by Arrhenius-type dependence $k_{a,d} = k_{a,d}^0 \exp(-E_{a,d}/RT)$. When diffusion is sufficiently fast, c_s is constant and equal to the bulk concentration. In equilibrium $d\Gamma/dt = 0$ and Equation 1.50 can be rearranged into the Langmuir isotherm 1.43.

By solving Equation 1.50 the explicit dependence of $\Gamma(t)$ can be recovered

$$\Gamma(t) = \Gamma_{eq} + (\Gamma_0 - \Gamma_{eq})e^{-t/t_{ads}} \quad (1.51)$$

with the characteristic adsorption time $t_{ads} = 1/(k_a c + k_d)$. Γ_0 and Γ_{eq} correspond to initial and equilibrium values of surface concentration, respectively.

The interactions between molecules in the surface layer can be taken into account assuming that adsorption and desorption energies depend on the surface concentration. The popular Frumkin model corresponds to a linear variations of E_a and E_d with Γ

$$E_{a,d} = E_{a,d}^0 + RT\nu_{a,d}\frac{\Gamma}{\Gamma_\infty}, \quad (1.52)$$

where $\nu_{a,d}$ are dimensionless proportionality constants. Equation 1.52 can be substituted in the expression of the adsorption rate 1.50. The obtained differential equation can be solved numerically to get the $\Gamma(t)$ dependence. It can be shown that at equilibrium the Frumkin adsorption isotherm is retrieved with

$$A_F = \nu_a - \nu_d. \quad (1.53)$$

1.9 Surface rheology

So far we considered only surfaces in mechanical equilibrium. The deformation of the interface covered by surfactant molecules is well-known to induce a viscoelastic response, like for bulk fluids. This rheological behaviour of interfaces is of great importance for different process in the foam, such as liquid drainage or coalescence, for example [13]. The detailed description of surface continuum mechanics is very complicated, so we will introduce here only some general concepts of interfacial rheology.

Let us consider an element of length dl in an interface. We will consider only small perturbations, because only for this case the simplest linear rules can be applied. By transporting to 2D the 3D formalism, we obtain an expression for the surface force acting on the element dl ¹

$$d\bar{f} = \bar{\bar{\sigma}} \cdot \bar{n} dl, \quad (1.54)$$

where \bar{n} is a unit vector in the tangent plane of the interface, normal to the element dl . The total Cauchy surface stress tensor $\bar{\bar{\sigma}}$ includes isotropic contribution related to the equilibrium surface tension and an additional tensor $\Delta\bar{\bar{\sigma}}$ containing viscous and elastic terms (see [14] for more details)

$$\bar{\bar{\sigma}} = \gamma \bar{\bar{\delta}} + \Delta\bar{\bar{\sigma}}(\bar{\bar{\epsilon}}, \dot{\bar{\bar{\epsilon}}}). \quad (1.55)$$

Here $\bar{\bar{\delta}}$ is a unit tensor, γ is the surface tension at equilibrium which plays a role of 3D pressure. The perturbation part of the stress tensor $\Delta\bar{\bar{\sigma}}$ describes the forces arising in the surface due to the deformation. The elastic and viscous parts of $\Delta\bar{\bar{\sigma}}$ are connected to, respectively, the linear strain tensor $\bar{\bar{\epsilon}}$ and strain rate tensor $\dot{\bar{\bar{\epsilon}}}$ by constitutive laws.

Any perturbation of the interface can be divided into dilational and shear parts (see Figure 1.5). Then the perturbation constituent of the stress tensor $\Delta\bar{\bar{\sigma}}$, strain tensor $\bar{\bar{\epsilon}}$ and strain rate tensor $\dot{\bar{\bar{\epsilon}}}$ can be split into isotropic term corresponding to the change of area and non-isotropic term characterising the shear deformation

$$\Delta\bar{\bar{\sigma}} = \bar{\bar{\sigma}}^d + \bar{\bar{\sigma}}^s, \quad (1.56)$$

$$\bar{\bar{\epsilon}} = \bar{\bar{\epsilon}}^d + \bar{\bar{\epsilon}}^s, \quad (1.57)$$

$$\dot{\bar{\bar{\epsilon}}} = \dot{\bar{\bar{\epsilon}}}^d + \dot{\bar{\bar{\epsilon}}}^s. \quad (1.58)$$

For a purely elastic surface, the Hooke's law states

$$\bar{\bar{\sigma}}^d = 2E\bar{\bar{\epsilon}}^d, \quad (1.59)$$

$$\bar{\bar{\sigma}}^s = 2G\bar{\bar{\epsilon}}^s, \quad (1.60)$$

¹In this thesis we will use a single bar notation for vectors and a double bar notation for second order tensors.

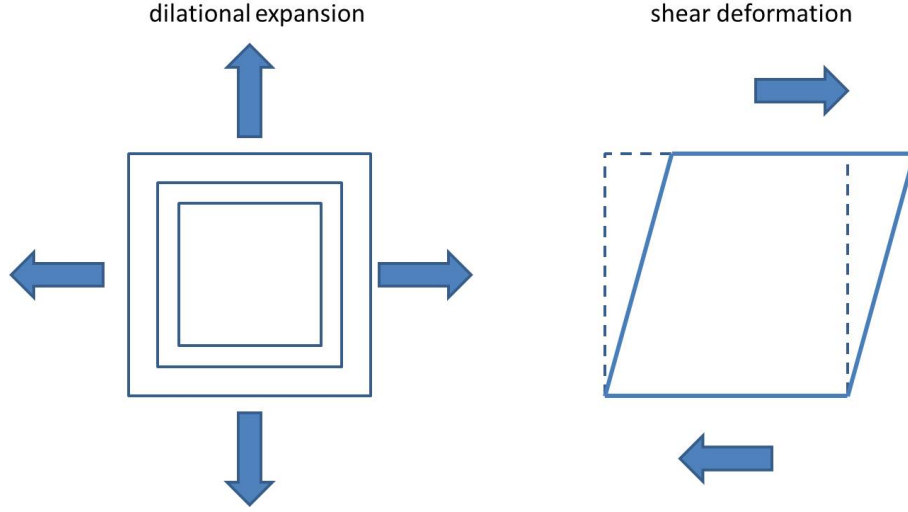


Figure 1.5: A schema of dilational (on the left) and shear (on the right) deformation of the interface

where E and G are dilational and shear surface elastic modulus measured in N/m .

The purely viscous two-dimensional fluid can be considered as a Newtonian liquid

$$\bar{\sigma}^d = 2\mu_d \dot{\bar{\epsilon}}^d, \quad (1.61)$$

$$\bar{\sigma}^s = 2\mu_s \dot{\bar{\epsilon}}^s, \quad (1.62)$$

where μ_d and μ_s are dilational and shear surface viscosities measured in kg/s .

In the presence of surfactant, surfaces can exhibit both viscous and elastic properties simultaneously. The total response can be predicted using different models, such as a Maxwell or a Kelvin-Voigt models [14, 15]. The behaviour is also shown to depend strongly on the characteristic frequency of the external forcing.

Quantitatively, in most systems dilational elasticity is much more important than the shear elasticity. Moreover, the shear elastic modulus is usually zero, while the dilational elastic modulus typically varies between a fraction of a mN/m to hundreds mN/m [15]. The shear viscosity μ_s has is typically around 10^{-8} to 10^{-7} kg/s for surfaces covered with surfactants of low mass [16].

Chapter 2

Structure of foams

2.1 Introduction

Foam is a two phase system consisting of closely packed gas bubbles surrounded by a continuous liquid phase. Many properties of the liquid foams are strongly related to their geometrical structure. The opaqueness of foam, for example, is due to the light scattering from liquid films. The complex rheological behaviour of foams is strongly related with the structural rearrangements. The knowledge of the foam structure is crucially important to predict the propagation of liquid through the foam or describe the electrical conductivity of foams.

The equilibrium foam structure is determined by the minimisation of foam energy under a number of constraints. Typically used constraints are constant volume of each bubble and constant liquid volume. Simple estimations show that for any reasonable bubble size the foam thermal energy is much smaller than the surface energy, so the thermal one plays no role in the organisation of bubble packing. In this chapter we will not consider the foam potential energy due to buoyancy. In practice it means that we consider the optimisation of the foam structure under a fixed liquid fraction constraint. The influence of gravity on the foam is discussed in more details in the next chapter. Then the total energy is simply proportional to the surface area A_{tot}

$$E = \gamma A_{\text{tot}}. \quad (2.1)$$

For isolated bubbles the surface energy has a minimum for a spherical shape, but in foams due to superposed constraints different structures can be obtained.

A key parameter to understand the structure of liquid foams is liquid fraction being the ratio of the liquid volume to the total volume of foam $\varepsilon = V_{\text{liq}}/V_{\text{foam}}$. Different types of structures are obtained depending on the liquid fraction (see Figure 2.1)

- At small liquid fractions $\varepsilon \lesssim 0.05$ foams consist of thin films which may often be idealized as single surfaces. The bubbles take the form of polyhedral cells with these surfaces as their faces: this is a *dry foam*.
- At high liquid fractions $0.05 \lesssim \varepsilon \lesssim \varepsilon_{\text{max}}$ bubbles can be approximated by contacting, deformed spheres: this is a *wet foam*.

- For very high liquid fractions $\varepsilon \gtrsim \varepsilon_{\max}$ we can not describe the system as a foam. Bubbles does not touch each other any more and they are generally described as a *bubbly liquid*. Such systems are not stable in the gravity field and rapidly transforms in *wet foams*.

The transition from bubbly liquid to wet foam occurs at a precise value of critical liquid fraction ε_{\max} , which is about 0.3 in 3D. This value corresponds to a foam jamming transition: above ε_{\max} bubbles are not in contact with each other and many foam parameters, such as elastic moduli or yield stress vanish.

Another key parameter is the *polydispersity* p of bubbles. Polydispersity p is commonly defined as the normalised standard deviation of the distribution of the "equivalent bubble radii" R , i.e. the radii the bubbles would have if they were spherical ($R = \sqrt[3]{\frac{3V}{4\pi}}$)

$$p = \left(\frac{\langle R^2 \rangle}{\langle R \rangle^2} - 1 \right)^{1/2}. \quad (2.2)$$

Foams with polydispersity less than 0.05 are generally called *monodisperse*. The higher polydispersity level corresponds to the *polydisperse* foam.

Polydispersity of foams is closely related with the *ordering* of the foam structure. Generally two limiting cases can be considered. It is shown that depending on the generation technique bubbles are either arranged in a highly *ordered* crystalline or in a *disordered* random structure. Even a small increase of polydispersity usually disorders the foam, so that real foams often have polydisperse disordered bubbles. However for many applications it is useful to simplify the structure to an idealized monodisperse foam.

Figure 2.1 gives a summary of the most commonly encountered types of foams.

To compare different foam structures the normalized energy density is used

$$\hat{E}(\varepsilon) = \frac{\langle S \rangle}{\langle V \rangle^{2/3}}, \quad (2.3)$$

where $\langle S \rangle$ and $\langle V \rangle$ are the mean surface area and volume of bubbles, respectively. The minimum possible energy density corresponds to a foam consisting of spherical bubbles and is about 4.836. Various other non-dimensional quantities are used in the literature to estimate the energy of the structure.

Since thermal energy is negligible, the macroscopic bubbles are generally trapped in local minima of a very complex energy landscape of the foam. Topological changes, which may lead to a reduction of the global energy via neighbour switching of bubbles, are energetically so costly, that they do not happen spontaneously. There is thus a strong dependence between the method of foam generation and the resulting bubble packing.

Foam structure may nevertheless be successfully predicted for the simplest cases of monodisperse periodic foams. However, even though the global packing may not be optimal, the microscopic foam structure, at least in the limit of dry foams, can be satisfactory described.

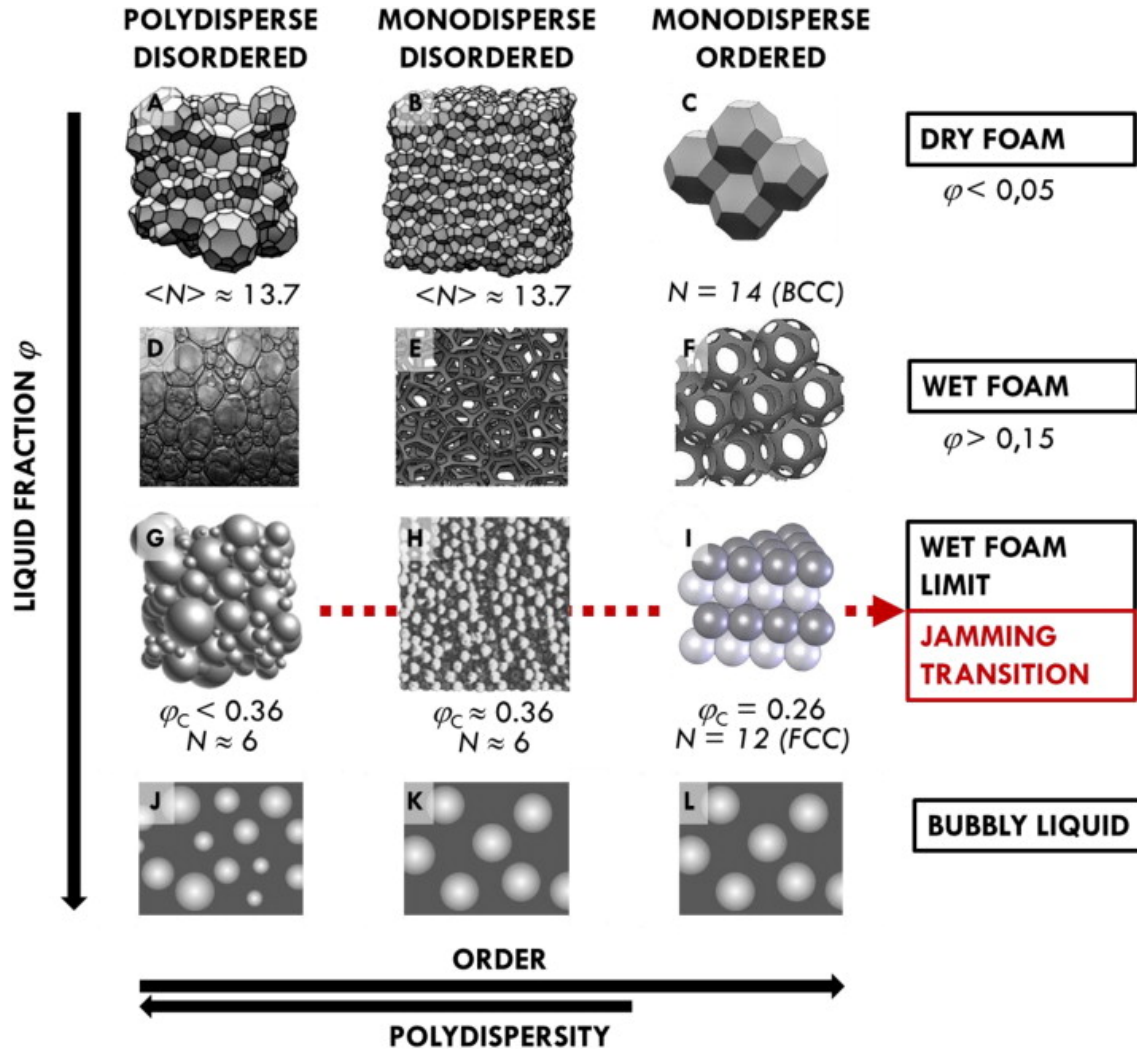


Figure 2.1: Representations of different foam structures. The key parameters are liquid fraction, polydispersity and order/disorder. An average number of neighbours N is shown for each structure. The picture was obtained from [17].

2.2 Dry foams

Very dry foams ($\varepsilon \rightarrow 0$) are satisfactorily described by an ideal foam model. We define an ideal foam by making following simplifications

- Foam is infinitely dry ($\varepsilon = 0$).
- The foam is at mechanical equilibrium.
- Foam energy is proportional to the surface area of the bubbles.
- The thin films separating the bubbles are "ideal": they have zero thickness and film tension 2γ (the factor 2 comes from the fact that each film has two interfaces).
- The foam is incompressible, the volume V of each bubble is fixed.

The structure of ideal dry foams is described by Plateau's laws which were formulated by Joseph Plateau in 1873 and fully proved in 1976 by Jean Taylor:

- Each film separating two bubbles has a constant mean curvature $H = 0.5(1/R_1 + 1/R_2)$ fixed by Young-Laplace law (see Equation 1.5).
- Three films meet symmetrically under angles of 120° in channels called Plateau borders.
- Four such Plateau borders meet symmetrically in junctions called nodes or vertices under the tetrahedral angle of 109.47° .

Plateau's laws explain how Plateau borders and films are connected and set important constraints on the possible ideal foam structures. But they do not predict the global minima of ideal foam. In 1887, Kelvin asked how space could be periodically partitioned into cells of equal volume with the least area of surface between them, i.e., what was the most efficient monodisperse foam structure. This problem has since been referred to as the Kelvin problem. After considering various possibilities he proposed a structure consisting of the truncated octahedrons called *tetrakaidecahedrons*. Bubbles in Kelvin structure have 14 neighbours and are arranged in a body centred cubic structure, as shown in Figure 2.2. Kelvin structure has the energy density $\hat{E} \approx 5.3063$. In order to satisfy Plateau's rules Kelvin introduced a slight curvature in the 8 hexagons making up the Kelvin cell, while its 6 square faces are flat. In Kelvin structure every edge has the same length L .

The Kelvin structure remained unbeaten for almost one century and only in 1994 a structure having 0.3 % less interfacial area ($\hat{E} \approx 5.288$) was computed using Surface Evolver software by Denis Weaire and his student Robert Phelan [18]. The Weaire-Phelan structure has eight bubbles, of two different types, in a periodic unit (see Figure 2.2). These periodic units fill space when placed at the lattice points of a simple cubic lattice. All bubbles have equal volume, so this is really a solution of the Kelvin Problem - although there is no mathematical proof that it is the optimal one.

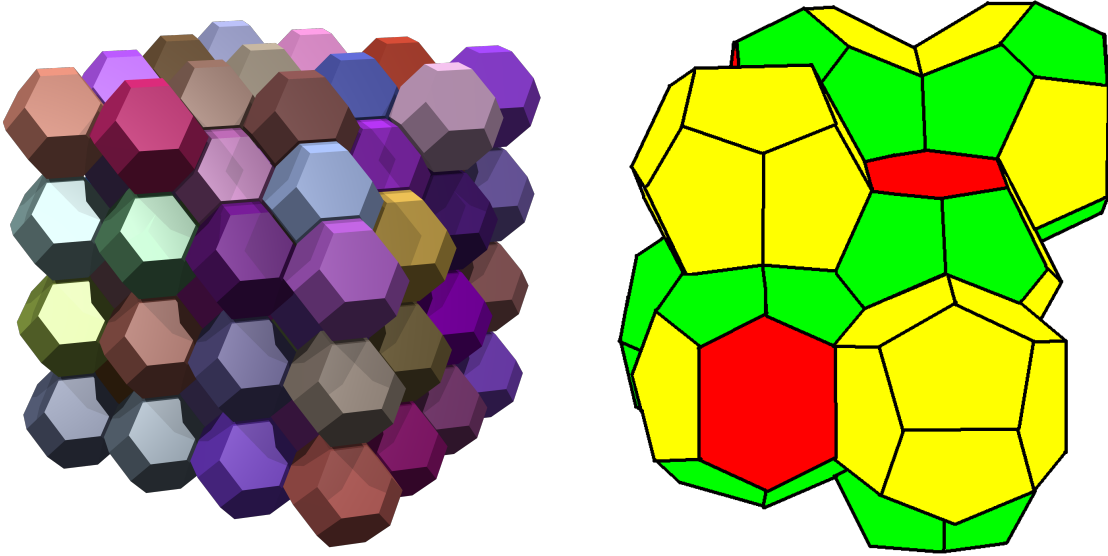


Figure 2.2: On the left: Kelvin structure. On the right: Weaire-Phelan structure

So far we explored a mathematical model of infinitely dry foam. Real foams always have a finite liquid fraction. We can extend our ideal infinitely dry foam model for fractions up to a few percent. In such foams, the films between neighbouring bubbles remain very thin, while Plateau borders and nodes swell to accommodate the liquid. The structure of such foams is generally considered equivalent to that of an infinitely dry foam with "decorated" Plateau borders. Such "decorated" Plateau borders form finite size channels replacing lines of infinitely dry foams. For sufficiently dry foams ($\varepsilon \lesssim 0.01$) the channel can be idealized as the volume between three cylinders having radius of curvature R_{Pb} , called a radius of Plateau border curvature (see Figure 2.3). Then the cross-section of the Plateau border is a concave triangle with the area

$$A_{Pb} = \left(\sqrt{3} - \frac{\pi}{2}\right) R_{Pb}^2. \quad (2.4)$$

Also the length of the channels is that of the node-to-node separation L , because the nodes are tiny.

For higher liquid fractions the liquid in the nodes should be taken into account.

Although the Weaire-Phelan structure is energetically favourable over the Kelvin structure, it has a much more complicated geometry. Due to its structural simplicity, the Kelvin structure is usually used for analytical estimations of different foam properties. In most of the practical applications the Kelvin structure gives a reasonable approximation of the real foam geometry.

For a slightly wet Kelvin structure ($\varepsilon \lesssim 0.1$) the relationship between the edge length L , radius of Plateau border curvature R_{Pb} and liquid fraction ε has been computed using the Surface Evolver software [19]

$$\varepsilon = 0.171 \left(\frac{R_{Pb}}{L}\right)^2 + 0.2 \left(\frac{R_{Pb}}{L}\right)^3. \quad (2.5)$$

Neethling et al. show that taking into account the foam expansion at high liquid fractions the equivalent bubble radius R can be related with node to node distance

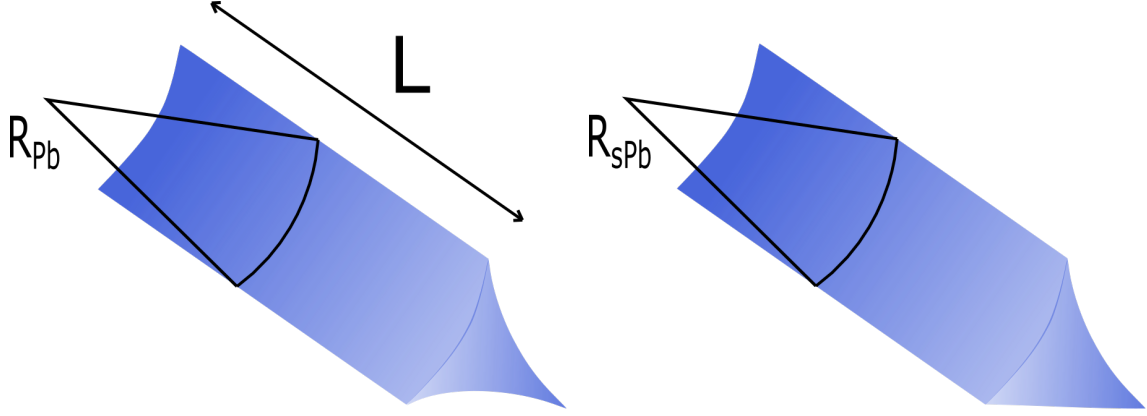


Figure 2.3: On the left: Structure of the dry Plateau border. On the right: Structure of the dry surface Plateau border

L for Kelvin structure by the following relationship [20]

$$\frac{4}{3}\pi R^3 = (1 - \varepsilon)2^{7/2}L^3. \quad (2.6)$$

By substituting Equation 2.6 in Equation 2.5 we get an expression for the liquid fraction

$$\varepsilon = 0.332 \left(\frac{R_{Pb}}{R}(1 - \varepsilon)^{1/3} \right)^2 + 0.540 \left(\frac{R_{Pb}}{R}(1 - \varepsilon)^{1/3} \right)^3. \quad (2.7)$$

First and second term account for the liquid in the Plateau borders and nodes, respectively. Equation 2.7 can easily be solved numerically to get a dependence of ε on R_{Pb}/R . For a sufficiently dry foam ($R_{Pb} \ll R, \varepsilon \lesssim 0.01$) it can be simplified to

$$\varepsilon \approx 0.332 \left(\frac{R_{Pb}}{R} \right)^2. \quad (2.8)$$

2.3 Wet foams

In the wet limit all bubbles are spherical and pack together under the influence of gravity. The optimal wet foam structure therefore corresponds to the densest packing of solid spheres, i.e. the involved interfacial energy is assumed to be constant.

For equal size spheres two densest regular lattices are well-known: face centred cubic (**FCC**) and hexagonally close packed (**HCP**) in which each sphere is in contact with 12 nearest neighbours. Both structures have a packing density $\pi/(3\sqrt{2}) \approx 0.74$ corresponding to a liquid fraction of $\varepsilon_{max} = 0.26$. It was proven by Carl Friedrich Gauss that it is the highest possible packing density for a regular packing of equal spheres. In 2005 T.C. Hales extended the proof to any arrangement of spheres, either regular or irregular [21].

Although all crystalline closed-packed structures have the same packing density, a number of different experiments surprisingly showed a clear preference of (FCC) arrangements. Such a preference of FCC has been recently explained by more optimal distribution of mechanical stresses.

For disordered monodisperse foams the critical liquid fraction ε_{max} is always a bit lower. If the bubbles are randomly close packed (**RCP**) the empirical results state that ε_{max} is about 0.36. In polydisperse foams the critical liquid fraction decreases only slightly from the value of 0.36 for the modest polydispersities which are typically obtained using many experimental foaming techniques.

2.4 Quasi-2D foams

When a monolayer of bubbles is squeezed between two solid plates in such a manner that each bubble touches both plates a quasi two-dimensional foam is formed (also referred to as a 2D glass-glass (2D GG) foam in a Hele-Shaw cell [22, 23], see Figure 2.4). Properties of such systems attract significant interest as their local two-dimensional structure can be directly observed which is awkward for classical 3D foams, yet many physical phenomena linked to foam ageing or rheology can be analogously studied [24–32]. This makes quasi-2D foams an excellent model system.

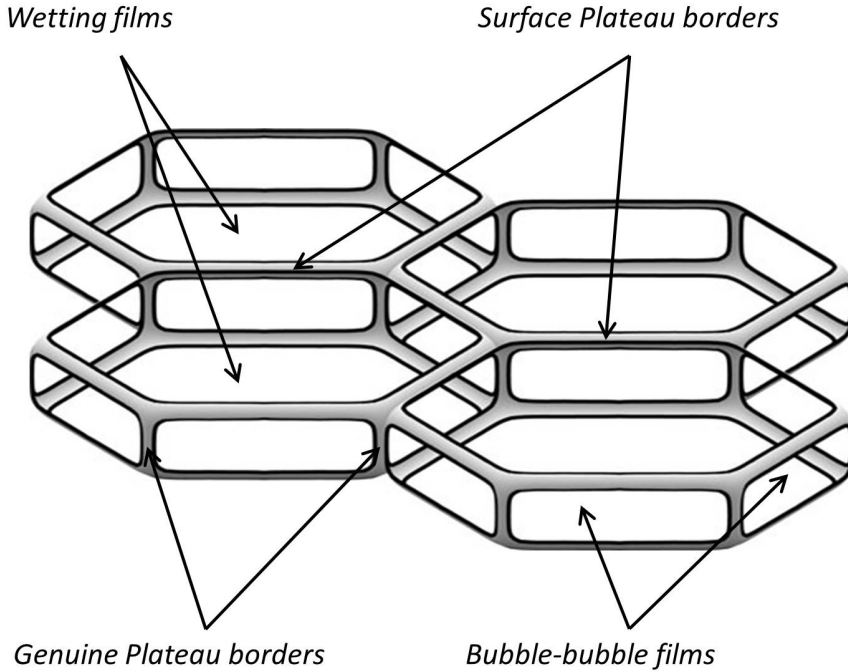


Figure 2.4: A structure of quasi-2D foam squeezed between two glass plates. The picture was obtained from [23].

For theoretical and computational purposes, the third dimension of these quasi-2D foams is often neglected. In such true 2D-foams interfacial tension turns into line tension, the liquid fraction is given by the ratio of the liquid to the total area of the foam, and it is the total line length of the foam which needs to be minimised in the search for the optimal structure of the foam. For many proposes, this is an extremely useful simplification. In the case ordered monodisperse foam the optimal structure consists of bubbles arranged on a triangular lattice, giving the well-known honeycomb structure for the dry case.

Quasi-2D foams could be even more widely used but often a measure of the liquid content and a proper description of the detailed three-dimensional geometry is required. Despite the ease of observation of the bubble size, a description of the full structure is quite complicated. In addition to the bubble size and liquid content typically used to characterize 3D foams, a degree of squeezing (a ratio of the thickness of the bubble monolayer to the bubble diameter) plays an important role for quasi-2D foams giving an enormous variety of different bubble shapes. An experimental determination of the exact geometry is hindered: the main source of structural information still remains the computer simulation [22].

A geometry of dry ordered monodisperse foams in equilibrium was recently described by C. Gay et al [23]. In the case of a monodisperse ordered foam each bubble has exactly six neighbours (as shown in Figure 2.4). Each bubble is therefore surrounded by 6 genuine Plateau borders (liquid channels that run across the gap between both solid plates at the junction between three bubbles), 12 surface Plateau borders (liquid channels that run along the solid plates at the junction between two bubbles), 6 films separating bubbles and 2 wetting films covering the surface of the plates. A junction of three surface Plateau borders and one genuine Plateau border forms a node.

The cross-section of a single surface Plateau border is a triangle with two concave sides characterised by a surface Plateau border radius of curvature R_{sPb} (see Figure 2.3). Assuming 0° contact angle a cross-sectional area of one surface Plateau border can be calculated from simple geometrical arguments

$$A_{sPb} = (2 - \frac{\pi}{2})R_{sPb}^2, \quad (2.9)$$

where R_{sPb} is the radius of curvature of the wall Plateau border.

Viewing from above only the wall Plateau borders are visible: they form two identical hexagonal honey-comb networks. The observed 2D structure provides us with significant information about the foam state. Analysing the images a thickness of surface Plateau borders d and a size of bubbles can be extracted. The latter can be expressed as a distance D between two centres of adjacent hexagons (see Figure 5.5). Simple relations exist between the hexagon perimeter P , area A and D

$$P = 6D/\sqrt{3}, \quad (2.10)$$

$$A = \sqrt{3}D^2/2. \quad (2.11)$$

In the described geometry the real 3D structure of the quasi-2D foam can be considered as consisting of hexagonal prisms. Volume of one prism is $V = AH$, where H is a separation between the plates. Then the total liquid volume fraction can be simply determined as

$$\varepsilon = \frac{V_{\text{liq}}}{V}, \quad (2.12)$$

where V_{liq} correspond to the liquid volume per bubble. Combining Equations 2.9 and 2.4 and assuming that the amount of liquid in the films is negligible V_{liq} can be written as

$$V_{\text{liq}} \approx (2 - \pi/2)PR_{sPb}^2 + (2\sqrt{3} - \pi)R_{Pb}^2H. \quad (2.13)$$

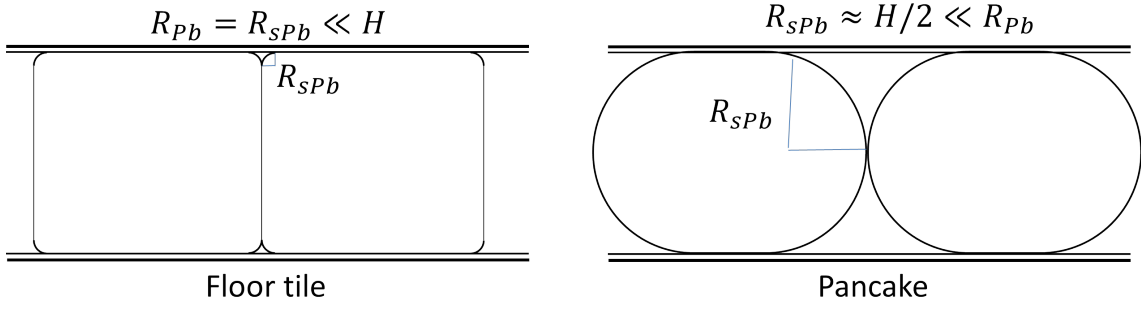


Figure 2.5: On the left: a schema of quasi-2D foam in a "floor tile" regime. On the right: a schema of quasi-2D foam in a "pancake" regime.

The first term corresponds to the volume of the pseudo Plateau borders V_{sPb} and the second one - to the genuine Plateau borders V_{Pb} . Depending on the ratio between these terms two asymptotic regimes can occur:

- if $H \ll R_{Pb}$, each bubble takes the form of a thick "pancake" (see Figure 2.5). Then the surface Plateau border radius is almost equal to $H/2$ which gives

$$V_{liq} \approx (1/2 - \pi/8)PH^2 + (2\sqrt{3} - \pi)R_{Pb}^2H. \quad (2.14)$$

A more precise expression may be obtained assuming an elliptical cross-section of the surface Plateau border as described [23]. Solving the Laplace equation the following expression for the liquid fraction can be derived

$$\varepsilon \approx (1/2 - \pi/8)\frac{PH}{A} \left[1 - \frac{2H}{3R_{Pb}} \right] + (2\sqrt{3} - \pi)\frac{R_{Pb}^2}{A}. \quad (2.15)$$

The Plateau border radius can be linked with experimentally measurable surface Plateau border thickness by the following expression

$$d = \frac{H}{2} \left[1 - \frac{H}{6R_{Pb}} \right]. \quad (2.16)$$

- In the reverse limit $R_{Pb} \ll H$. In this case the bubbles are shaped like "floor tile" (see Figure 2.5). In this geometry for sufficiently dry foam the surface and genuine Plateau border radii coincide $R_{PB} = R_{sPb}$. Then the liquid fraction is

$$\varepsilon \approx (2 - \pi/2)\frac{R_{sPb}^2P}{AH} + (2\sqrt{3} - \pi)\frac{R_{sPb}^2}{A}. \quad (2.17)$$

In this geometry $R_{sPb} = d/2$, the liquid fraction can be easily calculated from the experimental data. This regime is especially convenient for the experimental investigation: it is characterized by a more simple geometry than a "pancake" regime, liquid fraction strongly depends on the surface Plateau border radius.

The described geometry is valid only for sufficient dry quasi-2D foams. We will see in the chapter 8 how the wet quasi-2D foam can be described at least in the "floor tile" regime.

Chapter 3

Hydrodynamics of particles and foams

3.1 Introduction

Small particles suspended in a foam can move through the network of Plateau borders. Depending on the particle size their motion is either controlled by thermal fluctuations or by the buoyancy force arising from the difference between the liquid ρ and the particle ρ_p densities. Quantitatively the distinction between these two regimes can be drawn using a *Peclet number* comparing the thermal energy and potential energy of buoyancy

$$Pe = \frac{(\rho_p - \rho)gV_pL_p}{kT}, \quad (3.1)$$

where V_p is the volume of the particle and L_p is its characteristic size. For a quantitative estimation we can state that for most of the used materials the transition ($Pe \approx 1$) corresponds to a particle size $L_p \sim 0.1 - 2 \mu m$. For small $Pe \ll 1$ particles move randomly due to collisions with liquid molecules. Such particles are generally referred to as *Brownian*. The big $Pe \gg 1$ corresponds to *non-Brownian* particles whose motion can be described by continuous fluid mechanics. If the particles are more dense than the liquid they fall down in the gravity field, a process called *sedimentation*. For particles lighter than the liquid, their rise is referred to as *creaming*.

In this chapter we will consider some aspects of non-Brownian particle hydrodynamics. We will limit our discussion only to spherical particles as their theoretical description is the simplest one and they are the most widely used in practical applications. We will first have a look on the sedimentation of an isolated particle, then we will see how collective effects play a role in more concentrated suspensions. We will finish the chapter by considering a gravity induced liquid flow through foams, a process called *drainage*. We will see that the air bubbles can be considered as soft deformable particles and the foam can be successfully modelled as a porous material.

3.2 Governing equations of fluid mechanics

A continuous flow of liquid is usually described by the Eulerian approach which considers a velocity field $\bar{v}(\bar{r}, t)$ defined relative to some laboratory coordinates \bar{r} . In this case the deformation of fluid can be described by the gradient of velocity tensor $\nabla \bar{v}$ ¹. As any tensor $\nabla \bar{v}$ can be decomposed into the sum of symmetric and antisymmetric terms

$$\nabla \bar{v} = \frac{1}{2}(\nabla \bar{v} + \nabla \bar{v}^T) + \frac{1}{2}(\nabla \bar{v} - \nabla \bar{v}^T). \quad (3.2)$$

In the previous equation we can identify a symmetric *rate-of-strain tensor*

$$\bar{\bar{E}} = \frac{1}{2}(\nabla \bar{v} + \nabla \bar{v}^T) \quad (3.3)$$

and an antisymmetric *tensor of rotation*

$$\bar{\bar{\Omega}} = \frac{1}{2}(\nabla \bar{v} - \nabla \bar{v}^T). \quad (3.4)$$

It can be shown that $\bar{\bar{E}}$ represents the rate of deformation of the fluid while $\bar{\bar{\Omega}}$ corresponds to the rotation of the fluid as a solid body.

In the absence of sources and sinks the conservation of mass gives us *the equation of continuity*

$$\frac{\partial \rho}{\partial t} + \nabla \cdot (\rho \bar{v}) = 0, \quad (3.5)$$

where ρ is the fluid density.

For a single component fluid, the density is a function of temperature and pressure given by the equation of state. In this chapter we will consider only isothermal conditions, so we focus our attention only on the dependence on pressure. It turns out that for most liquids (water being the most important example) density is almost insensitive to reasonably small variations of pressure. Assuming that ρ is constant, Equation 3.5 simplifies to

$$\nabla \cdot \bar{v} = 0. \quad (3.6)$$

The last condition is equivalent to $Tr(\bar{\bar{E}}) = 0$. In the following we will restrict our consideration only to such *incompressible* fluids having uniform density because for the majority of soft matter hydrodynamic problems and for all of those considered in this thesis this approximation works very well.

To describe the motion of the continuous fluid we also need to write an analogue of Newton's second law. The motion of a volume of liquid $V(t)$ having a surface $S(t)$ is produced by the action of externally applied forces which are assumed to be of two kinds (see Figure 3.1): i) surface forces $\oint_{S(t)} \bar{T} dS$, where \bar{T} is a surface stress acting on a small element of a surface dS with a unit normal \bar{n} , ii) body forces $\iiint_{V(t)} \rho \bar{f} dV$ such as gravity or electrostatic forces.

¹In this thesis we will use the following definition of the gradient of a vector $\nabla \bar{v} = \frac{\partial v_i \bar{e}_i}{\partial x_j} \otimes \bar{e}_j$. Let us note that in some books a transposed expression is used.

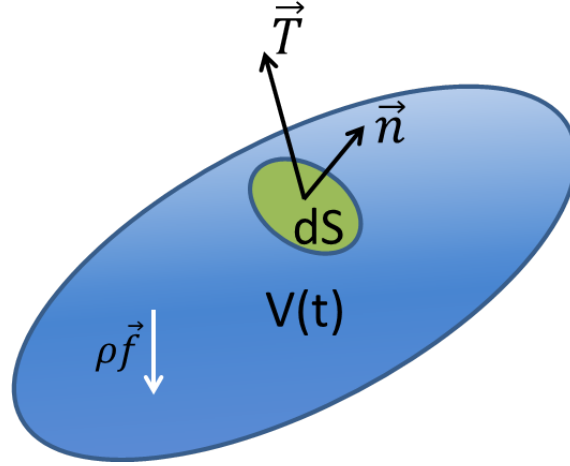


Figure 3.1: Surface stress \vec{T} acting on a infinitely small element of the surface dS having a unit normal \vec{n} and a body force $\rho \vec{f}$ acting in a volume $V(t)$.

The Cauchy postulate states that surface stress depends only on the normal to the interface and it is not influenced by the curvature of the surface. Then \vec{T} can be shown to linearly depend on \vec{n}

$$\vec{T} = \vec{\Sigma} \cdot \vec{n}, \quad (3.7)$$

where $\vec{\Sigma}$ is a second order *Cauchy stress tensor*. For an isotropic liquid, $\vec{\Sigma}$ is symmetric ($\vec{\Sigma} = \vec{\Sigma}^T$) and has only 6 different elements.

The concept of stress tensor allows us to write the conservation of momentum in the following form

$$\rho \left(\frac{\partial \vec{v}}{\partial t} + \nabla \vec{v} \cdot \vec{v} \right) = \nabla \cdot \vec{\Sigma} + \rho \vec{f}. \quad (3.8)$$

The left hand side corresponds to the liquid acceleration whereas the right one represents the sum of acting forces. The relationship between the stress tensor $\vec{\Sigma}$ and rate-of-strain tensor \vec{E} is given by the corresponding constitutive law. We do not need to consider a rotation tensor $\vec{\Omega}$ as the rotation of the solid body does not induce any friction between the liquid elements and thus any acceleration of the fluid. The simplest model for an incompressible fluid assumes a linear relationship between $\vec{\Sigma}$ and \vec{E} and can be written as

$$\vec{\Sigma} = -p\vec{\delta} + 2\mu\vec{E}, \quad (3.9)$$

where p is the mechanical pressure defined as $p = -\frac{1}{3}Tr(\vec{\Sigma})$ and μ is a proportionality constant called viscosity (measured in Pa.s). A liquid which obeys Equation 3.9 is referred to as an incompressible *Newtonian liquid*. It can be rigorously shown by considering the entropy of a Newtonian liquid that only positive values of viscosity $\mu \geq 0$ are allowed thermodynamically. Substituting Equation 3.9 into Equation 3.8 one can get, after some reorganization,

$$\rho \left(\frac{\partial \vec{v}}{\partial t} + \nabla \vec{v} \cdot \vec{v} \right) = -\nabla p + \mu \Delta \vec{v} + \rho \vec{f}. \quad (3.10)$$

Equations 3.6 and 3.10 can fully describe a flow of the incompressible Newtonian liquid and are together referred to as the *Navier-Stokes equations*.

We note that the Navier-Stokes equations are non-linear, and their general analytical solution is one of the open problems in mathematics. The problem is simplified a lot by neglecting the inertia effect $\nabla \bar{v} \cdot \bar{v}$. The relative importance of inertial and viscous effects is quantified by the *Reynolds number*

$$Re = \frac{\rho UL}{\mu} \sim \frac{\rho |\nabla \bar{v} \cdot \bar{v}|}{\mu |\Delta \bar{v}|}, \quad (3.11)$$

where U and L are the characteristic velocity and length scales, respectively. When $Re \ll 1$, we can neglect inertial effects, while when $Re \gg 1$, inertial effects dominate. It turns out that, for most of the problems in soft matter physics, Re is usually quite small due to small sizes and velocities of objects under investigation. In the absence of other time-scales than L/V , the small values of Reynolds number $Re \ll 1$ allow neglecting the acceleration term $\partial \bar{v} / \partial t$ as well. It means that we consider only the steady state where the velocity field does not evolve with time. Then one gets *Stokes equations*

$$\begin{aligned} -\nabla p + \mu \Delta \bar{v} + \rho \bar{f} &= 0, \\ \nabla \cdot \bar{v} &= 0, \end{aligned} \quad (3.12)$$

also called the creeping flow equations. In the case of gravitational effects, $\bar{f} = \bar{g}$, where \bar{g} is the gravitational acceleration. The gravity force can be included in a modified pressure field also called the dynamic pressure $p_d = p - \rho \bar{g} \cdot \bar{r}$. We can also introduce a dynamic stress tensor $\bar{\bar{\Sigma}}_d = -p_d \bar{\bar{\delta}} + 2\mu \bar{\bar{E}}$. Then we obtain the *homogeneous Stokes equations*

$$\begin{aligned} -\nabla p_d + \mu \Delta \bar{v} &= 0, \\ \nabla \cdot \bar{v} &= 0. \end{aligned} \quad (3.13)$$

An important property of homogeneous Stokes equations is their linearity. It means that a sum of different solutions also gives a solution of Stokes equation. For example, in the case of a settling sphere, we can conclude that the total motion can be obtained by summing up a pure translational flow without rotation and a rotation flow without settling.

The Stokes equations describe a stationary flow and thus do not require any initial conditions. However, the presence of the particles in the system influences the boundary condition at the particle interfaces. Depending on the type of interface different boundary conditions can be used:

- For a fluid-solid interface at rest it is generally assumed that the interface is impermeable and the fluid is immobile close to interface (no slip condition). This gives $\bar{v} = 0$ at the interface.
- The boundary condition for the fluid-fluid interface is usually written in terms of stresses. For a clean stress-free interface it can be written as $\bar{n} \cdot (\bar{\bar{\Sigma}}^{(1)} \cdot \bar{n} - \bar{\bar{\Sigma}}^{(2)} \cdot \bar{n}) = 2\gamma H$ (Laplace law) and $\bar{s} \cdot (\bar{\bar{\Sigma}}^{(1)} \cdot \bar{n} - \bar{\bar{\Sigma}}^{(2)} \cdot \bar{n}) = 0$, where \bar{n} and \bar{s}

denote, respectively, the unit normal and tangent vectors to the interface. For interfaces containing adsorbed substances the effect of surface rheology and possible Marangoni flow should also be taken into account. Using a concept of the surface stress tensor $\bar{\bar{\sigma}}$ introduced in Chapter 1 the boundary condition at the fluid-fluid interface in the most general case can be written as $\bar{\bar{\Sigma}}^{(1)} \cdot \bar{n} - \bar{\bar{\Sigma}}^{(2)} \cdot \bar{n} = \nabla_s \cdot \bar{\bar{\sigma}}$, where ∇_s is the surface gradient operator.

3.3 Sedimentation of a single particle

We will start our study of particle sedimentation by considering a single spherical particle with radius R falling in the liquid with constant velocity U_p . We will consider a particle in uniform translation without rotation. The movement of the particle disturbs the liquid and creates a velocity field. By change of the reference frame this problem can be made equivalent to the flow of liquid around an immobile particle. This situation is sketched in Figure 3.2. The boundary conditions correspond to a no slip condition at the particle interface and a uniform flow $\bar{U}^\infty = -\bar{U}_p$ infinitely far away from the particle

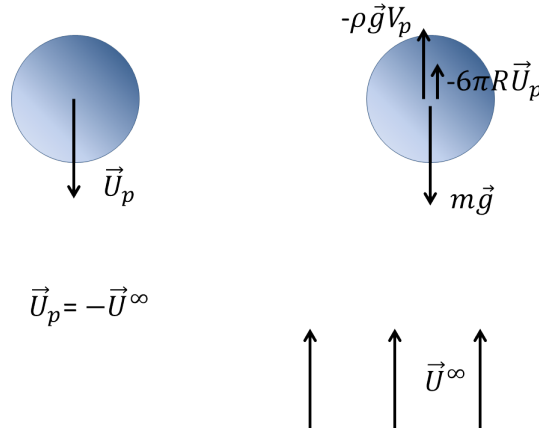


Figure 3.2: On the left: Sphere translating in the liquid. On the right: Fixed sphere in the uniform stream; a balance of gravity, buoyancy and drag forces is shown.

$$\bar{v} = \bar{U}^\infty \quad \text{at} \quad |\bar{r}| = \infty, \quad (3.14)$$

$$\bar{v} = 0 \quad \text{at} \quad |\bar{r}| = R, \quad (3.15)$$

where r is a radial coordinate starting from the centre of the particle.

The particle size R and velocity U_p give us natural length and velocity scales. Estimations show that for micro- and millimetric particles falling in water Re is usually small allowing us to use Stokes approximation. The homogeneous Stokes equations 3.13 can be solved using the above boundary conditions to get the velocity and dynamic pressure fields and then to calculate the dynamic stress tensor $\bar{\bar{\Sigma}}_d$ at

each point. It turns out that the disturbance fields decay very slowly away from the sphere, as r^{-2} for the pressure and r^{-1} for the velocity. The drag force acting on the particle can be calculated as

$$\bar{F}_{drag} = \oint_{S_p} \bar{\bar{\Sigma}}_d \cdot \bar{n} dS. \quad (3.16)$$

Here we use $\bar{\bar{\Sigma}}_d$ instead of $\bar{\bar{\Sigma}}$ to evaluate only the part of the force due to viscous stress, the total force acting on the particle also includes the buoyancy force. These calculations were for the first time performed by George Gabriel Stokes in 1851. For the sake of simplicity we will only cite here the final result. The following expression has been derived for the frictional force exerted on spherical objects in a viscous fluid

$$\bar{F}_{drag} = 6\pi\mu R \bar{U}_p. \quad (3.17)$$

In the stationary regime the drag force is compensated by a buoyancy force and a gravitational force

$$6\pi\mu R U_p = (\rho_p - \rho)g \frac{4}{3}\pi R^3, \quad (3.18)$$

which gives the well-known expression for the sedimentation velocity of an isolated spherical particle

$$U_p = \frac{2(\rho_p - \rho)gR^2}{9\mu}. \quad (3.19)$$

3.4 Sedimentation of suspensions

We now turn our attention to the sedimentation of many particles dispersed uniformly in a quiescent viscous liquid. In very dilute suspensions (for particle volume fractions smaller than 10^{-4}) the inter-particle distance is very large and they do not interact at all. Then the motion of each particle is described by the Stokes law. The separation must be very large as we know that the liquid velocity field induced by each particle decays very slowly, as r^{-1} . For more concentrated suspensions, if the separation is not so large, the flow induced by one particle affects the motion of the others and vice versa, creating effective hydrodynamic interactions between the particles. In a fixed volume, the liquid moves upwards on average to compensate for the settling of the particles. This fluid back-flow hinders the fall of the particles and leads to an average sedimentation velocity which is less than the settling velocity of the isolated particles. The hindrance effect becomes more pronounced with the increase of the particle volume fraction φ . It is common to write the average sedimentation velocity of the suspension as

$$\langle U_s \rangle = U_p f(\varphi). \quad (3.20)$$

The settling function $f(\varphi)$ is a monotonically decreasing function, which is assumed to depend only on the solid volume fraction φ and have $f(0) = 1$. For dilute random mixtures of hard spheres a theoretical expression for the settling function was proposed by Batchelor in 1972 [33]

$$f(\varphi) = 1 - 6.55\varphi + O(\varphi^2). \quad (3.21)$$

This prediction agrees reasonably with the experimental data for very low φ but significantly deviates for solid fractions higher than 0.05.

There exist also different empirical expressions for $f(\varphi)$. The most widely used one was suggested by Richardson and Zaki in 1954 [34]

$$f(\varphi) = (1 - \varphi)^n. \quad (3.22)$$

The exponent n varies with the particle Reynolds number, for low Re it is usually between 4.65 and 6.55 [34–36]. The *Richardson-Zaki law* has been shown to describe experimental data very well in a wide range of volume fractions [37]. Note that close to the maximum packing fraction $\varphi_{\max} \sim 0.60$ the settling velocity starts to deviate from this correlation [38].

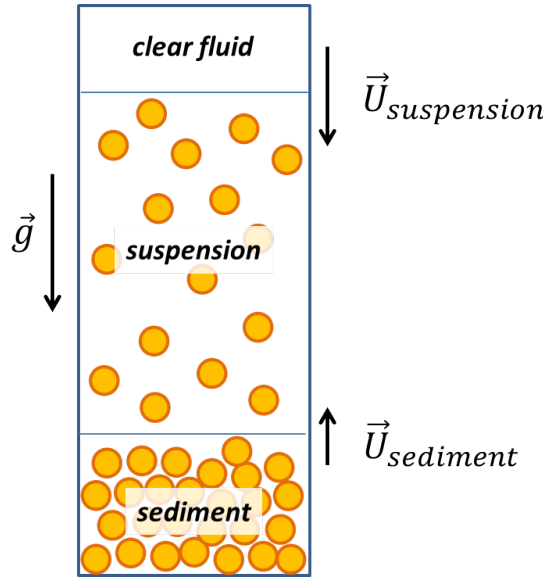


Figure 3.3: Sketch of the various regions during the sedimentation of the initially uniform suspension.

It turns out from experiments that an initially well-mixed suspension of non-Brownian particles sedimenting in a vessel with vertical walls can be separated into three distinct regions as illustrated in Figure 3.3. On the top a clear fluid phase is formed, while at the bottom a condensed phase approaching the maximum packing φ_{\max} grows. In the middle there is a suspension region having an approximately uniform initial volume fraction φ_0 . If we consider only the variation along the gravity direction z , the conservation of particles in all three regions is written as

$$\frac{\partial \varphi}{\partial t} + \frac{\partial (U_p f(\varphi) \varphi)}{\partial z} = 0. \quad (3.23)$$

Equation 3.23 is referred to as the *Kynch equation* which is a particular case of the nonlinear kinematic wave equation. Such an approach allows us considering the sedimentation as a wave propagation. The solution of Equation 3.23 indeed corresponds to a shock wave giving continuous but sharp transitions between homogeneous regions during the sedimentation. The velocity of the front between two

regions can be expressed as

$$U_{\text{front}} = U_p \frac{f(\varphi_2) - f(\varphi_1)}{\varphi_2 - \varphi_1}, \quad (3.24)$$

where the subscript 1 corresponds to the fraction ahead the shock and the subscript 2 is for values behind.

One can see that the velocity of the front between the clear fluid ($\varphi_2 = 0$) and the suspension ($\varphi_1 = \varphi_0$) is equal to the average sedimentation velocity of the particles discussed above

$$U_{\text{suspension}} = \langle U_s \rangle = U_p f(\varphi_0). \quad (3.25)$$

In the same way, we can evaluate the velocity of the front between the suspension ($\varphi_2 = \varphi_0$) and the immobile sediment ($\varphi_1 = \varphi_{\text{max}}$)

$$U_{\text{sediment}} = -U_p \frac{\varphi_0 f(\varphi_0)}{\varphi_{\text{max}} - \varphi_0}. \quad (3.26)$$

Measuring either of these two front velocities for various φ_0 is a commonly used experimental method for determining the average sedimentation speed and the settling function.

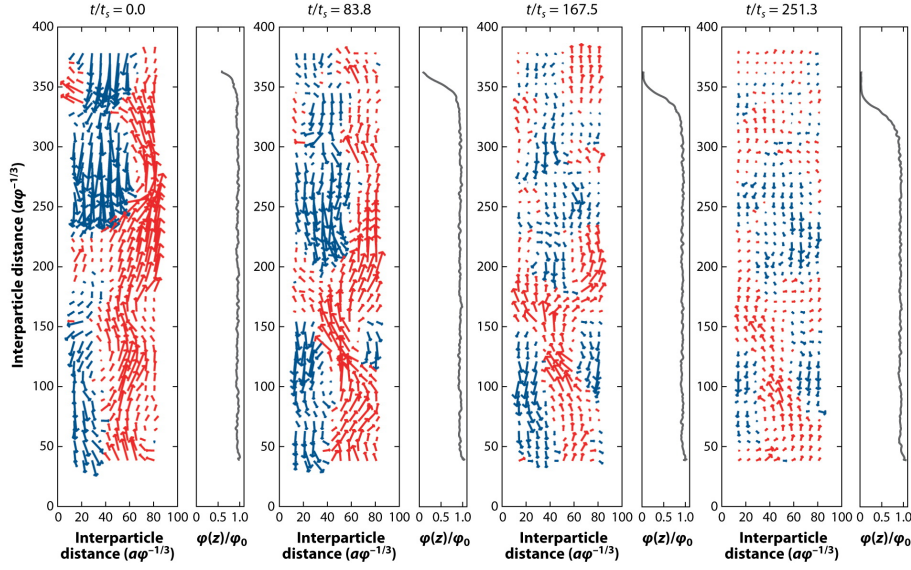
3.5 Velocity fluctuations

The average velocity explored in the previous section does not completely describe the motion of the particles. The long-range hydrodynamic interactions lead to a highly complex pattern of particle density fluctuations. The continuous change of suspension micro-structure causes the particle velocities to fluctuate significantly around its mean value.

The common tool to study these fluctuations is particle image velocimetry (PIV). In PIV a thin light-sheet is used to illuminate a layer of particles inside the cell. The movement of the particles is tracked by a camera and a 2D map of individual particle velocities is constructed. Then the velocity fluctuations are calculated by subtraction of the average sedimentation velocity from the measured velocity field $\delta \bar{U}_i = \bar{U}_i - \langle \bar{U}_s \rangle$. The examples of resulting fields are shown in Figure 3.4. One can see that the fluctuations are not distributed randomly but rather form correlated regions, or swirls. By analysing their spatial correlation function, the characteristic length scale of these swirls can be calculated. The amplitude of the fluctuations is usually estimated by the standard deviation of the velocity distribution $\Delta U = \sqrt{\langle \delta U_i^2 \rangle}$.

Some understanding of the relationship between the velocity fluctuations and size of correlation regions can be found by a scaling argument developed by Hinch [40]. Let us consider a blob of a characteristic size l having $N_l = \varphi l^3 / R^3$ particles. We expect that the random mixing produces statistical fluctuations in particle number of $\sim \sqrt{N_l}$. The arising fluctuation of the buoyancy force $\sqrt{N_l}(\rho_p - \rho)g \frac{4}{3}\pi R^3$ is balanced by a Stokes drag on the blob $6\pi\mu l \Delta U$. Then the amplitude of velocity fluctuations normalised by the Stokes velocity can be estimated as

$$\frac{\Delta U}{U_p} \sim \sqrt{\frac{\varphi l}{R}}. \quad (3.27)$$




 Guazzelli É, Hinch J. 2011.
 Annu. Rev. Fluid Mech. 43:97–116

Figure 3.4: Evolution of the velocity of fluctuations and a particle fraction profile with time. The time scale is the Stokes time $t_s = R/U_p$. The picture was obtained from [39].

The dominant fluctuation comes from the largest blob which should be equal in size to the smallest dimension of the vessel L

$$\frac{\Delta U}{U_p} \sim \sqrt{\frac{\varphi L}{R}}. \quad (3.28)$$

Thus the scaling law 3.28 predicts that the velocity fluctuations diverge with the container size. In reality, no divergence is seen, at least at a sufficiently long time after the beginning of the sedimentation. This experimental fact is often referred to a *divergence paradox* in literature.

Experiments show that at early stages just after the mixing of suspensions the large-scale velocity fluctuations are observed [41, 42]. They indeed follow the scaling suggested by Equation 3.27 with a swirl size comparable to L . These initial fluctuations are shown to exponentially decay with a characteristic relaxation time $\tau_{relax} \sim \frac{R}{U_p} \sqrt{\frac{L}{R\varphi}}$ to weaker small-scale fluctuations (see Figure 3.4). These small-scale fluctuations are part of the steady state and persist until the arrival of the upper sedimentation front. Segrè et al. found that the steady-state correlation length scales with the inter-particle distance $R\varphi^{-1/3}$ for particle fractions from 10^{-4} to 0.4 [43]. For sufficiently small containers ($L \leq 150R\varphi^{-1/3}$) the amplitude of velocity fluctuations ΔU was shown to increase with the container size L . For larger vessels ($L \geq 150R\varphi^{-1/3}$) the size of swirls does not depend on L and is about $\approx 20R\varphi^{-1/3}$. By substituting this length scale to Equation 3.27 one can get the following scaling for the velocity fluctuations

$$\frac{\Delta U}{U_p} \sim \varphi^{1/3}. \quad (3.29)$$

This result was shown to agree with the experimental data in the explored concentration range.

Another interesting peculiarity of the sedimenting suspensions is related to a large anisotropy of horizontal and vertical fluctuations. In the initial stages the amplitude of the vertical fluctuations is about four times higher than of the horizontal ones, in the steady state this difference drops to approximately two [39].

There are still open issues in the study of fluctuations in sedimenting suspensions. For example, what determines the size and magnitude of velocity fluctuations in the steady-state. More details of the current understanding of the problem can be found in [39].

The particle distribution can be modified by different other methods. The tilting of tubes induces formation of lanes and accelerates the sedimentation, a phenomenon known as the Boycott effect. An initial state having a particle-rich region at the top and a clear fluid at the bottom can be prepared by turning a container with condensed particles upside down. Such system undergoes a Rayleigh-Taylor instability. In the following sections we will consider these phenomena in more details.

3.6 Boycott effect

In the 1920s, an English medical scientist A. Boycott noticed that blood cells settle faster in inclined test tubes than in vertical ones [44]. In the inclined tubes particles need to settle a shorter distance than in the vertical ones (see Figure 3.5). As particles reach the bottom of the titled wall they slides down quickly. Such geometry leaves a thin layer of transparent fluid where the liquid back-flow can rise with less hydrodynamic resistance [38, 45]. These factors results in a several-fold acceleration of the sedimentation.

To estimate the magnitude of the Boycott effect the PNK model, presented by Ponder in 1925 [46] and, independently by Nakamura and Kuroda in 1937 [47], is widely used. The PNK model hypothesises that the thickness of the transparent fluid layer is tiny and does not change with time. The volumetric rate at which clarified liquid is produced equals the vertical sedimentation velocity $U_p f(\varphi)$ multiplied by the area of the horizontal interface at the top of the suspension plus the horizontally projected area of the surface between the suspension and the liquid layer. For settling between two parallel plates inclined by an angle θ and separated by a distance b the PNK model gives for the transparent fluid production rate

$$Q_l(t) = U_p f(\varphi) (b/\cos \theta + H \tan \theta). \quad (3.30)$$

Then the front velocity can be expressed as

$$\frac{dH}{dt} = -U_p f(\varphi) \left(1 + \frac{H}{b} \sin \theta \right). \quad (3.31)$$

By varying the angle of inclination θ and the aspect ratio H/b the front velocity can be made quite high.

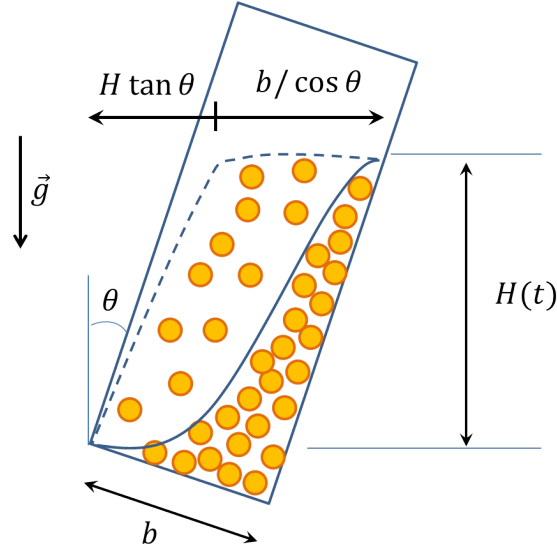


Figure 3.5: Sketch of the Boycott effect for the sedimentation between two parallel plates

3.7 Rayleigh-Taylor instability

The "classical" Rayleigh-Taylor (RT) instability occurs if a layer of a heavy fluid is placed on top of a lighter one. The system tends to minimise its potential energy and reverse the position of the fluids. It causes the growth of an unstable interfacial perturbation and the formation of "fingers". The formation of the RT instability is controlled by two competing mechanisms. The surface tension tends to suppress the perturbations increasing interfacial area, while gravity destabilises the system. As a result of this competition the modes with a wavelength smaller than a certain critical value $\lambda < \lambda_c$ are stable, while those with $\lambda > \lambda_c$ are unstable.

Recently the RT instability has been studied in a suspension of particles confined between two horizontal plates [48, 49]. The suspension was allowed to sediment towards the bottom wall. Once the particles had settled the experimental set-up was turned upside down. The spatial distribution of the particles was visualised by confocal microscopy. As one can see in Figure 3.6 the obtained fingering-like inhomogeneities of the system resemble the "classical" fluid-fluid RT instability.

There is no surface tension in this case and all perturbations are unstable ($\lambda_c = 0$). In the initial linear regime perturbations grow exponentially with time $\propto \exp(n(\lambda)t)$. The authors demonstrate that the growth rate $n(\lambda)$ exhibits a maximum at a finite wavelength λ_m . The experimental results were shown to be in a good qualitative and quantitative agreement with the results of simulations indicating that in the initial stages the fluctuations indeed increase in a linear regime. The influence of thermal motion was tested by using particles with different Peclet numbers around 1, the diffusion was shown to destroy the RT instability.

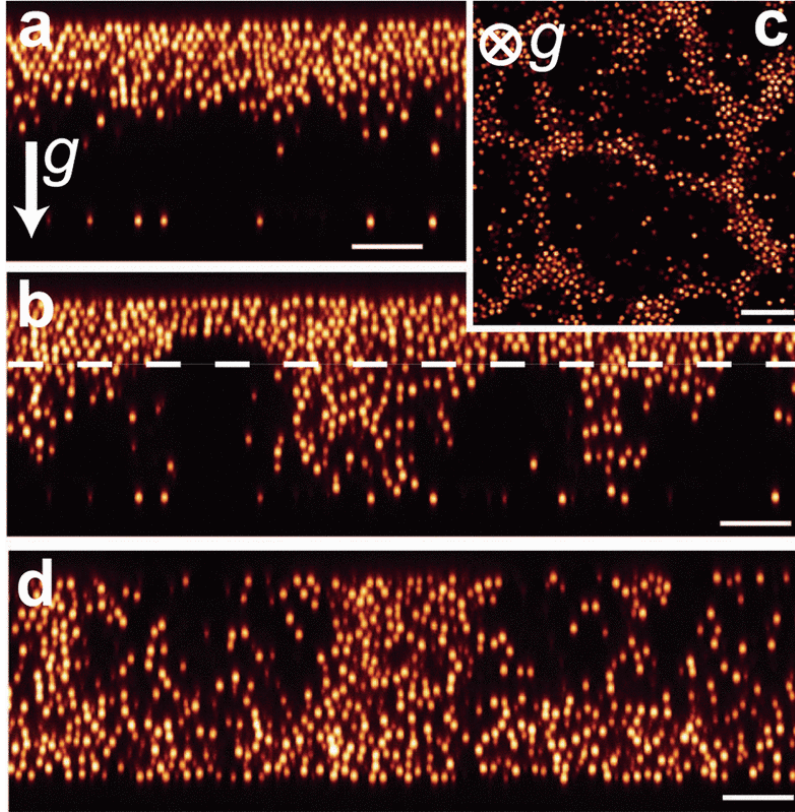


Figure 3.6: a),b),d) A series of images taken with a confocal microscope in a plane parallel to the gravity field at times $t/t_s = 3.2$ (a), 8 (b) and 14.4 (d). c) A slice perpendicular to the gravity at time $t/t_s = 11$. The scale bar is $20 \mu\text{m}$. The dashed line in (b) indicates the height of the slice in (c). The time scale is the Stokes time $t_s = R/U_p$. The picture is reproduced from [48].

3.8 Foam drainage

We will conclude this chapter by considering foam drainage, which is the flow of liquid through the foam due to the gravity force. The evolution of the liquid fraction in the foam towards its equilibrium is known as *free drainage*. The gravity-driven flow dries the foam at the top and accumulates the liquid at the bottom of the container resulting in a liquid fraction profile $\varepsilon(z)$ which evolves with time. Assuming that bubbles are incompressible we can write a mass conservation equation

$$\frac{\partial \varepsilon}{\partial t} + \nabla \cdot (\langle \bar{v}_l \rangle \varepsilon) = 0, \quad (3.32)$$

where $\langle \bar{v}_l \rangle$ is the mean liquid velocity at a given height. Equation 3.32 is valid if the foam volume is kept constant. For an unconfined foam, it has to be modified to take into account for foam expansion

$$\frac{\partial \varepsilon}{\partial t} + (1 - \varepsilon) \nabla \cdot (\langle \bar{v}_l \rangle \varepsilon) = 0, \quad (3.33)$$

which for dry foams is the same as the original mass conservation equation 3.32. As we will see later the liquid velocity $\langle \bar{v}_l \rangle$ can be expressed as a function of the liquid fraction and its gradient (and, of course, material parameters such as ρ, g, R, μ , etc.). Once velocity is determined it can be inserted into Equation 3.33 to get a partial differential equation describing the time evolution of the liquid fraction profile, known as the *drainage equation*.

The general approach to calculate the liquid velocity is to liken the system under investigation to a fluid flowing through a porous media [16] such as a packed bed of particles, for example. In the case of laminar flow, where inertia is negligible compared to the viscous drag, the liquid volumetric flux Q in such a flow can be well described by the integration of the Stokes Equation 3.13, which leads to

$$\frac{\bar{Q}}{S} = \langle \bar{v}_l \rangle \varepsilon = -\frac{K}{\mu} \nabla p_d, \quad (3.34)$$

where S is the cross-sectional area of the sample and K the permeability coefficient (measured in m^2). Equation 3.34 is known as *Darcy's law* [50] and is shown to describe well flows in pipes and in porous media at low Reynolds numbers. It is generally accepted that for foams K is proportional to the square of the bubble radius and can be expressed as

$$K = R^2 k, \quad (3.35)$$

where the dimensionless parameter k depends only on the liquid fraction and on the boundary conditions at the interfaces.

The main difference between a porous media and a foam is that the foam bubbles are elastic and that they can change their shape with the flow. It means that in the free drainage regime both the permeability and the pressure gradient vary with height. Another important difference is the boundary condition at the interfaces. In porous media a no-slip condition at the solid/liquid interface is commonly used,

while for foams the gas/liquid interfaces covered by surfactant can exhibit different rheological behaviour giving a rich variety of flow regimes.

In the following sections we will see how the pressure gradient and the permeability of foam can be predicted.

3.9 Pressure gradient in the foam

To describe the pressure drop in the foams a concept of *osmotic pressure* is generally used. Princen demonstrated that the osmotic pressure in foams can be introduced by analogy to the usual osmotic pressure in the context of solutions [51]. Let us consider a foam in contact with a liquid reservoir separated by a semi-permeable membrane: it is permeable for liquid but not for bubbles. To keep the liquid fraction constant an osmotic pressure must be applied to the membrane

$$\Pi = P_{\text{atm}} - p, \quad (3.36)$$

where p is the pressure in the liquid close to the membrane and P_{atm} is the atmospheric pressure. Using the osmotic pressure concept the driving pressure in Darcy's law 3.34 yields

$$\nabla p_d = \nabla p - \rho \bar{g} = -\nabla \Pi - \rho \bar{g} \quad (3.37)$$

Thermodynamically the osmotic pressure can be defined as the work required to extract a volume dV_l of liquid from the foam and to increase the total area of bubbles by dA_{tot}

$$-\Pi dV_l = \gamma dA_{\text{tot}}. \quad (3.38)$$

This equation can be rearranged in the following form

$$\Pi = -\gamma(1 - \varepsilon)^2 \frac{d(A_{\text{tot}}/V_g)}{d\varepsilon}, \quad (3.39)$$

where V_g is the volume of gas in the foam. This equation establishes a relationship between the change of the interfacial energy density A_{tot}/V_g with liquid fraction and the osmotic pressure. At the volume fraction corresponding to close packing ($\varepsilon = \varepsilon_{\text{max}}$) the bubbles are spherical, the energy density has a minimum, and consequently $\Pi(\varepsilon_{\text{max}}) = 0$. In the very dry limit $\varepsilon \rightarrow 0$ the osmotic pressure tends to infinity and in the intermediate range it decreases with the liquid fraction [52].

In dry foams ($\varepsilon \lesssim 0.01$), where Plateau borders are straight and can be characterised by a single radius of curvature R_{Pb} , the difference between the pressure inside a bubble P_b and the liquid around p can be written with Young-Laplace law as

$$P_b - p = \frac{\gamma}{R_{Pb}}. \quad (3.40)$$

In dry foams, the pressure in every bubble is approximately equal to the atmospheric one $P_b \approx P_{\text{atm}}$. Then the osmotic pressure is

$$\Pi = \frac{\gamma}{R_{Pb}}. \quad (3.41)$$

By expressing R_{pb} as a function of ε using Equation 2.8, we find for the Kelvin structure

$$\Pi \approx 0.57 \frac{\gamma}{R\sqrt{\varepsilon}}. \quad (3.42)$$

Recently a semi-empirical expression to the osmotic pressure Π , which agrees both with experimental results and simulations, was developed

$$\Pi = \alpha \frac{(\varepsilon_{\max} - \varepsilon)^2}{\sqrt{\varepsilon}} \frac{\gamma}{R}. \quad (3.43)$$

with $\alpha = 7.3$, $\varepsilon_{\max} = 0.26$ for monodisperse ordered foams [53] and $\alpha = 3.2$, $\varepsilon_{\max} = 0.36$ for monodisperse disordered ones [54]. This expression gives right limits both for dry and wet foams and can be used in the whole range of liquid fractions from almost 0 to ε_{\max} .

3.10 Forced drainage

Free drainage may seem to be the most simple experiment to study foam permeability. However, in this case the obvious solution is not the best one, since regions of very different liquid fraction (and, consequently permeability and osmotic pressure) are present simultaneously. Moreover, free drainage usually takes a lot of time, so other ageing processes, such as a coalescence of bubbles or coarsening, can be important.

Instead, a *forced drainage* experiment can be performed, where the foaming solution is continuously added at a constant flow rate from the top of the foam that has already been allowed to drain freely. A sharp wetting front develops downwards at a constant velocity u_{front} which is easy to measure. Above the front the liquid fraction ε is uniform and does not evolve with time. This situation is similar to the shock wave particle sedimentation. Indeed, it turns out that the drainage equation can have a solitary wave as its solution, just as the Kynch equation 3.23. For dry foams ($\varepsilon \lesssim 0.1$) the velocity of the front is approximately equal to the velocity of the liquid above the front $u_{\text{front}} \approx \langle \bar{v}_l \rangle$. For higher liquid fractions this approximation is generally not true because the front velocity is usually measured in the laboratory framework and does not take into account the upward movement of bubbles due to foam expansion. However, for small liquid fractions this effect can be neglected.

Above the front, the system is in a steady state. Here only gravity and viscous forces are important, the osmotic pressure is constant everywhere. Then the front velocity can be written from Darcy's law as [16]

$$u_{\text{front}} \approx \frac{R^2 k \rho g}{\varepsilon \mu}. \quad (3.44)$$

The liquid fraction above the front can be easily calculated from the experimental data as

$$\varepsilon = \frac{Q_l}{S u_{\text{front}}}. \quad (3.45)$$

Finally, the foam permeability can be calculated from forced drainage data using Equations 3.45 and 3.44. By varying the incoming liquid flux, different liquid fractions can be tested and the $k(\varepsilon)$ dependence can be experimentally determined and compared with theoretical predictions.

3.11 Modelling the permeability of a foam

The flow of liquid through the foam can be considered as a flow through the network of Plateau borders and nodes. The liquid flow through films can usually be neglected. For dry foams the volume of nodes is negligible and dissipation mainly occurs in Plateau borders. Foam in this case can be modelled as a network of randomly oriented channels with constant flow resistance. For wetter foams the nodes should be taken into account. In the limiting node-dominated case it is presumed that there are no viscous losses in the Plateau borders and dissipation occurs mainly in the nodes.

Channel-dominated model The starting point of channel-dominated model is to consider a flow through a single Plateau border. We consider a straight Plateau border with a cross-sectional area A_{Pb} and a length l , oriented at an angle θ to the vertical axis z (see Figure 3.7). A flow through the Plateau border can be described by Darcy's law. For the mean liquid velocity in the Plateau border $\langle \bar{v}_{Pb} \rangle$ one has [16]

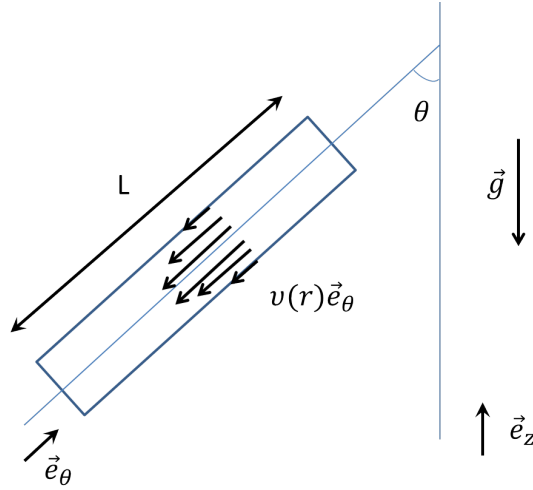


Figure 3.7: A sketch of the liquid flow inside a Plateau border inclined by angle θ to the vertical axis z . The velocity field is $\bar{v} = v(r)\bar{e}_\theta$, where r is the radial coordinate.

$$\langle \bar{v}_{Pb} \rangle = -\frac{k_{Pb}A_{Pb}}{\mu} \left(\frac{dp}{dz} + \rho g \right) \cos \theta \bar{e}_\theta, \quad (3.46)$$

where k_{Pb} is the permeability coefficient for a single Plateau border. The last depends not only on the geometry of the pipe but also on the mobility of the interface.

The coupling between the surface and bulk flows can indeed change the surface velocity and modify the velocity profile in the Plateau border. In Chapter 1 we have discussed that the mechanical response of interfaces can be characterised by 4 parameters, namely dilational and shear surface elastic modulus and dilational and shear surface viscosities. It turns out that, for the description of the foam drainage, the shear surface viscosity is the most important one [16]. Quantitatively, the coupling between bulk and surface flow can be described by the dimensionless *Boussinesq number* which is a ratio between the characteristic surface and bulk stresses

$$Bo = \frac{\mu_s}{\mu R_{Pb}}, \quad (3.47)$$

where μ_s is a surface shear viscosity. Depending on the Boussinesq number, two limiting cases should be considered:

- For $Bo \ll 1$, the interfaces are *mobile*, the surface velocity is equal to the bulk one. The velocity profile is close to a *plug flow*.
- For $Bo \gg 1$, the interfaces are *rigid*, the surface velocity is zero. The velocity profile is close to a *Poiseuille flow*.

The permeability of a single Plateau border as a function of Bo can be approximated by the following analytical expression [55]

$$k_{Pb} = \frac{1}{6} \left[\frac{3}{25} + \sqrt{\frac{2}{Bo}} \arctan \sqrt{\frac{1}{8Bo}} - \arctan \frac{1}{2\pi Bo} \right]. \quad (3.48)$$

In the limit of rigid interfaces k_{Pb} tends to 0.02.

The mean liquid velocity in the foam $\langle \bar{v}_l \rangle$ can be obtained by averaging the z projection of $\langle \bar{v}_{Pb} \rangle$ over all orientations. Assuming that the Plateau borders are randomly oriented, the probability of its being inclined at an angle between θ and $\theta + d\theta$ is $\sin \theta d\theta$. Thus the mean liquid velocity $\langle \bar{v}_l \rangle$ is

$$\langle \bar{v}_l \rangle = -\frac{k_{Pb} A_{Pb}}{\mu} \left(\frac{dp}{dz} + \rho g \right) \int_0^{\pi/2} \cos^2 \theta \sin \theta d\theta = -\frac{k_{Pb} A_{Pb}}{3\mu} \left(\frac{dp}{dz} + \rho g \right). \quad (3.49)$$

By comparing this expression with Equation 3.34, we finally get the permeability in the channel-dominated model as

$$K = \frac{k_{Pb} A_{Pb} \varepsilon}{3}. \quad (3.50)$$

Using Equations 2.4 and 2.8, the permeability can be shown to be proportional to ε^2

$$k \approx 0.16 k_{Pb} \varepsilon^2. \quad (3.51)$$

In the case of completely rigid interface ($k_{Pb} = 0.02$) the permeability becomes

$$k \approx 3.2 \cdot 10^{-3} \varepsilon^2. \quad (3.52)$$

Due to its simplicity, this expression is often used to estimate the permeability of the foam in a wide range of liquid fractions even if it is rigorously valid only for dry foams.

Node-dominated model Drainage of dry foams with rigid interfaces is usually reasonably well described by a channel-dominated model [56, 57]. But for both mobile interfaces and for wetter foams experimental agreement is poor. In such foams the dissipation in nodes has to be accounted for. However, the complexity of node geometry makes the detailed description of the problem quite complicated. Each node is connected with four Plateau borders and, depending on the node orientation, the flow through a Plateau border can go either into or out of the node.

A qualitative prediction for the node-dominated model can be made on the base of simple scaling arguments [58, 59]. Let us consider a foam network unit consisting of a Plateau border and two quarter nodes. The viscous losses in the nodes scale with $\mu\langle\bar{v}_l\rangle/R_{Pb}^2$. The volume of the nodes V_n is proportional to R_{Pb}^3 , while the total volume of one unit V_{unit} scales like LR_{Pb}^2 , where L is a node-to-node distance. The volume integral of the Stokes equation can be written as

$$\int_{V_{unit}} \nabla p_d dV = \int_{V_{Pb}} \mu \Delta \bar{v} dV + \int_{V_n} \mu \Delta \bar{v} dV, \quad (3.53)$$

where V_{Pb} is a volume of the Plateau border. Assuming that the viscous dissipation in the Plateau borders is smaller than in the nodes and using the above-mentioned scaling, one gets for the mean liquid velocity

$$\langle\bar{v}_l\rangle \sim \nabla p_d L R_{Pb} / \mu. \quad (3.54)$$

If the liquid fraction is not high, we can use Equations 2.6 and 2.8 to link L and R_{Pb} with the bubble radius R . Then the permeability becomes

$$k \sim \varepsilon^{3/2}. \quad (3.55)$$

In the node-dominated case the permeability scales as $\varepsilon^{3/2}$ instead of the ε^2 dependence found in a channel-dominated model. Several experimental results indeed show that in some systems the permeability varies as $\varepsilon^{3/2}$ indicating the domination of the viscous dissipation in nodes, while in others a ε^2 dependence is experimentally observed [56, 57].

Mixed models To improve agreement of theory with experiment some mixed models which take into account permeabilities both in Plateau borders and in nodes have been proposed [19, 20]. Unfortunately, no analytical expression for k is available. But, recent semi-empirical expressions describing experimental data very well in a wide range of liquid fractions were proposed [60] for both limits of mobile and rigid interfaces

$$k(\varepsilon) = \frac{\varepsilon^{3/2}}{425(1 - 2.7\varepsilon + 2.2\varepsilon^2)^2} \quad (\text{mobile interface}), \quad (3.56)$$

$$k(\varepsilon) = \frac{\varepsilon^2}{312(1 - 2.15\varepsilon + 1.37\varepsilon^2)^2} \quad (\text{rigid interface}). \quad (3.57)$$

We will see in Chapter 7 how these expressions can help us to describe the liquid flows in foams during generation.

Chapter 4

Antifoaming agents

Foams are present in various forms in our daily lives as soft solids or fluids in food and beverage products or in insulating materials as solids. On the other hand; in other applications (paper and paint industry) foam formation can cause serious problems. Also for some industrial processes the foam should be created and then rapidly destroyed (for example, for flotation). In these cases suitable *antifoaming agents* (molecules or particles that stop solutions from foaming) need to be used [16]. Despite the abundance in applications, the mechanism of foam destruction by antifoams is still poorly understood.

In this short introduction we will focus our attention only on the oil-based antifoams which are widely used in technical applications and are extensively studied [61–65]. Highly efficient antifoams used in industry typically consist of silicone oil emulsion droplets containing hydrophobic nanoparticles. Being dispersed in the foam, they can destroy a large volume of foam within a few seconds.

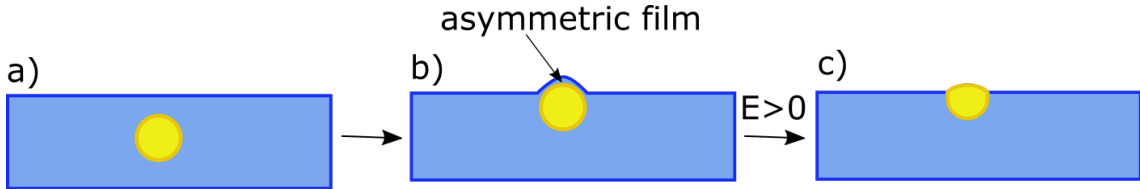


Figure 4.1: Sketch of the drop entry. a) An antifoam globule in the foaming solution. b) Formation of the asymmetric gas-water-oil film. c) Formation of the oil lens at the interface.

To be effective, an antifoam globule dispersed in the foam should first reach an interface between foaming solution and gas (see Figure 4.1). Foaming solution is usually an aqueous phase, so for brevity we will call it water in the following. The energy gain of the droplet emergence at the interface is described by the *entry coefficient*

$$E = \gamma_{gw} + \gamma_{ow} - \gamma_{og} \quad (4.1)$$

where γ_{gw} , γ_{ow} and γ_{og} are the gas-water, oil-water and oil-gas interfacial tensions, respectively. The emergence corresponds to positive values of the entry coefficient,

$E > 0$. Oils having a negative entry coefficient cannot enter the interface and are inactive as antifoams.

The entry coefficient only tells us if the emergence is thermodynamically allowed. The positive value of E does not guarantee the appearance of the antifoaming droplet at the interface because the kinetic *drop entry barrier* is also important - a high barrier can prevent the particle from entering. This barrier arises from the stability of the asymmetric gas-water-oil film which appears when the droplet approaches the interface (see Figure 4.1). Quantitatively, the kinetic barrier is usually discussed in terms of a *critical capillary pressure* P_c^{cr} , which is the pressure necessary to collapse the asymmetric film [62]. The drop entry barrier can be measured experimentally by the film trapping technique. Experiments show that P_c^{cr} depends on various parameters, such as the chemical nature of the oil, the addition of electrolytes, the droplet size, etc. The presence of hydrophobic nanoparticles in the oil can significantly decrease the drop entry barrier: nanoparticles adsorbed at the oil-water interface can help pierce the asymmetric film making it less stable.

Depending on the entry barrier and the characteristic time of foam destruction antifoams can be divided into two families:

- *Fast antifoam* droplets, having P_c^{cr} less than approximately 15 Pa, act in the foam films and destroy them within seconds. They significantly decrease the foamability of the solution and destroy completely the foam in less than 1 minute after the end of generation.
- *Slow antifoam* droplets with P_c^{cr} more than 15 Pa are immediately expelled from the films to the Plateau borders and nodes. They act only once the Plateau border walls and nodes shrink sufficiently due to the foam drainage and start to compress the globules. The foam destruction by slow antifoams takes from tens of minutes to hours.

Mechanism of foam destruction by fast antifoams Once the fast antifoam globule enters the interface, it can destroy the film between the bubbles by various mechanisms: *bridging-stretching*, *bridging-dewetting* and several *oil-spreading* mechanisms [62].

In the bridging mechanisms the oil droplet first forms an oil lens on one of the interface. The foam film rapidly drains due to the capillary pressure difference between the film and the adjacent Plateau borders. In a few milliseconds the film reaches a thickness comparable with the antifoam droplet size ($\sim 1 \mu m$) [16]. Then the antifoam globule touches both interfaces of the foam film forming a "bridge" between them (see Figure 4.2). The mechanical stability of the formed bridge is described by the bridging coefficient, introduced by Garrett [66]

$$B = \gamma_{gw}^2 + \gamma_{ow}^2 - \gamma_{og}^2 \quad (4.2)$$

It was proven theoretically that for positive values of B the bridges are mechanically unstable, while oils with $B < 0$ form stable bridges which does not cause film rupture.

In the bridging-stretching mechanism the unstable bridge ($B > 0$) stretches in the radial direction due to uncompensated capillary pressure. This process leads to

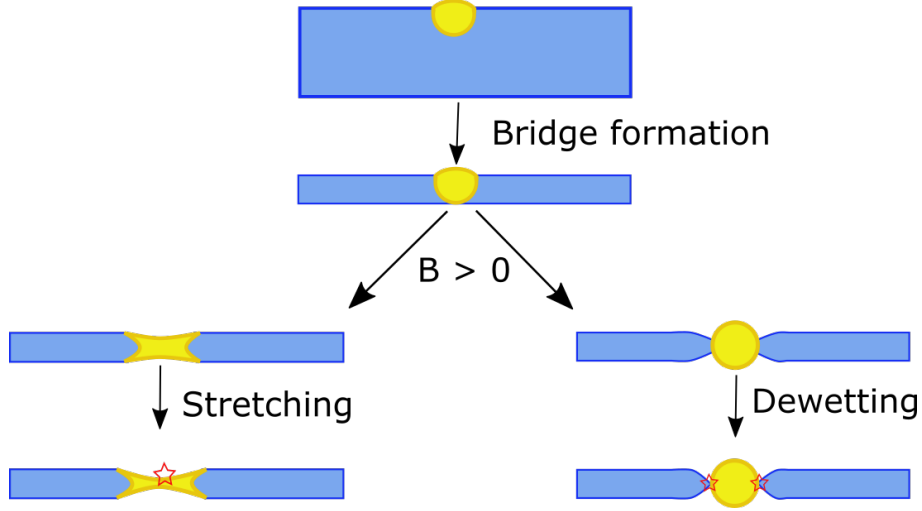


Figure 4.2: Schematic representation of the bridging-stretching (on the left) and bridging-dewetting (on the right) mechanisms.

the formation of a thin unstable oil film in the center of the bridge as illustrated in Figure 4.2. The rupture of this film destroys the whole foam film. An important requirement for this mechanism is the deformability of the oil droplets.

Alternatively, the bridging-dewetting mechanism can be realised. In this case the bridge has no time to deform and the aqueous phase dewets hydrophobic oil droplet surface leading to the rupture at the oil-water connection (see Figure 4.2).

It seems that both bridging mechanisms are possible in real systems. So far, it is not very clear how a given system choose a preferred mechanism: it should be related with the velocities of lens dewetting and lens deformation [62].

The possibility of the *oil-spreading* mechanism was also intensively discussed in the literature [16]. According to this mechanism, the oil from the lens rapidly spreads over the foam film interface as illustrated in Figure 4.3. The oil spreading induces a Marangoni-driven flow of liquid directed radially from the lens. This effect leads to local film thinning and its rupture. Quantitatively, the possibility of the spreading mechanisms can be estimated by the *spreading coefficient*

$$S = \gamma_{gw} - \gamma_{ow} - \gamma_{og} \quad (4.3)$$

where positive value of S corresponds to the oil spreading case. However, so far it is not proven that this mechanism can be encountered in the real systems [62].

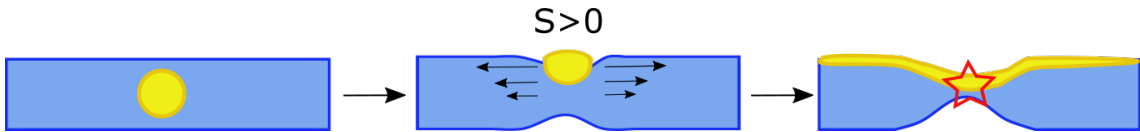


Figure 4.3: Schematic representation of the oil-spreading mechanism.

Mechanism of foam destruction by slow antifoams Slow antifoams cannot enter the interface without an additional compressive force due to a high entry barrier. After the end of generation, slow antifoam globules are expelled from films and they get stuck in the Plateau borders and nodes. At this stage they do not influence the foam stability. The foam drains in the gravity field and as the Plateau borders and nodes shrink at the top of the foam, they start to squeeze the trapped antifoam droplets (see Figure 4.4). When the compressing pressure exceeds the critical capillary pressure, the droplet emerges at the interface.

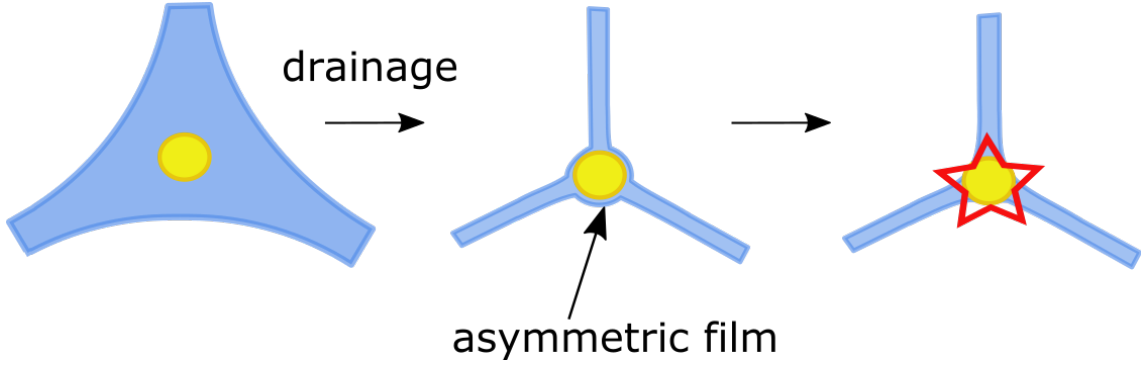


Figure 4.4: Schematic representation of the foam destruction by slow antifoams.

The detailed mechanism of foam destruction after the globule entry still remains unclear for slow antifoams [62, 65]. It can be either bridging or spreading, or a combination of both. Another interesting peculiarity of slow antifoams is that a single destruction event induces a strong mechanic agitation in the adjacent Plateau borders. This shock provokes entry of other antifoam globules causing an avalanche of collapses. One drop entry event can therefore trigger the destruction of thousands of bubbles [62].

There are still open issues in the physics of antifoams. The condition determining the choice of the microscopic mechanism is still not very clear. Also almost all research assume that the antifoam globule is already in the active zone (a film for fast antifoams or a Plateau border for slow ones), usually neglecting how the antifoam reaches it (except in [61]). In this thesis we will shed some light on the importance of the transport phenomena for fast antifoams.

Part II

Materials and methods

Chapter 5

Materials and Methods

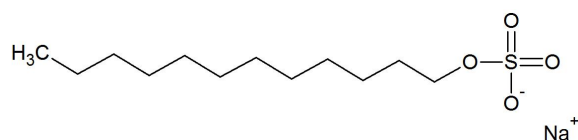
5.1 Materials

In the present work all solutions are prepared with deionized Milli-Q water. Absence of impurities is checked by conductivity measurements (18.2 M Ω for pure water).

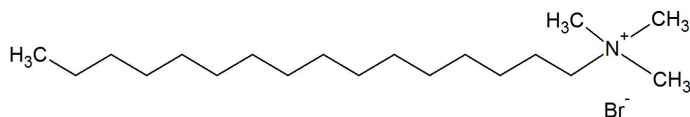
Different electrolytes are used: sodium bromide (NaBr), sodium chloride (NaCl). To produce foam nitrogen is used as a gas. To avoid coarsening of bubbles small traces of water-insoluble perfluorohexane (C₆F₁₄) are added.

Several types of surfactants are used:

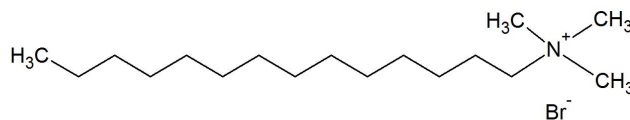
- Sodium dodecyl sulfate (SDS) C₁₂H₂₅SO₄Na



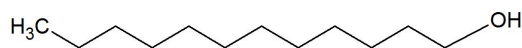
- Hexadecyl trimethyl ammonium bromide (CTAB) C₁₉H₄₂NBr



- Tetradecyl trimethyl ammonium bromide (TTAB) C₁₇H₃₈NBr



- dodecanol C₁₂H₂₆O



All chemicals were purchased from Sigma-Aldrich.

An antifoaming agent Silcolapse RG22 was kindly provided by Bluestar Silicones. The antifoam is composed of an oil in water emulsion (20% oil) with a drop radius about $5\ \mu\text{m}$ with a small fraction of hydrophobic silica particles (ratio of oil to silica 24:1). The density of the droplets is around $1050\ \text{kg/m}^3$. It is very efficient and can destroy large amount of foam within few seconds.

Polystyrene particles with density $1050\ \text{kg/m}^3$ and different diameters from 10 to $40\ \mu\text{m}$ were a gift from Microbeads.

5.2 Sample preparation

To perform surface tension measurements all chemicals are additionally purified. All inorganic salts are roasted at $750^\circ\ \text{C}$ for several hours in order to remove organic impurities. CTAB is recrystallized from an ethanol/water mixture. Absence of impurities is checked by measuring surface tension of pure water ($72.0\ \text{mN/m}$ at $25^\circ\ \text{C}$) before each experiment.

All glassware is cleaned by heating at $50^\circ\ \text{C}$ in Deconex cleaning solution, then rinsing thoroughly at least 10 times with distilled and 3 times with deionized water.

All SDS solutions are used within two weeks after preparation to avoid hydrolysis. All particle dispersions are ultrasonicated after preparation and before each experiment to avoid any particle aggregation.

5.3 Surface tension measurements

The surface tension is measured by bubble/drop profile analysis tensiometry. This method is based on the determination of surface tension from the analysis of the bubble profile. In a gravity field the bubble shape is determined by the combination of two competing forces. The gravity force tends to elongate the bubble and the surface tension of the liquid tends to make the drop spherical, i. e. contract the bubble. Mechanical equilibrium for two homogeneous fluids separated by an interface is described by the Gauss-Laplace equation:

$$\gamma \left(\frac{1}{R_1} + \frac{1}{R_2} \right) = \Delta P_0 + \Delta \rho g z, \quad (5.1)$$

where γ is an interfacial tension, ΔP_0 is a pressure difference between liquid and gas at the bubble apex, $\Delta \rho$ is a density difference between the two bulk phases, g is the gravitation constant and z is a vertical coordinate of point on the drop surface counted from the drop apex along the center line of the drop (see Figure 5.1), R_1 and R_2 are the two principal radii of curvature.

Using the Gauss-Laplace equation a theoretical drop/bubble profile can be numerically integrated and compared with one experimentally measured. Such an approach allows the surface tension to be determined.

In this thesis a commercial device Tracker (Teclis, France) is used. Principal schema of the equipment is presented in Figure 5.2.

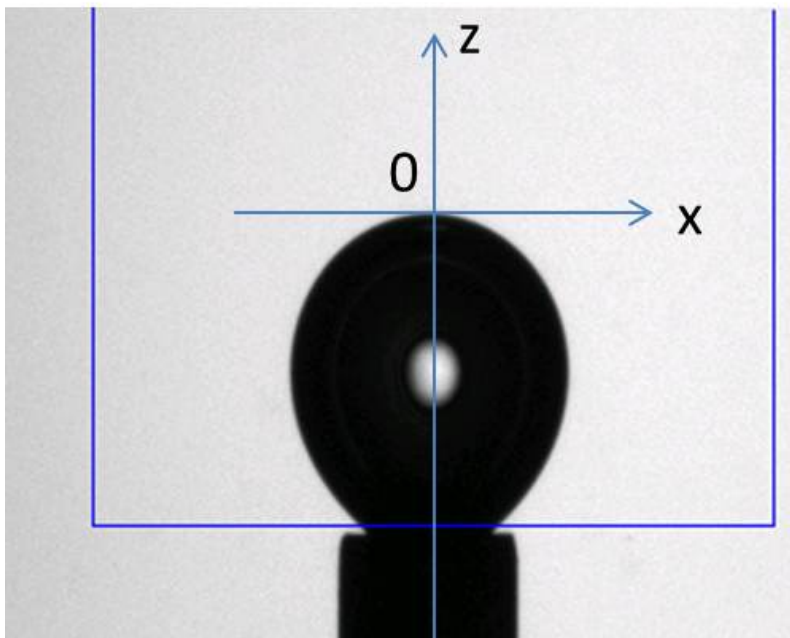


Figure 5.1: Profile of a rising bubble at the end of a capillary

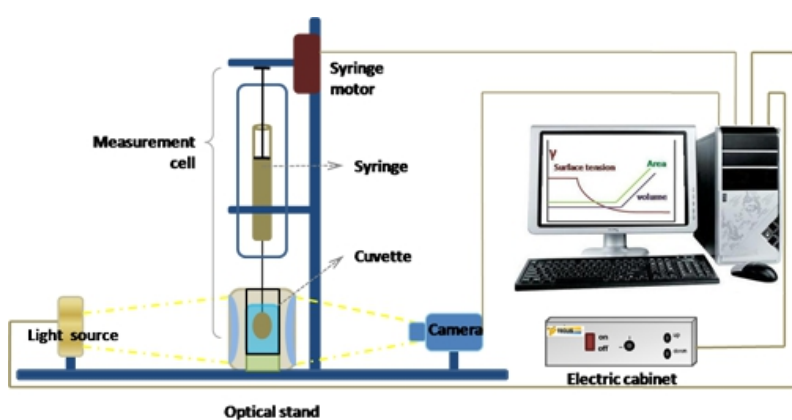


Figure 5.2: Principal schema of the Tracker tensiometer (Teclis, France).

The rising bubble configuration is used in order to avoid bulk depletion effects. The rising bubble is created at the end of a needle having a U form, and the syringe injects air into the surfactant solution under the control of a motor. The air bubble is illuminated with uniform light and the bubble image is obtained by a CCD camera equipped with telecentric lenses. The software provided by with the device automatically analyses photographs and calculates the surface tension.

Different measurement plans can be chosen depending on the experiments to be performed. In a measurement plan, one executes controlled variations of one of the physical quantities (the drop volume, interface area or tension) and records the response of the other physical quantities versus time.

The experimental cell is maintained at a fixed temperature by circulating water.

5.4 Methods of foam generation and characterization

5.4.1 FoamScan

A commercially available device Foamsan (Teclis, France) is used to generate and characterize foams. This machine produces foam by blowing gas through a porous plate at a controlled gas flow rate. Frits with different sizes of pores can be used to get various bubble sizes. The flow rate can be varied from 10 to 400 ml/min. After generation the foam rises in a square column with sides 2.5×2.5 cm and a height of about 32 cm. A video camera connected with a computer follows the position of the foam height and from this the foam rising velocity is calculated.

The cell is equipped with six pairs of electrodes to measure a reference electrical conductivity of the liquid at the bottom of the cell σ_l and a foam conductivity σ_f at five different positions. To avoid electrolysis of the foam, an alternating current of 1 V at 1kHz is applied. At the chosen frequency the capacitance of the foam can be neglected and the active resistance can be directly measured [16].

The measure of electrical conductivity is a powerful tool to determine the foam liquid fraction ε defined as the ratio between the volume of liquid and the total volume of the foam. An empirical relation is used to calculate ε from experimentally measured relative conductivity of the foam $\sigma = \sigma_{\text{foam}}/\sigma_{\text{liquid}}$ [67]

$$\varepsilon = \frac{3\sigma(1 + 11\sigma)}{1 + 25\sigma + 10\sigma^2}. \quad (5.2)$$

It has been shown that this relation perfectly describes experimental data for the whole range of ε and σ , both ranging from 0 to 1.

5.4.2 Measurement of the bubble size

To measure the bubble size distribution a sample of foam is collected from the Foamsan column and squeezed between two glass plates separated by $h = 150 \mu\text{m}$ (Figure 5.3). The cross-sectional area A_b of the squeezed bubble is measured from photos. Assuming volume conservation, the radius R of each bubble can be easily calculated [56]

$$R = \sqrt[3]{\frac{3A_b h}{4\pi}}, \quad (5.3)$$

In this thesis the bubble size distribution is usually characterised by the mean Sauter radius $R_{32} = \langle R^3 \rangle / \langle R^2 \rangle$.

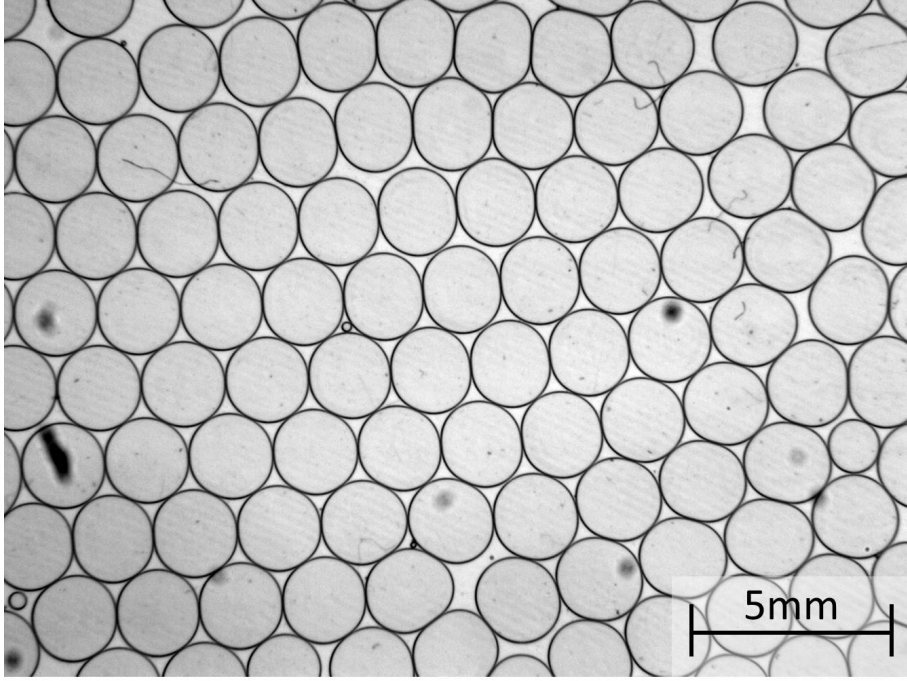


Figure 5.3: Photograph of bubbles squeezed between two plates

5.4.3 Hele-Shaw cell

To study quasi-2D foams (monolayers of bubbles squeezed between two plates) a home-made Hele-Shaw cell was developed (see Figure 5.4). The cell consists of two vertical plexiglas plates with dimensions 10×50 cm. The distance H between the two plates can be slightly varied but it is typically about 2 mm. The foam is produced by blowing gas through a single orifice into a foaming solution. Three pairs of electrodes, connected with the Foamscan set-up, measure the conductivity at different foam heights. Before each experiment the cell is filled with the foaming solution to have a reference conductivity σ_l .

To vary the liquid fraction over a wide range, the experiments can be performed in a forced drainage regime: foaming solution is added from the top of the foam at a constant flow rate Q . The liquid fraction can be adjusted using different liquid flow rates: a higher flow rate results in a higher liquid fraction [52]. In our experiments we vary the liquid flow from 4 ml/h to 500ml/h. This flow rate range allows us to get both very dry and very wet quasi-2D foams. The forced drainage regime significantly simplifies our investigation providing us with a liquid fraction which is not only constant with time but also throughout the entire foam. A steady-state, defined by constant conductivity, is reached before each measurement.

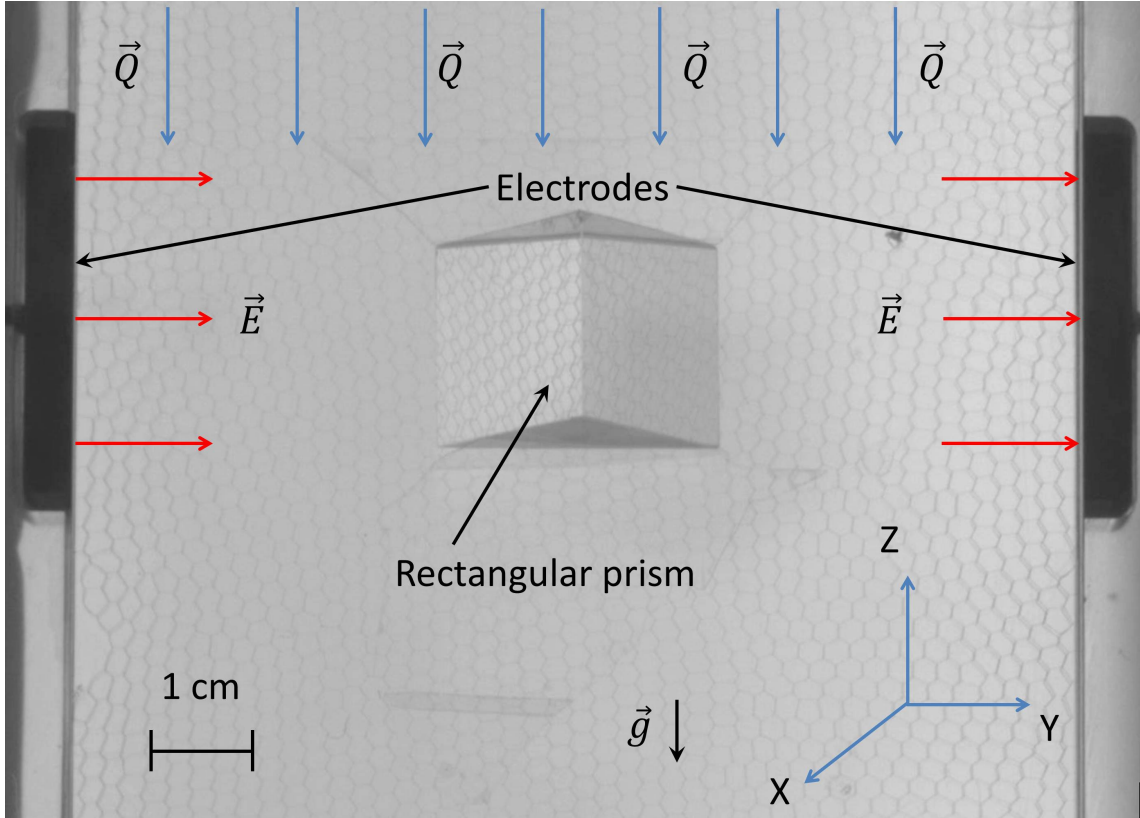


Figure 5.4: Photograph of the experimental Hele-Shaw cell. A pair of electrodes allows to measure the electrical conductivity. A rectangular prism in the center of the cell is used to take the high-resolution photos of the surface Plateau border network. Foaming solution is injected at constant flow rate Q at the top of the cell to control the liquid fraction of the foam.

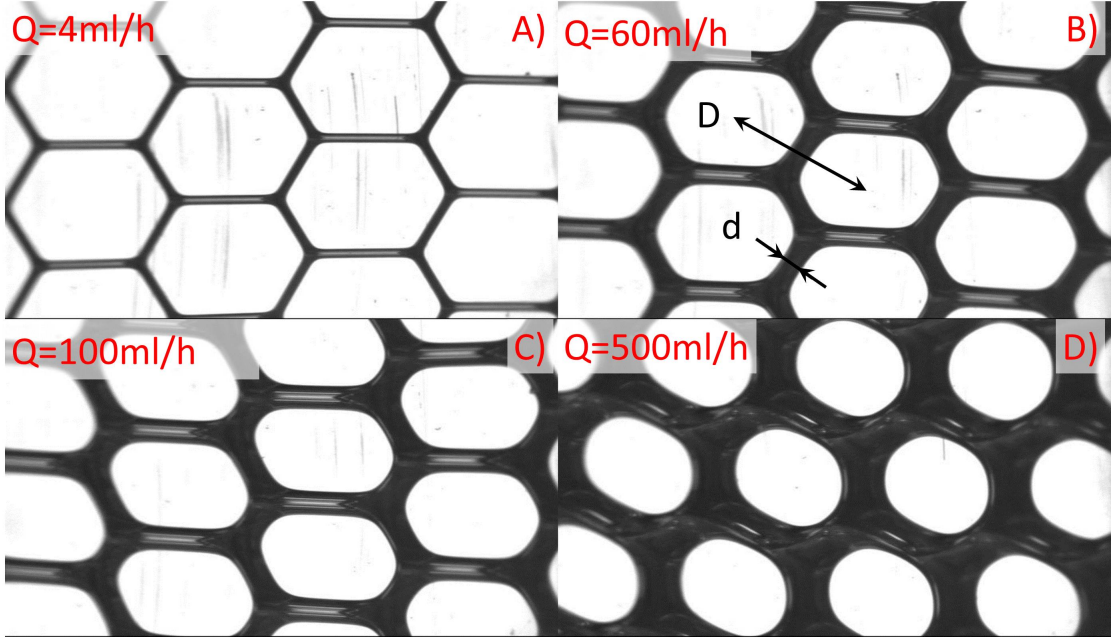


Figure 5.5: High-resolution photographs of vertical quasi-2D foams corresponding to different liquid flow rates: A) $Q = 4$ ml/h B) $Q = 60$ ml/h C) $Q = 100$ ml/h D) $Q = 500$ ml/h. The thickness d of the surface Plateau border and the bubble diameter D are indicated.

The thickness of the wetting films h_{wf} between the bubbles and the confining plates is calculated from the reflected light spectrum measured by an USB 400 Ocean Optics spectrometer. It was found that in our experiments h_{wf} shows negligible dependence on the flow rate of the liquid and is constant at $3 \pm 1 \mu\text{m}$ within experimental error. Assuming that the contribution of the wetting film conductivity is directly proportional to this thickness we subtract it systematically from the experimentally measured value of the relative conductivity σ_m to have a pure signal from the foam

$$\sigma = \sigma_m - \frac{2h_{wf}}{H}. \quad (5.4)$$

High-resolution photographs of the foam are made with a CCD camera equipped with a telecentric lens through a rectangular prism glued to the outside of the container wall (see Figure 5.5). This technique was first proposed by Garrett et al. (cited in [68]). Slight deviations in the path of light reflected by the curved interfaces of the Plateau borders avoid that this light enters the camera. The full surface Plateau border network appears therefore in black. The described optical configuration provides us with reliable information on the foam structure. Each image is treated with ImageJ software to get an average distance D between the centres of the adjacent bubbles and an average surface Plateau border thickness d as shown in Figure 5.5. In the case of dry foams D corresponds to the bubble size. Also a fraction of the surface covered by water $\varepsilon_{surface}$ is calculated for each image.

5.5 Parabolic flights

5.5.1 Principle of parabolic flights

To study foams in microgravity conditions we profited from a parabolic flight campaign organised by Novespace and financed by CNES (French Space Agency). Novespace is a private company possessing their own Airbus A300 Zero-G specially configured to perform parabolic flights. The aircraft has seats in the front and tail parts, while the central part is empty to install scientific equipment. Each flight is considered as a test flight and is completely controlled by DGA Essais en Vol (a subdivision of French Ministry of Defence).

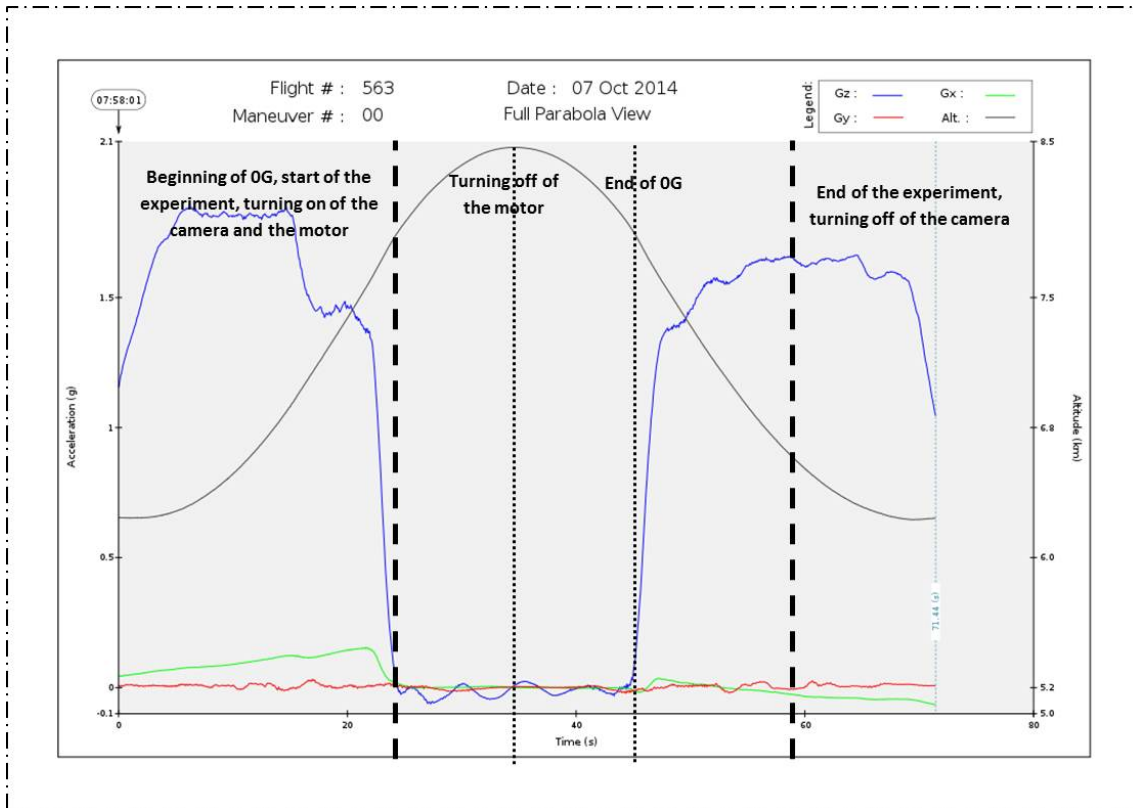


Figure 5.6: Typical altitude (grey line) and acceleration profiles during a parabolic manoeuvre. The acceleration is measured along 3 axes: x (green curve) going from tail to front of the aircraft, y (red curve) going from left to right wings and z (blue curve) perpendicular to the aircraft floor. Different experimental stages are shown by dashed lines.

In the parabolic flight the aircraft with research equipment and experimentalists performs manoeuvres following an approximately parabolic path. Typical altitude and acceleration profiles inside the aircraft are shown in Figure 5.6. Each parabola can be divided in three parts. First of all, the aircraft flies horizontally (just as in a classic flight), then it lifts up its nose till 45° . During this phase, taking about 20 s, people feel the acceleration equal to $1.8 g$. Then the pilot starts to follow the parabolic curve and gravity abruptly goes almost to 0 within 5 s. People and

payload are now in free fall during next 22 s. In this phase the remaining gravity can slightly vary but does not exceed $\pm 0.03 g$ allowing the microgravity experiments to be performed. When the aircraft reaches the angle of incidence of 45° , the pilot gets the plane out of the parabola. Acceleration increases to $1.8 g$ and remains high for 20 s. Then the aircraft stabilizes its flight and starts the next manoeuvre.

During a flight the plane performs 31 parabolas with some rest phases of about 5 minutes every 5 parabolas, during which the aircraft remains in steady flight and experimenters can realize any adjustments of their experimental devices.

5.5.2 The experimental set-up

A home-made set-up was used to generate and study foam in microgravity conditions. The experiment is made out of 45x45 aluminium Bosch profiles to meet the safety requirements (See Figure 5.7). The overall dimension of this rack is 106x101x80 cm and the weight is about 120 kg full. The rack was kindly borrowed from Dr. Hervé Caps (University of Liège, Belgium).

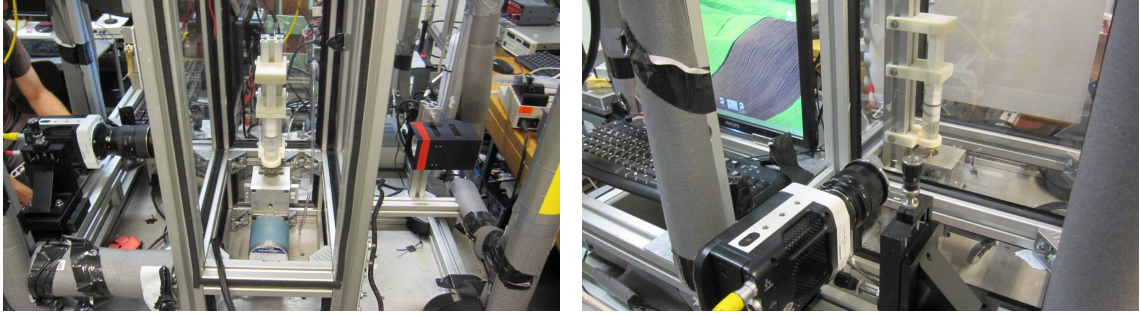


Figure 5.7: Experimental rack for parabolic flights

A home-made foaming device shown in Figure 5.8 consists of a piston perforated by several holes moving back and forth at frequency of 5 Hz in a syringe containing the foaming liquid (dimensions: height = 5 cm and diameter = 1.7 cm). The motion of the mesh is driven by a stepper motor (SLOSYN MO92) fixed onto the railings of the support chassis. Mechanical agitation caused by this movement breaks the gas into bubbles to create a foam. This technique gives bubbles with a mean radius about of $100 \mu m$. The syringe is filled with different amounts of liquid in order to vary the foam liquid fraction between 10 and 70 vol %. We used a surfactant solution of 4 g/l sodium dodecylsulfate that foams very well. Commercial antifoam (Silcolapse RG22, a gift from Bluestar Silicone) was used (0.7 wt % of oil in the solution). A high-speed camera (Phantom Miro 310, at 200 frames/s) is used to follow the foam generation and evolution.

Two syringes are tested simultaneously in each experimental run to get more statistics. The syringes are embedded in plastic structures, printed out to fit snugly around them. The syringes are easily changed between two series of parabolas as they are fixed in place with magnets. Both syringes and the motor are placed in a glove box to ensure that no electronic systems can come into contact with any liquids. The motor and camera are controlled using a computer (Labview). In case of a software crash they can also be started manually. In each experimental run the



Figure 5.8: Two syringes with moving pistons inside.

motor and the camera are launched simultaneously at the beginning of microgravity phase (see Figure 5.6). Generation lasts for first 10 seconds and then we follow the foam stability during the 12 seconds of 0G and few seconds of 2G phase.

After the parabolic flight campaign all the obtained videos were treated using ImageJ to get an estimation of the relative foam fraction F (ratio between a volume of the foam and a volume of the cell) as a function of time. Photographs of one of the foams (10 vol % liquid with antifoams) in microgravity are shown in Figure 5.9 for different times after the beginning of the experiment.

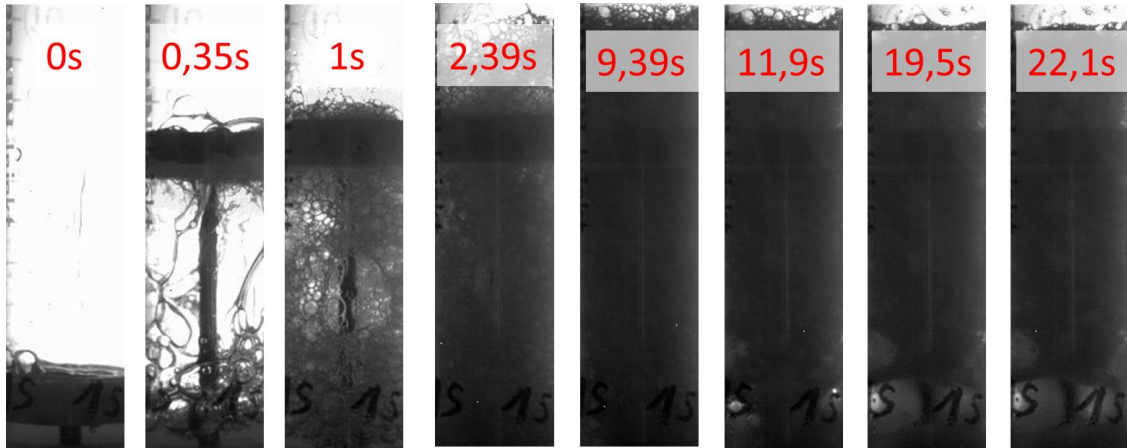


Figure 5.9: Photographs of foam (10 % liquid fraction) at different times after the beginning of the experiment.

5.6 Sedimentation in capillaries

To study particle sedimentation in capillaries very monodisperse polystyrene particles with diameters of 10, 20 and 40 μm are dispersed in a 4 g/L water solution of SDS. Addition of anionic surfactant charges the particles negatively preventing them from aggregation or adsorption on capillary walls. We can reasonably assume that electrostatic interactions are active only at very short distances and they do not alter particle fluid parameters. Glass capillaries having different inner diameters from 0.14 mm to 1.4 mm were purchased from the Drummond Scientific Company.

The capillaries are mounted on a plastic support printed to fit snugly around them (see Figure 5.10). To prevent evaporation the capillaries are closed from both sides. The verticality of capillaries is thoroughly checked before each experiment. The support is connected with a motor which can rapidly turn the capillaries upside down. Sequences of photographs are obtained in transmission with a CCD camera. In each experimental run up to 5 capillaries can be studied simultaneously.

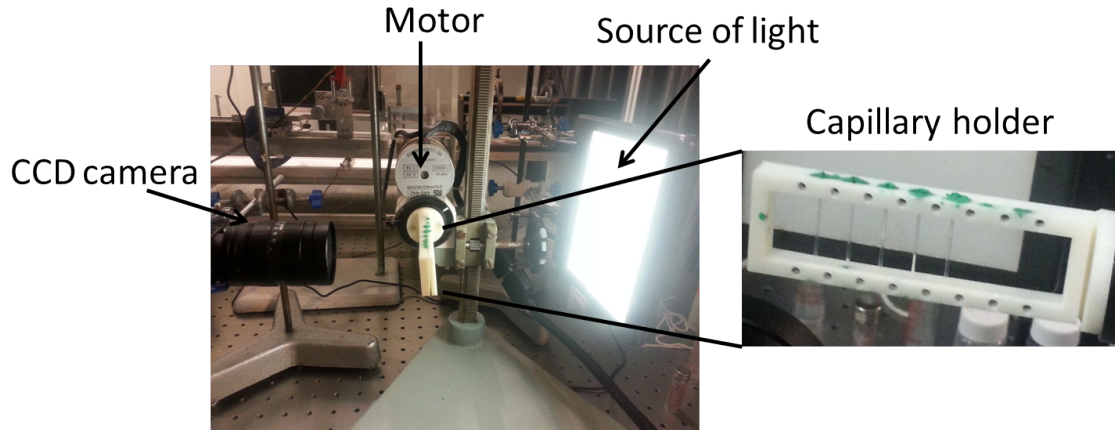


Figure 5.10: Experimental set-up for sedimentation experiments

Two configurations of initial particle distributions are studied in this work, namely homogenous and plug configurations.

In the "classic" homogeneous approach the video is recorded straight after the capillary is filled by capillary rising. The theoretical analysis of this configuration is described in Chapter 3, where it is assumed that the particles are distributed uniformly. Unfortunately, it is awkward to mix the particles inside the capillary, so we cannot be firmly confident of the homogeneity of the initial state.

Alternatively we let the particles to sediment and then turn the capillary by 180° . In this case we start from a plug configuration, where all particles are collected at the top of the sample. The advantage of the plug configuration is a better control of the initial conditions of the experiment, inhomogeneities in the initial filling of the capillary have no impact on the experimental results.

To treat the recorded images an ImageJ software is used. This software allows us to trace a segment of the video with time and make a reslice which shows the evolution of intensity profile inside a capillary. Examples of such reslices are shown in Figure 5.11 for homogeneous and plug configurations.

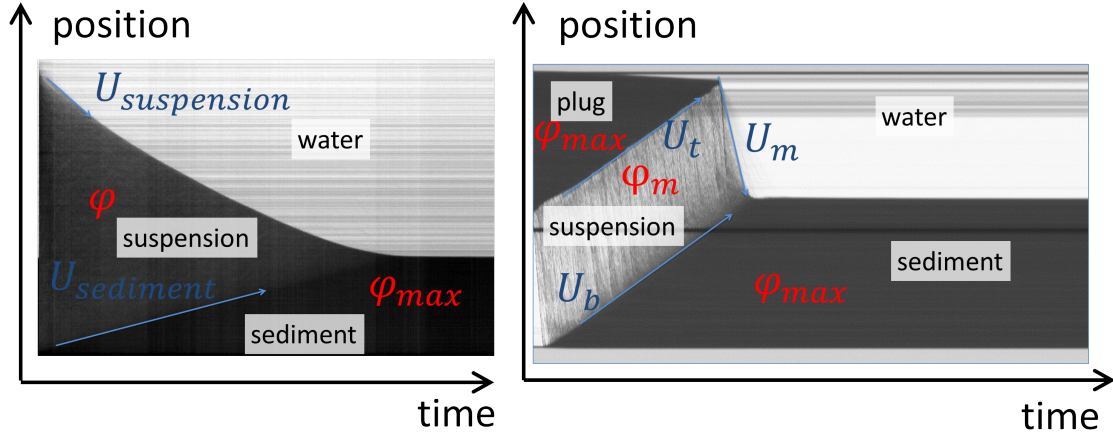


Figure 5.11: Reslices of the experimental image sequences for homogeneous (on the left) and plug (on the right) initial configurations. Different phases and fronts are shown.

In the homogeneous configuration two fronts are clearly observed: one between the suspension and clear fluid at the top and one between the suspension and immobile sediment at the bottom. As we have discussed in Chapter 3, the velocity of the former $U_{\text{suspension}}$ is equal to the average sedimentation rate of particles $\langle U_s \rangle$, while the velocity of the latter U_{sediment} can be related with $\langle U_s \rangle$ by Equation 3.26.

In the plug configuration all particles are initially compactified at the top of the sample. Due to the Rayleigh-Taylor instability the particles leave the plug with a maximum particle fraction φ_{max} and start to sediment forming a suspension region in the middle with an average fraction of φ_m . The front between the two regions moves with velocity U_t . The particles arrive at the bottom of the capillary and form a front between the suspension and a sediment phase rising with velocity U_b . Surprisingly, the experiment tells us that the system rapidly reaches a stationary regime, where U_t and U_b do not change with time and $U_t \approx U_b$. Taking into account that the volume occupied by the suspension is constant, we conclude that φ_m does not change with time in the steady-state.

As soon as the last particles leave the plug region a front between clear fluid and suspension forms. At this point the system is in the homogeneous configuration. The velocity of the descending front U_m therefore corresponds to an average sedimentation velocity $\langle U_s \rangle$. The advantage of this method of sedimentation velocity measurement is that the system has enough time to homogenise the sedimenting region.

By analysing reslices such as shown in Figure 5.11 on the right, the velocities U_t , U_b and U_m can be directly measured. The particle fraction of suspension φ_m can be calculated from the matter balance as

$$\varphi_m = \varphi_{\text{max}} \frac{U_b}{U_b + U_m}. \quad (5.5)$$

In wide capillaries, where the particle diameter d is much smaller than the capillary diameter D , we can assume that the particles are organised in a random close

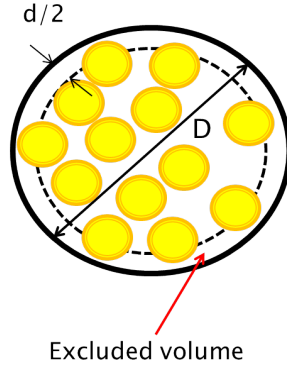


Figure 5.12: Excluded volume in the capillary.

packing structure and $\varphi_{\max} \approx 0.64$. For smaller capillaries the excluded volume effect should be taken into account (see Figure 5.12). Close to the capillary walls there exists a layer of fluid with thickness $d/2$ which is inaccessible for the centres of particles. This leads to the following expression for the maximum packing fraction in the capillary

$$\varphi_{\max} = 0.64 \cdot (1 - d/D)^2. \quad (5.6)$$

The experimentally measured maximum packing fraction for different confinement degrees is shown in Figure 5.13. One can see that the predication of Equation 5.6 shown by red line gives a reasonable estimation of φ_{\max} .

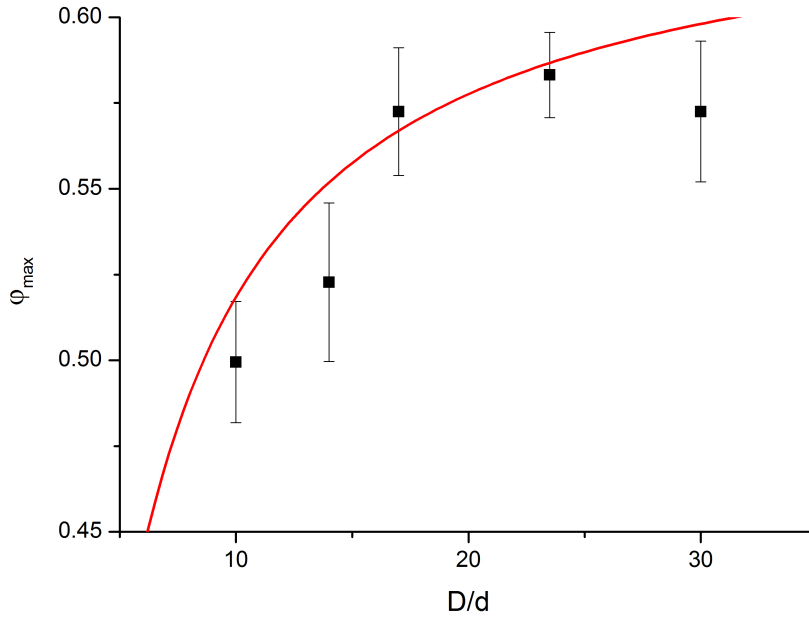


Figure 5.13: Maximum packing fraction φ_{\max} as a function of the degree of confinement D/d . The red line shows the prediction of Equation 5.6.

Using Equations 5.5 and 5.6 the content of particles in different regions in the plug configuration can be calculated from the experimental data.

The plug configuration is also used to study sedimentation in inclined capillaries. In this case the sedimenting region between the plug and the sediment separates due to the Boycott effect into two phases: a clear fluid close to the top wall and a suspension near the bottom wall (see Figure 5.14).

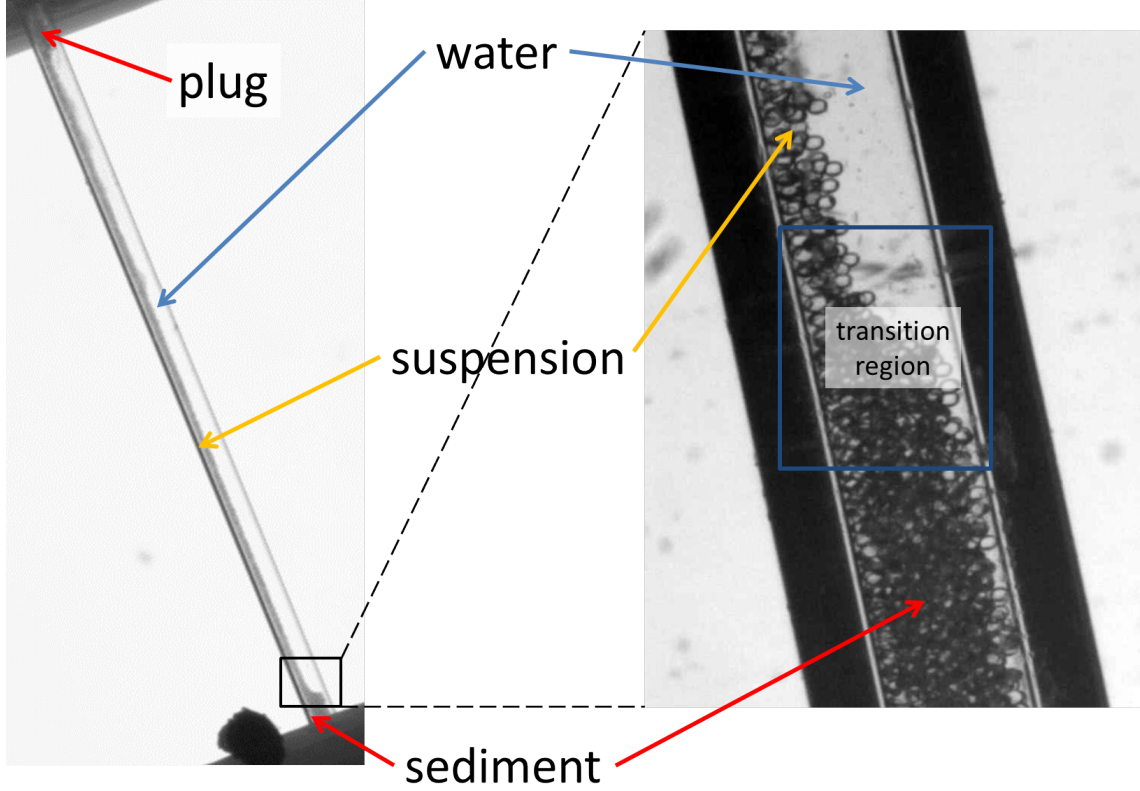


Figure 5.14: An inclined capillary corresponding to the initial plug configuration (on the left) and a zoomed region close to the sediment (on the right).

To properly treat the images in the described geometry, it is important to take a reslice inside the suspension region. It turns out that the reslice of inclined capillary looks exactly the same as the reslice in the vertical plug configuration shown in Figure 5.11. By analogy with vertical capillaries, we can measure front velocities U_t and U_b and average sedimentation velocity U_m . In the stationary regime the velocities do not evolve in time and we again find $U_t \approx U_b$. Using Equation 5.5 one can define an average particle fraction φ_m . However, in the inclined capillaries, φ_m does not represent the local particle concentration in the suspension, it only gives the mean content of particles in the sedimenting region consisting of suspension and water phases.

We should note that in the inclined capillaries there exist two transition regions between the suspension and the concentrated phases (plug and sediment). One of them can be observed in zoomed image in Figure 5.14. In these regions particle fraction rapidly changes along the axe parallel to the capillary from φ_{\max} to the par-

ticle concentration in the suspension. However, in our experiments these transition regions are much smaller than both the sedimenting region and the concentrated phases. So we usually neglect the presence of transition regions and assume that the suspension and the concentrated phases are separated by sharp fronts.

Part III

Experimental results and discussion

Chapter 6

Kinetics of surfactant desorption at air-water interface

6.1 Introduction

Surfactant adsorption/desorption kinetics are of great importance for the foam generation and stability. The creation of foam requires the formation of large amounts of new interface, which should be stabilized by surfactants. The bubble formation time-scale can be milliseconds, so the ability of surfactants to adsorb rapidly is critical for effective foam generation [69, 70].

Adsorption/desorption kinetics can also play a role in the generation of foamed emulsions. If the surfactant concentration is not very high, adsorption on emulsion droplets can significantly decrease the concentration of free surfactant molecules in the aqueous phase [71]. In surfactant-poor systems an emulsion can foam efficiently only if the surfactant transport from oil droplets to bubbles is sufficiently fast. The last strongly depends on the presence of adsorption and desorption barriers.

In Section 1.8 we have seen that the evolution of the surface concentration can be predicted by various adsorption models. However, experimentally the variation of the surface tension with time $\gamma(t)$ is usually measured. The kinetic models need therefore a surface equation of state linking γ and Γ such as the Szyszkowski 1.42 or the Frumkin 1.45 equations. The use of theoretical equations of state requires several assumptions which are not rigorously valid. For example, the Frumkin isotherm assumes that the pairwise interaction energy does not depend on the surface coverage, which is, of course, a very rough approximation. More accurate equations of state can be used, but they usually involve a large number of adjustable parameters, which are difficult to estimate.

A simple way to experimentally measure the equation of state using dynamic surface tension data at single concentration was suggested by Pan et al. [72]. The surface equation of state is experimentally determined by measuring the surface tension response during a fast bubble compression or expansion. If the relative rate of area dilatation is sufficiently high, there is no exchange of surfactant between the surface layer and the sub-phase during the experiment and the $\gamma(\Gamma)$ dependence can be easily accessed. Using the experimentally determined equation of state the dynamic surface tension during the adsorption/desorption process can be directly converted

to the kinetic dependencies of surface concentration without any additional theoretical assumptions. Using this technique the behaviour of a non-ionic surfactant ($C_{12}E_6$) and an ionic surfactant with an excess of inorganic salt (CTAB+NaBr) has been investigated [73]. The adsorption kinetics of these solutions has been shown to be diffusion-controlled, however the desorption kinetics has not been systematically studied yet [74]. In this chapter we will continue this research and focus mainly on the desorption kinetics of a CTAB+NaBr mixture. In the presence of excess salt the equilibration of the double electric layer is always very fast and the system can be treated as a non-ionic one. We decided to concentrate our attention on the ionic system as a high purity of ionic surfactant can be achieved simply by multiple recrystallisations, which is extremely important in the study of the dynamics of surfactant desorption.

6.2 Experimental procedure

We have chosen CTAB at a concentration of 10^{-5} M with 0.1 M NaBr to screen electrostatic interactions. This surfactant concentration is lower than the CMC ($3 \cdot 10^{-5}$ M) at the given salt concentration [73], so no micelles are present in the solution.

The dynamic surface tension is measured by a bubble shape analysis method using a commercial tensiometer “Tracker” (Teclis, France). All experiments are performed at 25° C. The details of profile analysis tensiometry and the experimental set-up are found in Section 5.3.

To experimentally measure the equation of state the following experiment is performed. A bubble is created and after some ageing time it is rapidly compressed or expanded. Figure 6.1 shows an example of surface tension and surface area as a function of time during a fast compression. If the deformation rate is sufficiently high, the total number of surfactant molecules on the bubble interface does not change $\Gamma A = \Gamma_{ref} A_{ref}$, where Γ_{ref} and A_{ref} are the surface concentration and surface area of a reference state. The reference value of $\Gamma_{ref} = 3.5 \cdot 10^{-6}$ mol/m² at $\gamma_{ref} = 36$ mN/m has been taken from [73]. Using this reference point the $\gamma(A)$ dependence can be converted to the experimental surface equation of state $\gamma(\Gamma)$.

Taylor and al. have shown that if the surface dilatation rate is not high enough, the adsorption during bubble compression/expansion can significantly influence the obtained results and specific corrections are required [75]. To verify the assumption of negligible exchange between the interface and the sub-phase in our experiments, different dilatation rates are tested. Some results are shown in Figure 6.2, the data for different compression rates perfectly superimpose. In the previous work, it has been shown that for smaller compression rates the results start to deviate indeed indicating the influence of adsorption/desorption during the bubble dilatation [73]. It has been also shown that the described method of the $\gamma(\Gamma)$ measurement gives results comparable with ones obtained by classical analysis of the equilibrium isotherm $\gamma(c)$ using Gibbs equation. Summing up, we can conclude that, for compression rates higher 1.5 μ L/s, our experimental technique gives a reliable and accurate method to measure the surface equation of state.

To measure surfactant desorption kinetics, a bubble is created, left to reach an

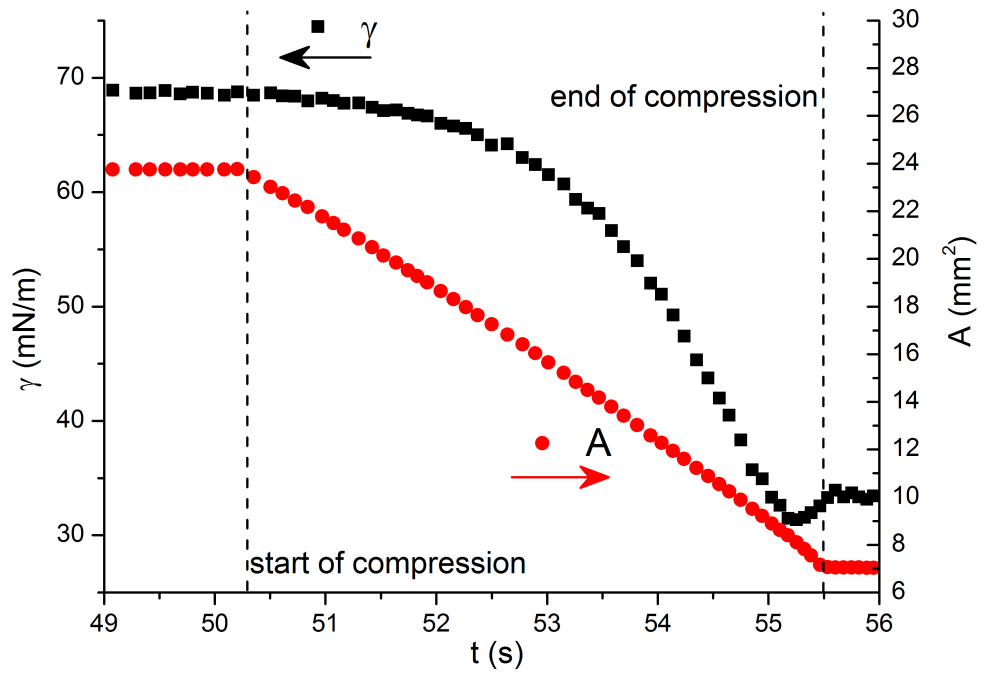


Figure 6.1: Variations of surface tension (black squares) and bubble surface area (red circles) with time during the compression of the bubble.

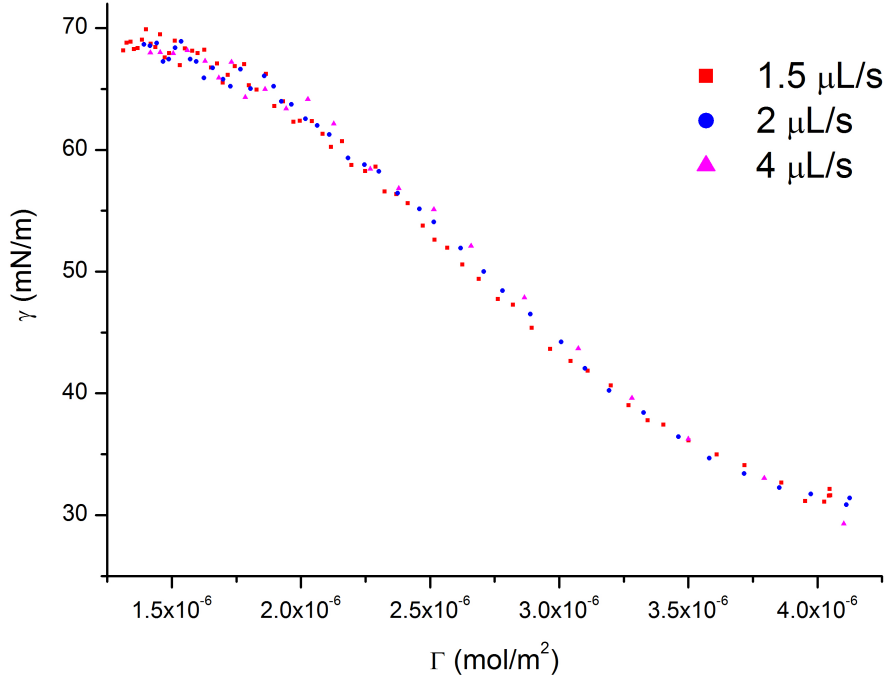


Figure 6.2: Surface tension as a function of the calculated surface concentration at various compression rates.

equilibrium and is compressed quickly so as to increase the surface concentration rapidly above its equilibrium value. The bubble compression induces a lot of convection in the bulk, so we assume that after compression the bulk concentration is constant everywhere and equal to the equilibrium value. As soon as the compression is stopped, the surface tension γ as a function of time t is recorded as it increases during the re-equilibration of the system. Using the measured equation of state $\gamma(\Gamma)$, the dynamic surface tension $\gamma(t)$ is converted to the kinetic surface concentration dependence $\Gamma(t)$. For each degree of compression the experiment is repeated at least 3 times and the average curve is calculated. Different degrees of compression $\Delta A/A$ are tested from 0.03 to 0.2.

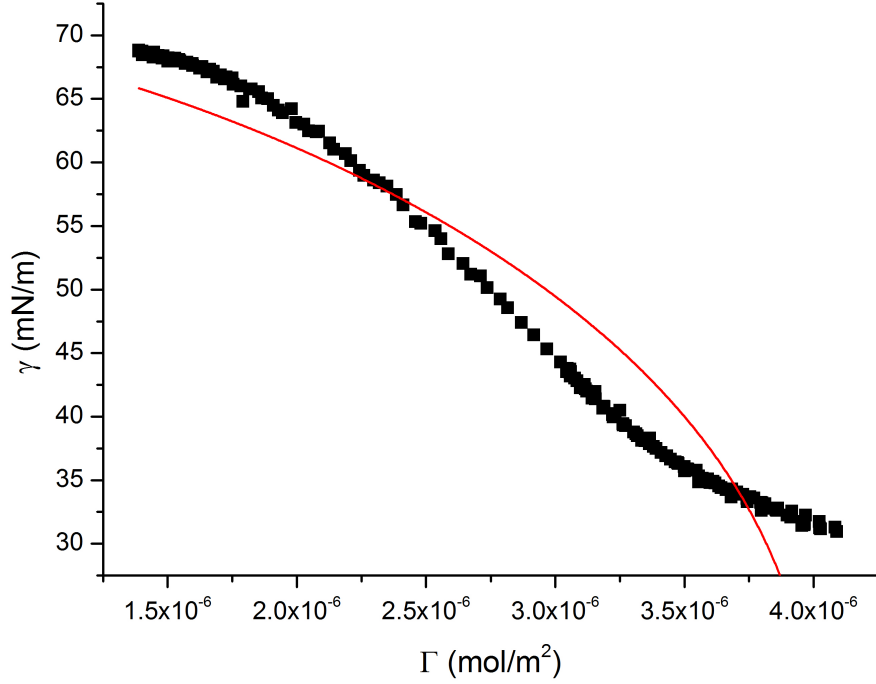


Figure 6.3: Experimental equation of state $\gamma(\Gamma)$. The red line shows the best fit by Frumkin equation with $A_F = 3.37$.

6.3 Results and discussion

6.3.1 Equation of state

The experimental equation of state is shown in Figure 6.3. A minimum value of surface tension obtained in our compression experiments is about 31 mN/m and further compression does not change it. Therefore this surface tension can be attributed to the maximum packing of molecules at the interface. Then from the experimental data Γ_∞ can be estimated as $4.1 \cdot 10^{-6} \text{ mol/m}^2$. The simplest theoretical model, taking into account inter-molecule interactions, is described by the Frumkin equation 1.45. In Figure 6.3 one can see that the Frumkin equation poorly fits the experimental data. The Langmuir model, being a particular case of the former with $A_F = 0$, can not fit the data either. This confirms that the use of these theoretical equations of state to model the dynamic surface tension of the system can give unreliable sorption barriers.

The main reason, why the Frumkin model fails to fit the data, is that the interactions between molecules in the surface layer are not constant as assumed by Frumkin but rather depend on the surface coverage in a non-trivial way. To better describe the interactions different expressions have been proposed for the $A_F(\Gamma)$ dependence, for example a power-law dependence in the empirical generalised Frumkin equation [76, 77]. However, in this chapter instead of assuming a certain type of $A_F(\Gamma)$

dependence, we will see how to extract it from the experimental data. We can reasonably assume that the Frumkin equation state is still valid locally, in the narrow range of surface concentrations, where A_F can be considered constant. In the vicinity of a certain surface concentration $\tilde{\Gamma}$ the "local" Frumkin equation is

$$\gamma(\Gamma) = \overbrace{\left[\gamma(\tilde{\Gamma}) - RT\Gamma_\infty \left(\ln \left(1 - \frac{\tilde{\Gamma}}{\Gamma_\infty} \right) - \frac{A_F(\tilde{\Gamma})}{2} \left(\frac{\tilde{\Gamma}}{\Gamma_\infty} \right)^2 \right) \right]}^{const(\tilde{\Gamma})} + RT\Gamma_\infty \left(\ln \left(1 - \frac{\Gamma}{\Gamma_\infty} \right) - \frac{A_F(\tilde{\Gamma})}{2} \left(\frac{\Gamma}{\Gamma_\infty} \right)^2 \right). \quad (6.1)$$

By dividing the experimental equation of state into small regions and fitting each part independently by Equation 6.1, an $A_F(\Gamma)$ dependence can be experimentally measured (see Figure 6.4). The top axes of Figure 6.4 also show the corresponding average distance d^* between surfactant molecules. To estimate d^* we assume as a first approximation that surfactant molecules are arranged in a hexagonal packing, then the average distance is $d^* = \sqrt{2/(\sqrt{3}\Gamma N_A)}$, where N_A is the Avogadro constant.

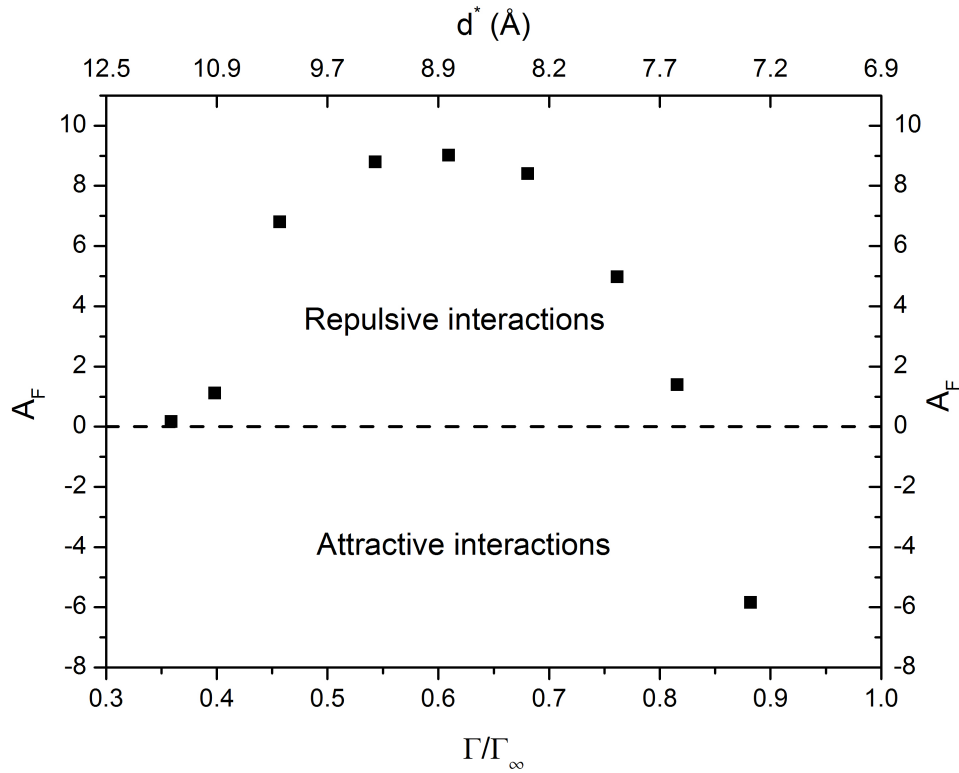


Figure 6.4: Variation of the interaction parameter A_F with surface coverage Γ/Γ_∞ . The top axes show the average distance between surfactant molecules d^* .

Let us recall that positive values of A_F indicate a repulsion in the surface layer, and negative values correspond to an attraction, while at $A_F = 0$ there are no

interactions. One can see that A_F indeed varies strongly with Γ . At small surface coverages ($\Gamma/\Gamma_\infty < 0.3$) and big inter-molecule distances ($d^* < 12 \text{ \AA}$), the surfactant molecules do not interact in the surface layer. As the surface concentration increases a repulsive interaction arises. At $\Gamma/\Gamma_\infty \approx 0.6$ and $d^* \approx 9 \text{ \AA}$ the repulsion reaches its maximum. Any further increase of surface coverage leads to a decrease of repulsion and at a certain point the molecules start to attract each other.

A similar behaviour has been reported in [78, 79]. The distance at which the repulsion starts to be important ($\approx 12 \text{ \AA}$) is comparable with the length of the hydrophobic tail. Steric forces between tails lying on the surface can induce the repulsion. Also at the used salt concentration the Debye length is around 10 \AA , so the electrostatic repulsion between charged surfactant headgroups can be important. As the molecules come closer the tails self-organise perpendicular to the interface inducing a Van der Waals attraction between them.

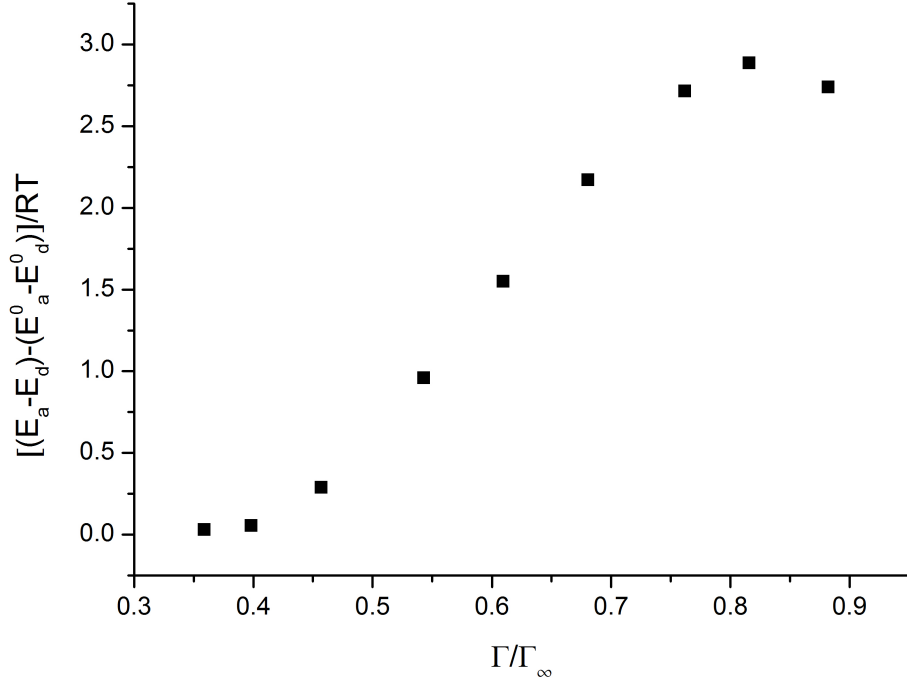


Figure 6.5: Variation of the difference between sorption energies $(E_a - E_d) - (E_a^0 - E_d^0)$ with surface coverage Γ/Γ_∞ .

We can take one step forward in analysing the $A_F(\Gamma)$ dependence. According to Equation 1.53 we can express the interaction parameter as

$$A_F = \frac{\Gamma_\infty}{RT} \frac{\partial(E_a - E_d)}{\partial \Gamma}. \quad (6.2)$$

At a bare interface ($\Gamma \rightarrow 0$) the adsorption and desorption barriers are E_a^0 and E_d^0 , respectively. By integrating Expression 6.2, an evolution of the adsorption and

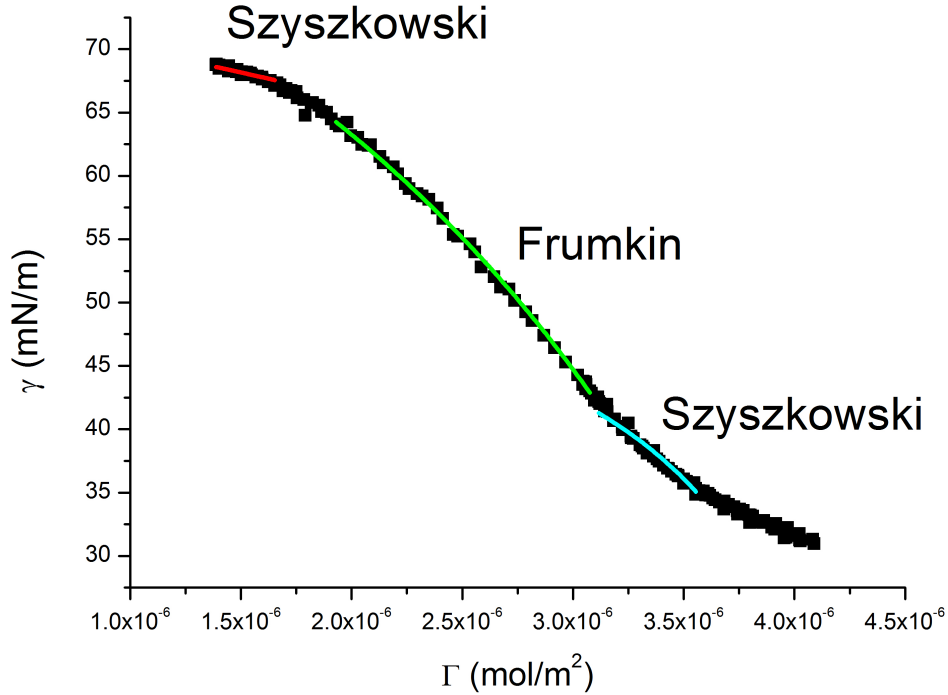


Figure 6.6: Experimental equation of state $\gamma(\Gamma)$. Different regions are fitted by the Szyszkowski (red and cyan lines) and a "local" Frumkin equation 6.1 with $A_F = 7.8$ (green line).

desorption activation energy difference $(E_a - E_d) - (E_a^0 - E_d^0)$ as a function of surface concentration can be obtained. In Figure 6.5 one can see the results of the numerical integration performed by the trapezoid rule for the data presented in Figure 6.4.

The experimentally measured $E_a - E_d$ vs Γ/Γ_∞ dependence can be divided into three regions. For $\Gamma/\Gamma_\infty < 0.4$ the difference of sorption energies is almost constant. The surface concentration is too low to influence both adsorption and desorption energies, in this regime the Szyszkowski equation 1.42 should work for $\gamma(\Gamma)$ dependence. For $0.45 < \Gamma/\Gamma_\infty < 0.75$, $E_a - E_d$ linearly increases with the surface coverage. The raise is probably mainly related to the increase of the adsorption barrier caused by electrostatic and steric forces. The linear increase of the sorption energy difference is the main assumption of the Frumkin model, so we expect the experimental equation of state to be fitted by Equation 6.4 with a unique value of A_F in this region. For higher surface concentrations ($\Gamma/\Gamma_\infty > 0.75$), $E_a - E_d$ reaches its maximum and it is again approximately constant. We can expect to fit the $\gamma(\Gamma)$ dependence in this region by the "local" Szyszkowski equation, so Equation 6.4 with $A_F = 0$.

The suggested fits of the experimental equation of state are shown in Figure 6.6. One can see that for small surface concentrations the data are indeed described by the Langmuir model. In the intermediate range the "local" Frumkin equation

perfectly fits the $\gamma(\Gamma)$ dependence. Close to the maximum surface packing fraction the Langmuir model can give rather approximate description of the experimental data, which is probably related with a fast change of inter-molecule interactions with surface coverage in this region.

6.3.2 Desorption kinetics

Using the experimental equation of state, the relaxation of surface concentration $\Gamma(t)$ after a fast bubble compression is measured (see Figure 6.7). In this study only relatively small degrees of compression of the interface are considered, for most of the present experimental points the surface coverage Γ/Γ_∞ lies in the range from 0.75 to 0.85. In this narrow range the repulsive and attractive forces compensate each other and the interaction is close to zero (see Figure 6.4). From Figure 6.5, one can see that in the studied surface concentration range $E_a - E_d$ reaches a plateau, allowing us to assume that adsorption and desorption barriers are almost constant.

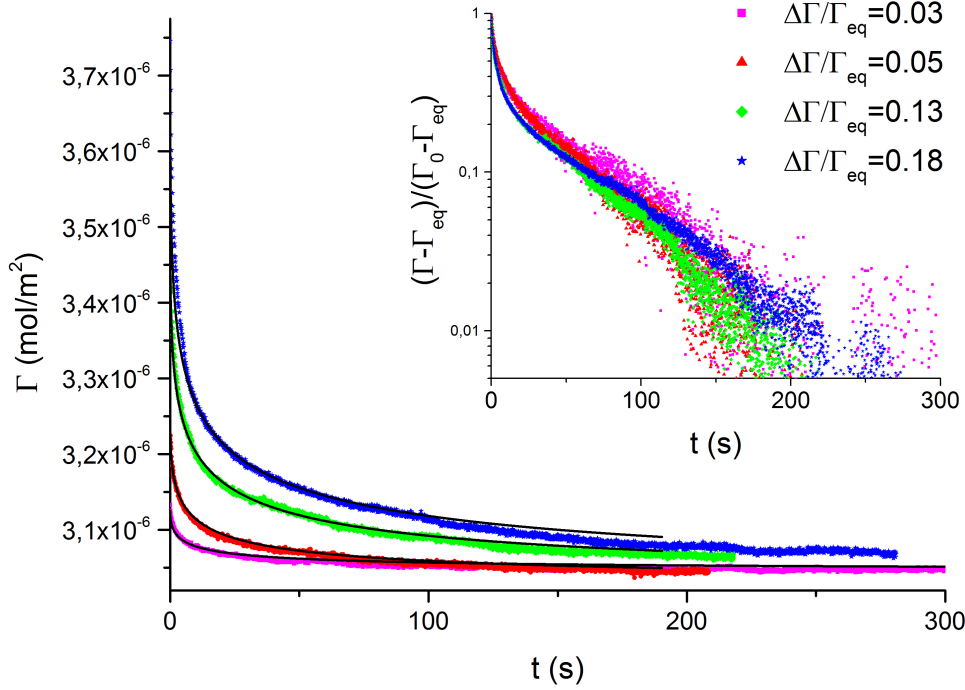


Figure 6.7: Time variation of the surface concentration after a rapid compression for different degrees of compression. The black lines show the best fits by diffusion-limited model with $D \approx 6 \cdot 10^{-10} \text{ m}^2/\text{s}$. Inset: Variations of $(\Gamma(t) - \Gamma_{eq})/(\Gamma_0 - \Gamma_{eq})$ with time for the same experimental data in log-linear axis.

First of all we will see if the desorption curves can be fitted by a kinetically controlled model. In the kinetically-limited case, the diffusion from the bulk to the interface is fast, but there is no equilibrium between the interface and the sub-phase.

Recall that in the barrier-limited case, if the activation energy of sorption is constant, the variation of the surface concentration can be represented in the following form (see Equation 1.51)

$$\frac{\Gamma(t) - \Gamma_{eq}}{\Gamma_0 - \Gamma_{eq}} = e^{-t/t_{ads}}. \quad (6.3)$$

The inset of Figure 6.7 shows the variations of $(\Gamma(t) - \Gamma_{eq})/(\Gamma_0 - \Gamma_{eq})$ with time in log-linear axis. Equation 6.3 implies that in these axis all data lies on a straight line, which is not a case in our experiments. It means that the barrier-limited model is not valid for our system and surfactant diffusion in the bulk should be taken into account.

We can emphasize the importance of the diffusion step by estimating the characteristic diffusion time from Equation 1.48. Taking the diffusion coefficient as $10^{-10} - 10^{-9} \text{ m}^2/\text{s}$, t_{diff} has an order of magnitude of $10^2 - 10^3 \text{ s}$. This diffusion time is comparable with the experimental desorption time, meaning that the diffusion step is important for a proper description of desorption kinetic.

To check the applicability of the diffusion-limited model to our experimental data Matlab simulations are performed. The model is similar to the Ward and Tordai equation describing the diffusion away from the surface. The sub-phase is assumed to be in equilibrium with the surface at all times. The experimentally measured equation of state allows us to avoid making any assumptions about the $\gamma(\Gamma)$ dependence. However, a theoretical adsorption isotherm has to be used to link the surface concentration Γ and the sub-phase concentration c_s . As we have discussed above, in the studied range of surface concentrations, the adsorption and desorption barriers are pretty constant with Γ . It allows us to use the Langmuir adsorption isotherm to get a first approximation of $\Gamma(c_s)$ dependence. The equilibrium adsorption constant can be estimated from Equation 1.43 as

$$K = \frac{\Gamma_{eq}}{c_{eq}(\Gamma_{\infty} - \Gamma_{eq})} \quad (6.4)$$

At each step of simulation a profile of surfactant concentration close to interface is established by Fick's law. At the end of simulation the time variation of the surface concentration is obtained.

The only adjustable parameter in the simulations is the diffusion coefficient. The best fits of the experimental data for different degrees of compression are shown by the solid lines in Figure 6.7. It turns out that all our desorption curves can be described by a diffusion-limited model with $D \approx 6 \cdot 10^{-10} \text{ m}^2/\text{s}$.

6.4 Conclusion

In this chapter, the surface equation of state for CTAB with 0.1 M of NaBr has been measured using a fast bubble compression/expansion method. By fitting the experimental results, the interactions between molecules in the surface layer have been studied.

Using the experimentally determined surface equation of state, the desorption of ionic surfactant with excess of salt has been studied. The measured desorption curves

are reasonably described by a diffusion-limited model. The diffusion coefficient has been calculated by comparing the Matlab simulations and experimental results. The obtained value of $D \approx 6 \cdot 10^{-10} \text{ m}^2/\text{s}$ is comparable with one used earlier to describe adsorption in the same surfactant system [73].

Chapter 7

Generation of rising foams

7.1 Introduction

The physical properties of foams are largely controlled by the bubble size R and the liquid fraction ε , which makes them such important parameters. However, the control of these two parameters during the foam generation remains mainly empirical [69]. In general, with a given foam generation process, the bubble size and the liquid fraction can only be varied in a rather narrow range. Moreover there is often a correlation between the two parameters, and generation methods where they can be varied independently are scarce. Examples are shown in figure 7.1, where the bubble size and the liquid fraction are shown for foams prepared by blowing gas thorough a porous media and by the turbulent mixing of liquid and gas jets. A strong correlation between bubble size and liquid fraction is observed, which has also been shown in foams generated by microfluidic techniques [80]. Finally, the different methods allow for the exploration of a range of bubble radii and liquid fractions, but rarely independently. In general either the liquid fraction or the bubble size is controlled and sets the other in combination with the flow conditions. It is only through a fine understanding of each of the processes used that control over the bubble radius and the liquid fraction, and thus, of foam properties can be achieved.

In the following, I focus on a very common technique used to generate foams: blowing gas through a porous media. The process can be divided into two separate steps. The first one is the formation and rising of the bubbles in the liquid before they agglomerate at the liquid/air interface. The second is the simultaneous rising and drying of the foam. The bubble radius is mainly controlled during the first stage. Theoretical descriptions of this process can be found in the literature for a number of different techniques, however some aspects still remain unclear [69, 81]. In this work we focus on the second stage, in which the liquid fraction profile in the foam is fixed. This is set by a balance between the foam rising in the column due to the buoyancy force and the gravity driven drainage of the liquid leading to foam drying. After a certain time, a steady-state regime can be reached, characterized by a stationary liquid fraction profile.

Although a thorough understanding of the second step is essential for a description of the final foam, there are only few theoretical publications [82–86] in this field and experimental data concerning this problem are scarce [87, 88]. Among these

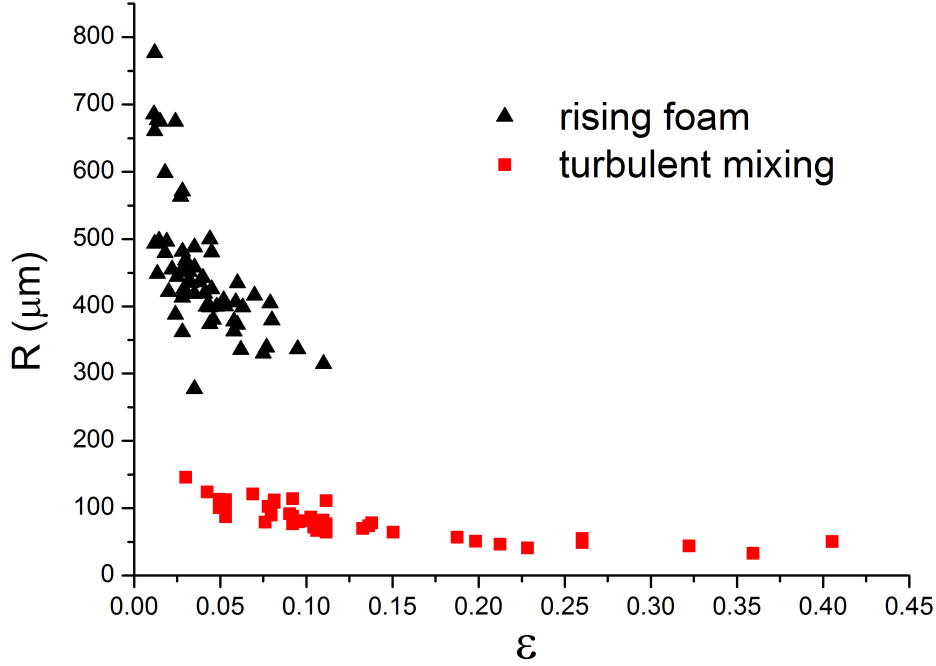


Figure 7.1: The relation between the radius and the liquid fraction for two different generation methods.

works is the model developed by Stevenson to establish the liquid fraction profile as a function of the gas flow rate imposed at the bottom [83, 84]. The basis of this model is that the liquid fraction profile is mainly fixed by the drainage of the foam during its generation.

It is well known that drainage in foams is quite different depending on the surface mobility (see Chapter 3 for more details). In this chapter, our goal is to explore the impact of surface rigidity on foam generation. I recall Stevenson's model and build on it to explore more quantitatively how the change in boundary conditions influences on the liquid flow in the rising foam.

The experiments are done with solutions of surfactants, that are known to lead to rigid or fluid interfaces in drainage experiments [57, 60]. The bubble radius and the liquid fraction profile of the foam are measured for each foaming solution. This work provides a systematic comparison between the liquid fraction profile obtained in the model and in the experiments. Moreover, we see that every surfactant solution used in this work leads to a liquid fraction profile well described by the equations obtained in the mobile limit. This is because the forced drainage experiments are performed on dry foams whereas in the foamability experiments one cannot get around wet ones.

7.2 Experimental procedure

A commercially available device Foamscan (Teclis, France) is used to generate foam and to measure the liquid fraction profile. The bubble sizes are measured by taking photos of foam samples squeezed between two plates. The detailed description of the experiment can be found in Chapter 5. The different foaming solutions used to generate foams are listed below, with the name by which they are referred to in the rest of the chapter:

- SDS at 12 g/L - SDS12
- SDS at 12 g/L with 0.3 g/l of dodecanol - SDS12-DOH3
- SDS at 12 g/L with 0.04 g/l of dodecanol and 0.1M of NaCl - SDS12-DOH4-NaCl
- TTAB at 3 g/L with 0.2 g/l of dodecanol - TTAB3-DOH2

To keep the liquid level constant the set-up is in contact with a big vessel containing the foaming solution. By varying the level of liquid the position of the interface between the foam and the solution can be moved relative to the electrodes. In this way different heights in the foam can be probed and a full liquid fraction profile can be measured.

A steady-state defined by a constant conductivity is reached before each measurement of the liquid fraction.

7.3 Theoretical background

Let us consider a foam which moves inside a tube with a cross-sectional area S (see figure 7.2). The axe z is oriented along the column in the direction of the foam flow. The bottom of the foam corresponds to $z = 0$. At each point the foam can be fully characterized by the liquid fraction $\varepsilon(z, t)$, the mean radius of the bubbles $R(z, t)$, and the flow rates of liquid $Q_l(z, t)$ and gas $Q_g(z, t)$. In this case the linear velocities of liquid $v_l(z, t)$ and gas $v_g(z, t)$ can be calculated

$$\vec{v}_l = \frac{\vec{Q}_l}{S\varepsilon}, \quad (7.1)$$

$$\vec{v}_g = \frac{\vec{Q}_g}{S(1 - \varepsilon)}. \quad (7.2)$$

The liquid and gas do not travel at the same speed and this difference is used to define the slip velocity

$$\vec{v}_s = \vec{v}_l - \vec{v}_g. \quad (7.3)$$

Considering our system in the reference of the moving bubbles it is clear that the slip velocity just corresponds to the velocity of liquid flow through the bubble

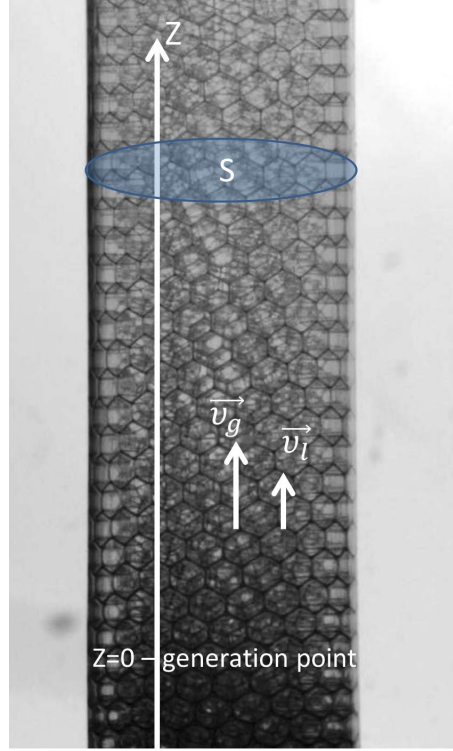


Figure 7.2: Foam rising in a tube

assembly. Thus the slip velocity can be described by Darcy's law 3.34. Combining Equations 7.3, 3.34 and 3.37, one gets

$$\vec{Q}_l = \frac{\varepsilon \vec{Q}_g}{(1 - \varepsilon)} + \frac{SR^2 k(\varepsilon)}{\mu} \left(\rho \vec{g} + \vec{\nabla} \Pi \right). \quad (7.4)$$

Now let us assume that our foam has reached a stationary regime in which the liquid fraction does not depend on time, i.e. $\partial \varepsilon / \partial t = 0$. We know from the experiments that such a regime exists. To avoid misunderstanding let us mention that ε is still a function of z . In the steady state, assuming that there is no evaporation in the system, the mass conservation gives us that the flow rates of gas and liquid are constant along the tube $\partial Q_g / \partial z = \partial Q_l / \partial z = 0$. It means that in the stationary regime the flow rates of gas and liquid at any point inside the foam are equal to the ones used to produce the bubbles. In the case of rising foam Q_g can be controlled, while Q_l is self-adjusted to satisfy Equation 7.4.

Applying the mass conservation condition $\partial Q_l / \partial z = 0$ to Equation 7.4 one can eliminate Q_l and get a differential equation which can be solved to get the liquid fraction profile $\varepsilon(z)$. But the corresponding equation is of second order and is quite complicated. An elegant way to simplify the calculations has been proposed by Stevenson [89]. Far away from the bottom the osmotic pressure gradient can be neglected and the liquid fraction ε^∞ is almost constant with height. Then Q_l is a function only of ε^∞ and the stationary state corresponds to the condition $\partial Q_l / \partial \varepsilon^\infty = 0$ [89]. Assuming a constant bubble radius, this condition can be written as

$$\frac{\mu Q_g/S}{(1 - \varepsilon^\infty)^2 R^2 \rho g} = \frac{\partial k(\varepsilon^\infty)}{\partial \varepsilon^\infty}. \quad (7.5)$$

This equation can be solved numerically to get ε^∞ and calculate Q_l from Equation 7.4. The obtained value of Q_l can be then used to calculate the whole liquid fraction profile from Equation 7.4. This differential equation is of first order. Using the semi-empirical Expressions 3.56 and 3.57 for permeability and empirical Equation 3.43 for osmotic pressure, Equation 7.4 can be solved numerically in the two limiting cases of mobile and rigid interfaces to get a liquid fraction profile $\varepsilon(z)$. To perform the integration we need an appropriate boundary condition. Assuming that at the bottom of the foam bubbles are not deformed, the boundary condition can be written as $\varepsilon(z = 0) = \varepsilon_{\max}$, with $\varepsilon_{\max} = 0.26$ for ordered foams [53] and $\varepsilon_{\max} = 0.36$ for disordered ones [54]. Polydispersity in the bubble size can stop the bubbles from crystallising leading to a disordered packing. Therefore we refer to $\varepsilon_{\max} = 0.26$ as monodisperse and $\varepsilon_{\max} = 0.36$ as polydisperse.

7.4 Results and discussion

To check the applicability of the developed theory, the liquid fraction was measured for different foaming solutions at different gas flow rates.

Experiments with a solution of SDS at 12 g/l are shown in Figure 7.3. The bubble size distribution, shown in the inset, is monomodal and sharply peaked. Using the mean Sauter radius $R_{32} = \langle R^3 \rangle / \langle R^2 \rangle$ as the characteristic bubble radius ($R_{32} = 523 \mu\text{m}$) liquid fraction profiles are calculated in the rigid (Equation 3.57) and in the mobile (Equation 3.56) limits. For each limit, profiles for monodisperse and polydisperse foams are calculated using the corresponding values for α and ε_{\max} in Equation 3.43. This results in 4 different theoretical curves. One can see that rigid and mobile limits predict significantly different liquid fractions especially far away from the bottom of the foam (Figure 7.3). Thus, it should not be a problem to discriminate between the mobile or the rigid limits from the experimental data. However for a given mobility the curves corresponding to ordered and polydisperse limits almost coincide. The ordering at the bottom of the foam thus results in such fine variations that they are not detected by our experiments. That is why in the following we will consider only the case of monodisperse ordered foams. Experimental data shown with black points agree well with the model of mobile interfaces. The obtained result is expected. It is well known, both from interfacial rheology and from drainage experiments that newly prepared SDS solutions have low surface shear viscosity (about 10^{-7}kg/s) and produce mobile interfaces in both forced and free drainage experiments [90].

One can ask about the error bars in the measurements. Electrical conductivity measurements provide us with an accurate estimation of the liquid fraction, the position of electrodes can also be measured from photographs with sufficiently high precision. The main source of errors in our experiments is the distribution of bubble sizes. Typically the bubble size distribution is monodisperse but it still has a certain standard deviation δ . To estimate the influence of this slight polydispersity on our predictions let us take the experimental data shown in Figure 7.3 and add

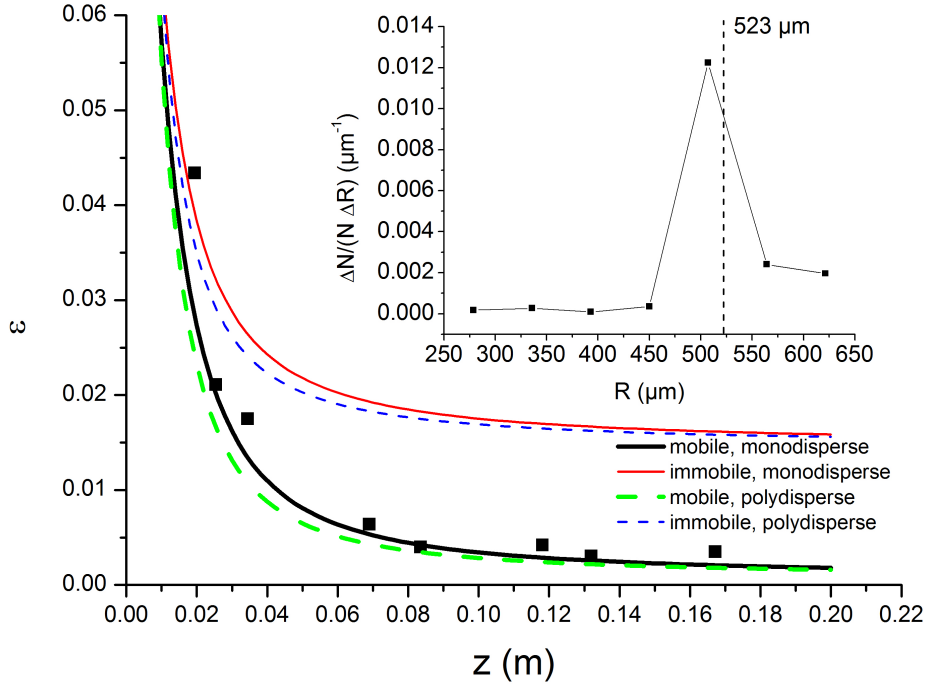


Figure 7.3: Liquid fraction profile for SDS12 foam produced with a 10 ml/min gas flow rate. Black points represent experimental data, the lines show calculated profiles in different limits with no adjustable parameters. Inset: Number weighted bubble size distribution.

theoretical liquid fraction profiles for three different bubble radii: R_{32} and $R_{32} \pm \delta$ (see Figure 7.4). One can see that the experimental data lie between two limits. So the dispersion of bubble sizes can indeed explain the scattering in the experimental points.

Increasing the flow rate to 30 ml/min the bubble size distribution is changed drastically as smaller holes in the frit become activated. The bubble size distribution weighted by number becomes bimodal as shown in the inset of Figure 7.5. In this case, it is not evident which mean value is the best to input in our calculations as a bubble size. Thus, three different ways to determine the mean size have been chosen: a mode size corresponding to small bubbles (303 μm), a mean Sauter radius R_{32} (457 μm) and a mode corresponding to big bubbles (558 μm). For each mean value liquid fraction profiles are calculated (see Figure 7.5). Only curves corresponding to the mobile limit are shown, as the rigid model predicts much higher liquid fractions than the ones measured experimentally. The best agreement with the experiments is obtained using the big bubble radius as input. It seems that the big bubbles control the foam permeability even if their number is very small. This is both because their total volume is actually non negligible and because the liquid tends to follow the path of lower permeability.

Summing up one can conclude that the model with mobile interfaces captures

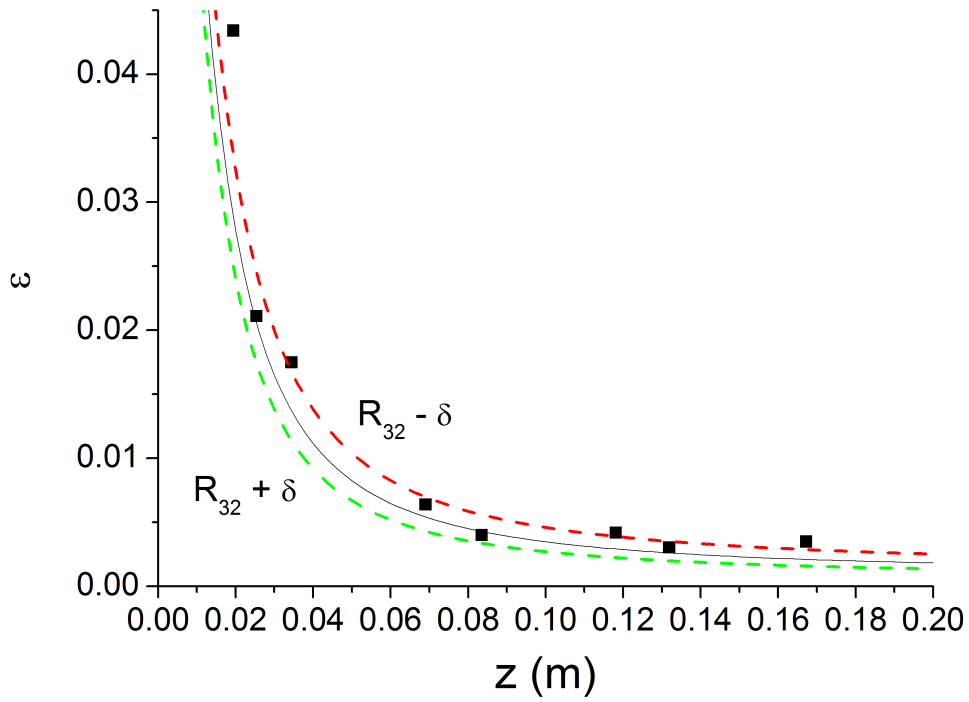


Figure 7.4: Liquid fraction profile for SDS12 foam produced at 10 ml/min gas flow rate. Black points represent experimental data, the lines show calculated profiles for different bubble sizes: $R_{32} = 523\mu m$ (black line), $R_{32} - \delta = 473\mu m$ (red dashed line), $R_{32} + \delta = 573\mu m$ (green dashed line)

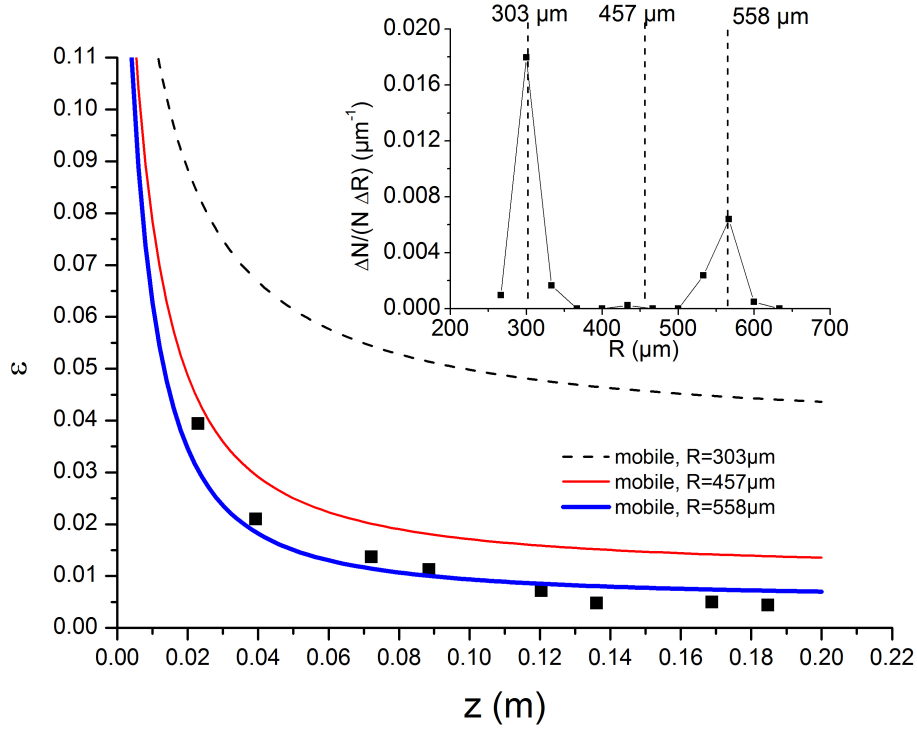


Figure 7.5: Liquid fraction profile for the SDS12 foam produced with a 30 ml/min gas flow rate. Black points represent experimental data, the lines show calculated profiles for different bubble sizes. Inset: Number weighted bubble size distribution.

the liquid fraction profile for foams stabilized by fresh solutions of SDS. We have also seen that the liquid fraction profile is not very sensitive to the polydispersity of bubbles making the model valid for both monodisperse and polydisperse foams. Moreover in the case of bidisperse foam with two distinct populations of bubble sizes, the largest bubble size has to be used in the model for it to agree with the experimental liquid fraction profile. Because our foam typically has very narrow bubble size distributions, I will focus only on the monodisperse case in the following discussion.

The liquid fraction profile was expected to be rather different with higher surface viscosities. To increase the surface viscosity, mixtures of SDS and dodecanol are commonly used. It is well known from forced drainage experiments that the addition of dodecanol increases the surface viscosity (up to approximately 10^{-6} kg/s) and makes the interfaces more rigid [90]. One could expect data with such a mixture to agree with the rigid model. As one can see in Figure 7.6 this is not the case. The system is well described by the model supposing mobile interfaces, exactly as with pure SDS. Other systems shown to have rigid interfaces in forced drainage experiments [56] were tested, but they are all well described by the mobile limit (see Figure 7.7). The foams from TTAB3-DOH2 with the smallest bubble size are slightly wetter than predicted by the model, suggesting that for this system the

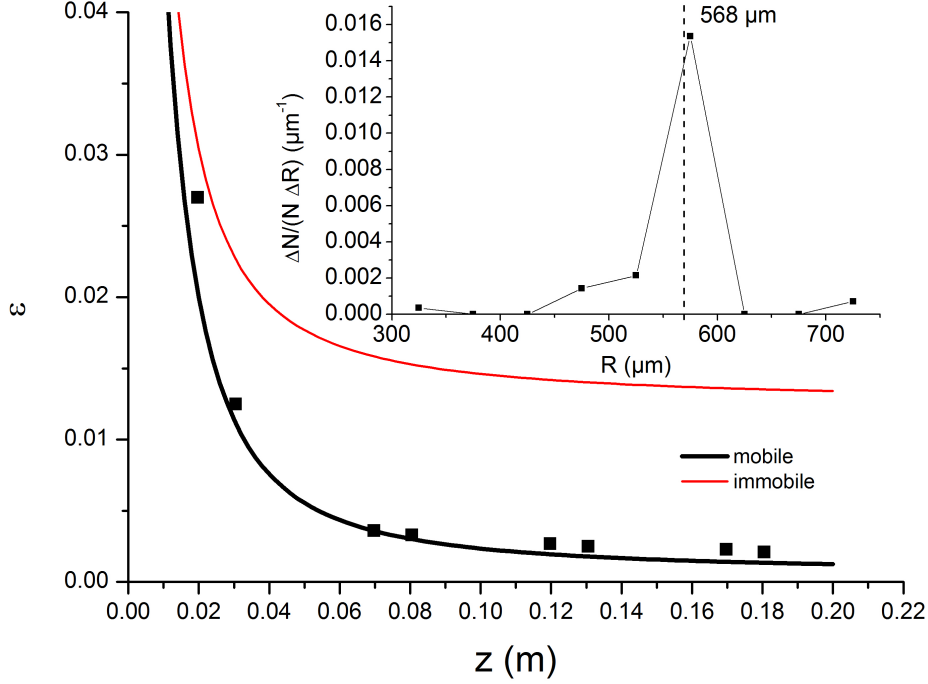


Figure 7.6: Liquid fraction profile for the SDS-DOH3 foam produced at 10 ml/min gas flow rate. Black points represent experimental data, the lines show calculated profiles in different limits. Inset: bubble size distribution.

interfaces are marginally rigid. But they are still far from being described by the rigid model.

We can start to understand why the interfaces behave as mobile if we remember that there is no soap solution with absolutely rigid interfaces. The surfaces can only be sufficiently rigid for the boundary to become important in a given flow problem.

As we have discussed in Chapter 3, the rigidity can be described quantitatively by the Boussinesq number $Bo = \mu_s/\mu R_{Pb}$. One can imagine two factors which can change Bo . First of all, note that in aged stable foam Bo is expected to vary with the position in the foams because R_{Pb} depends on both the liquid fraction and the radius of the bubbles. To estimate R_{Pb} , Equation 2.7 can be solved numerically to get $R_{Pb}(\varepsilon)$ for a given bubble size. This dependence can be converted to $R_{Pb}(z)$ using the best fit of the liquid fraction profile. It turns out at the top of the foam R_{Pb} is almost 10 times smaller than at the bottom, indicating that this effect is important for a proper calculation of the $Bo(z)$ dependence (see the inset of Figure 7.9).

The second factor which can potentially influence the surface mobility is the adsorption time of dodecanol affecting the surface tension γ and surface viscosity μ_s . To quantify this effect, I performed experiments with a rising bubble and measured the surface tension of pure SDS and SDS-DOH3 solutions as a function of time

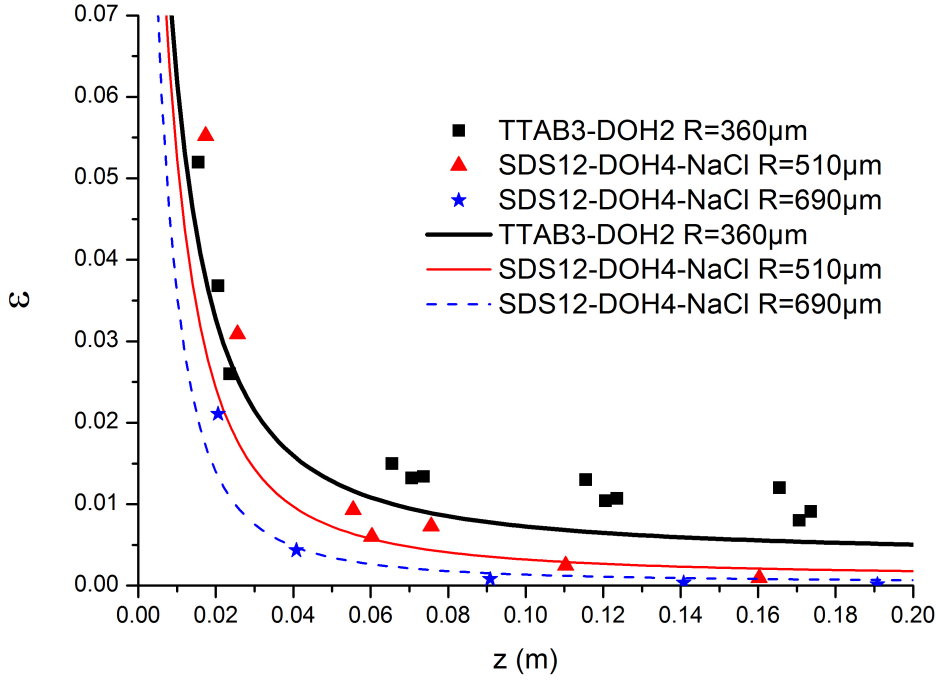


Figure 7.7: Liquid fraction profile for different "rigid" foams produced at 10 ml/min gas flow rate.

(Figure 7.8). The adsorption of SDS is so fast that the surface tension of SDS solutions is practically constant from the start of the measurement (around 1 s). But, when dodecanol is added to the system (SDS-DOH3) the surface tension continues to slightly decrease during hundreds of seconds. Note however, that this late decrease is quite small (around 0.4 mN/m). Foam generation induces a lot of convection in the volume, so one can expect that in the rising foam experiment this decrease is even smaller.

This change of surface tension is too small to influence the osmotic pressure gradient. Taking into account the surface tension gradient the last can be written, using Equation 3.43, as

$$\vec{\nabla}\Pi = \gamma\vec{\nabla}\left[\alpha\frac{(\varepsilon_{\max}-\varepsilon)^2}{\sqrt{\varepsilon}R}\right] + \left[\alpha\frac{(\varepsilon_{\max}-\varepsilon)^2}{\sqrt{\varepsilon}R}\right]\vec{\nabla}\gamma. \quad (7.6)$$

The numerical estimations show that the second term can always be neglected in our experiments, and that the equilibrium value of the surface tension can be used to calculate the osmotic pressure.

The change of surface tension is also too small to affect the shear surface viscosity μ_s . Indeed, it can be justified if we consider that the surface viscosity varies linearly with surface tension, so descending from 37.5 mN/m (pure SDS) to 30.2 mN/m (SDS-DOH), μ_s would decrease from 10^{-7} to 10^{-6} kg/s. However, within 1 s the surface tension of SDS-DOH has reached 30.6 mN/m (Figure 7.8). Therefore the

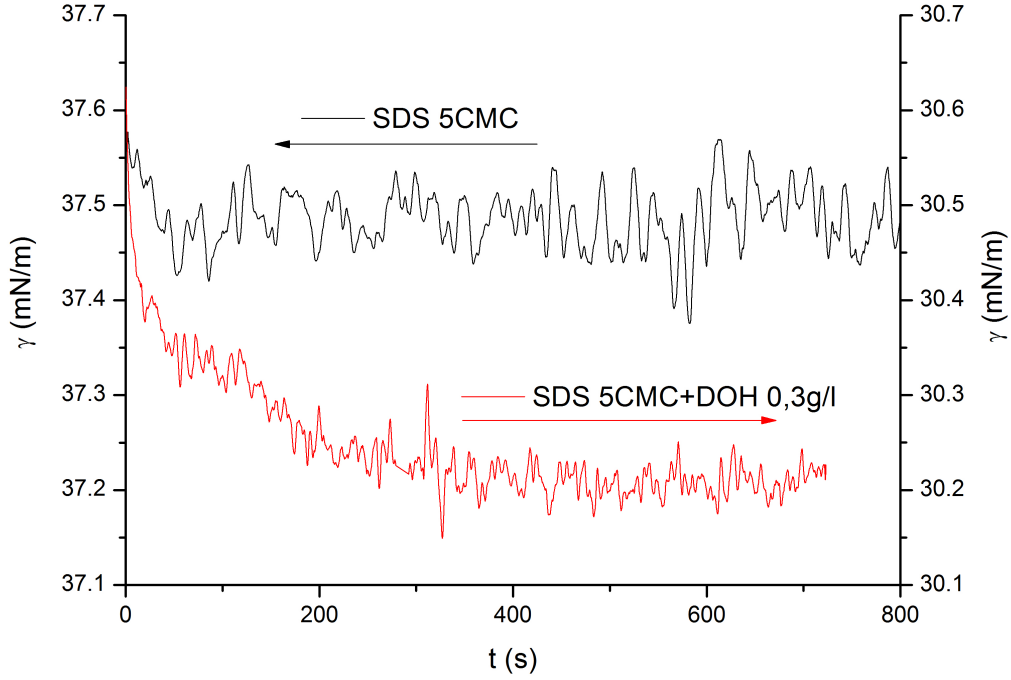


Figure 7.8: Surface tension vs time for SDS12 (thick black line) and SDSH12-DOH3 (thin red line).

maximal variation in the surface tension is around 5 % (from $0.4/(37.5 - 30.2)$) leading to a similar variation of μ_s and consequently of Bo , which hardly affects the hydrodynamic behaviour of the system. This means that Bo is much more affected by the dryness of the foam than by the value of μ_s .

Summing up, one can conclude that the equilibrium surface tension and surface viscosity can be used to estimate Bo , the only factor significantly influencing Bo is the change of R_{pb} with height. The values for Bo as a function of foam height are plotted in Figure 7.9 with two bounding values of μ_s (bare SDS or SDS-DOH). One can see that at the bottom of a foam stabilized by a solution of SDS/Dodecanol, Bo is close to 1 indicating a mobile behaviour. Boussinesq number increases with height indicating a high interfacial stress (rigid limit) at the top. However, the mobility of the foam at the bottom, close to the generation point, determines the behaviour of the entire foam. If the liquid flux is limited at the bottom of the foam, it cannot be amplified downstream.

It is useful to explain a principal difference of our experiments with the forced drainage experiments for SDS+dodecanol and TTAB+dodecanol mixtures [60]. In the forced drainage experiments foaming solution is added from the top of the prepared in advance dry foam [52]. In this case the forced drainage is normally performed at a low liquid fraction corresponding to a small radius of curvature. As a consequence Bo is always sufficiently high and the foam under investigation al-

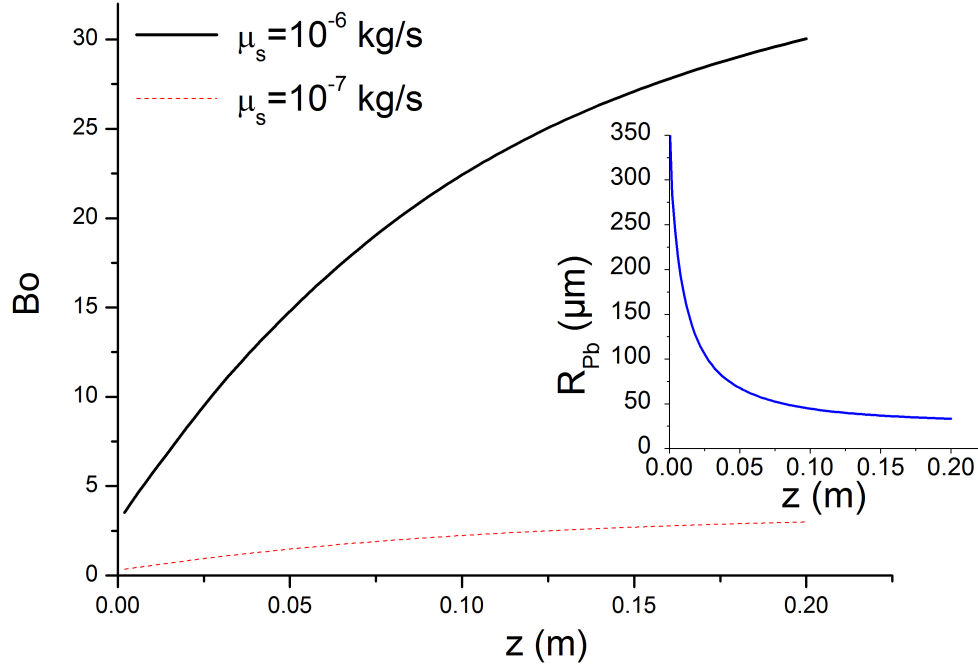


Figure 7.9: Boussinesq number Bo for "rigid" ($\mu_s = 10^{-6}$ kg/s) and "mobile" ($\mu_s = 10^{-7}$ kg/s) surface viscosities vs height. The best fit of the liquid fraction profile shown in Figure 7.6 was used in calculations. Inset: the Plateau border radius of curvature R_{pb} vs height.

ways shows a rigid behaviour with the rigid surface mixtures in the forced drainage experiments whereas it is not a case for rising foams. The two methods of foam characterization, namely the forced drainage and rising foam experiments, are intrinsically different and it should not be so surprising that they show a different foam behaviour.

7.5 Conclusion

The liquid fraction profile in rising foam has been studied using a classical model of foam drainage with Darcy's law. The pressure gradient includes both gravity and osmotic pressure, and through the permeability we account for the mobility of the interfaces using recent expressions obtained from forced drainage experiments. The model describes experimental data on systems with mobile interfaces very well. The results show that the liquid fraction depends very weakly on the ordering at the bottom of the foam and that in bidisperse bubble distributions the larger bubble sizes control the foam drainage.

The model predicts higher liquid fractions if the interfaces are rigid. However, in the described experiments systems which behave as rigid in forced drainage, behave

as mobile ones. This can be explained by considering that close to the bottom the high liquid fraction of the foam always results in the relative rigidity of an interface corresponding to the mobile limit. The fast drainage at the bottom of the foam fixes the liquid flux leading to dryer foam than could have been expected.

Through these results one can see once more that the concept of mobile or rigid interfaces should be treated with caution as it is not only dependent on the physical chemistry of the interfaces, but also on the problem under consideration. Thus a system that behaves as rigid in one problem can behave as mobile in another.

Chapter 8

Electrical and flow conductivity of quasi-two-dimensional foams

8.1 Introduction

Particle laden foams and foamed emulsions separate in a gravity field due to particle sedimentation and liquid drainage. Being coupled, these effects can lead to non-trivial profiles of foaming solution, gas and particle volume fractions by height [91]. The experimental measurements of these fraction profiles is awkward in real 3D foams. In this thesis vertical quasi-2D foams (monolayers of bubbles squeezed between two plates) have been chosen as a tool to investigate foams doped with microparticles. A valuable information of quasi-2D foam geometry can be extracted simply from image treatment which is awkward for classical 3D foams, yet many physical phenomena linked to gravity-driven flows can be analogously studied.

If we use non-conducting particles, which is often the case, valuable information about the aqueous phase content can be obtained from electrical conductivity measurements [92]. For 3D foams without particles the relative conductivity σ (being the ratio of the foam σ_f and the liquid σ_l conductivities) is found to be primarily a function of the liquid fraction ε and does not depend on the bubble size [67]. Theories describing the exact form of this function are well elaborated for three-dimensional foams [52] in two limiting cases of dry and wet foams. In the dry limit $\varepsilon \lesssim 0.05$ for 3D foams the Plateau borders may be approximated by straight conductors [52]. Taking into account the topology of the foam, considered to be isotropic, Lemlich predicted that [93]

$$\sigma = \frac{1}{3}\varepsilon. \quad (8.1)$$

which has been confirmed by numerous experiments [16, 52, 67]. The equation does not take into account the effect of nodes. But for dry foams the nodes typically contain negligible amounts of liquid in comparison with the Plateau borders and do not significantly influence the conductivity [52]. In the case of anisotropic dry foams it was shown that Lemlich's limit gives an exact upper bound for the conductivity [94].

The well-known Maxwell equation [95] describes conductivity of a media with

random spherical insulating inclusions

$$\sigma = \frac{2\varepsilon}{3 - \varepsilon}. \quad (8.2)$$

This equation is correct in the very wet limit ($\varepsilon \gtrsim 0.36$) for isolated spherical bubbles in a liquid.

In between the dry and the wet limits different semi-empirical relations have been suggested [52, 67, 96] in order to smoothly link them. The above-mentioned limits can be easily rewritten in a two-dimensional space for a hypothetical "true" 2D foam. Such foams do not exist in reality but represent a useful theoretical model. The 2D Lemlich formula gives [93]

$$\sigma_{2D} = \frac{1}{2} \varepsilon_{2D}. \quad (8.3)$$

where σ_{2D} and ε_{2D} are two-dimensional conductivity and liquid fraction, respectively. The 2D Maxwell equation becomes [95]

$$\sigma_{2D} = \frac{\varepsilon_{2D}}{2 - \varepsilon_{2D}}. \quad (8.4)$$

However the above-mentioned 2D equations cannot be directly applied to quasi-2D foams. To properly describe the electrical conductivity of quasi-2D foams their real three-dimensional geometry should be taken into account. As far as I know it has never been done before. This is surprising, considering that conductivity measurements may provide an easy solution to the challenge of determining the liquid content of quasi-2D foams which are used by many researchers to access foam properties at the bubble scale.

In the present chapter a model describing the quasi-2D foam geometry is shown and geometrical parameters, which can be extracted from experimental data simply using photographs, are proposed. Using the example of ordered, monodisperse foams we discuss how the electrical conductivity can be related to these parameters and how it can help us to investigate the geometry of quasi-2D foams. We also see how the drainage in quasi-2D foams can be accounted for. In future these results can be used to study quasi-2D foams with particles.

A home-made Hele-Shaw cell is used to study quasi-2D foams. The detailed description of the experimental set-up and data treatment can be found in Section 5.4.3. A solution of Sodium Dodecyl Sulfate (SDS) is used to generate foam. The surfactant concentration is kept constant at 12 g/L (approximately 5 times the critical micelle concentration) to avoid any surfactant depletion during the generation of the foam. The results presented in this chapter are published in [97].

8.2 Geometry of quasi-2D foams

To describe the properties of quasi-2D foams detailed information about their three dimensional structure is necessary.

Though our experimental foams are never perfectly ordered we will limit our theoretical discussion to the case of ordered monodisperse foams in equilibrium.

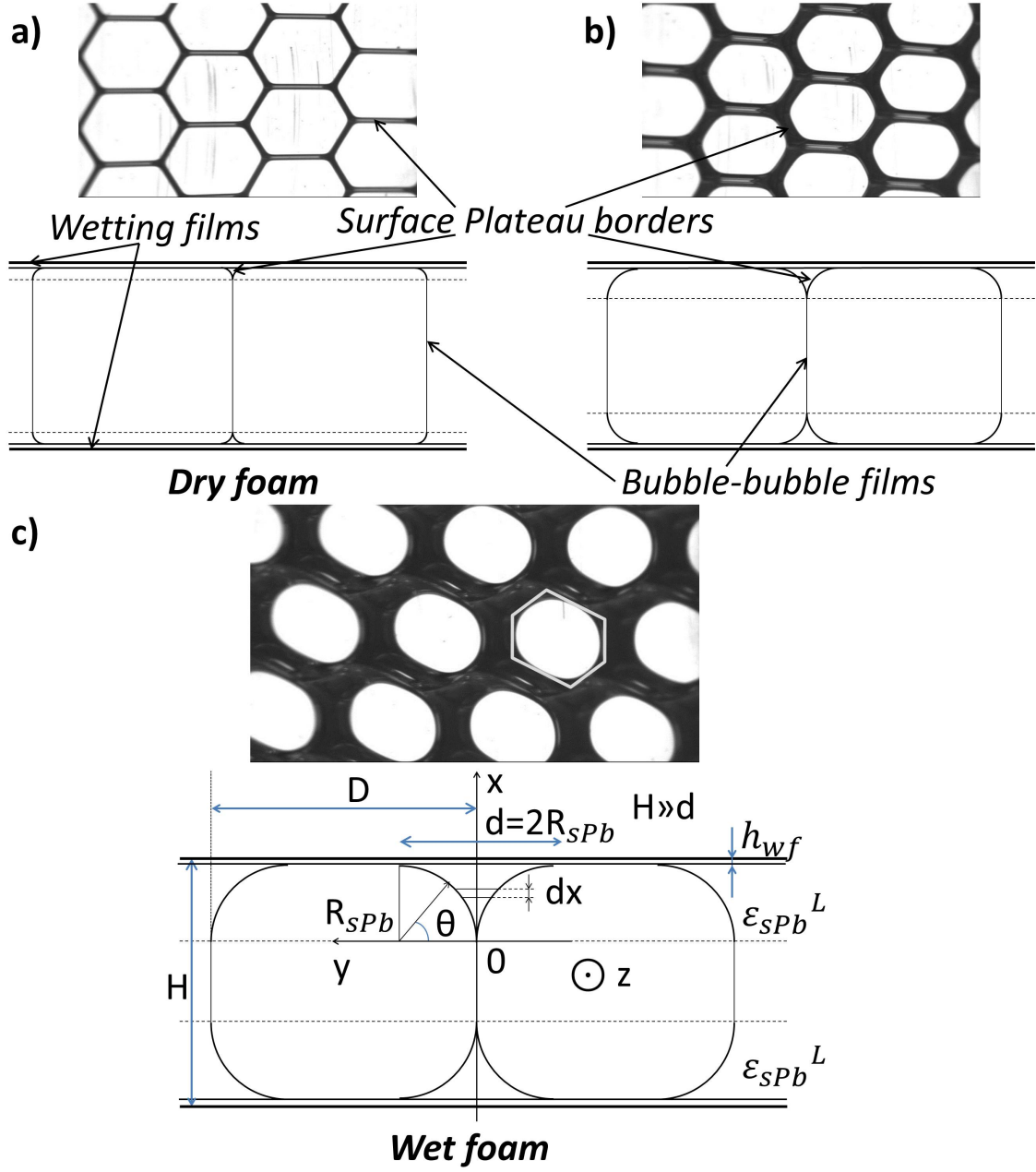


Figure 8.1: A top view and a cross-sectional view perpendicular to the walls for different liquid fractions. A transition from dry to wet limit is shown. The situation depicted here corresponds to the case when the surface Plateau border radius of curvature R_{sPb} is much smaller than the distance between the plates H . A hexagon circumscribing a single bubble is shown by a solid grey line.

They are much easier to model and have been found to be very useful for the description of real foams [98]. The structure of monodisperse quasi-2D foam is represented in Figure 2.4. As it was discussed in Chapter 2 quasi-2D foam consists of two honey-comb networks of surface Plateau borders, genuine Plateau borders connecting these networks, nodes connecting three surface Plateau borders with one

genuine Plateau border, two wetting films covering the surfaces of the plates and films between bubbles.

In quasi-2D foams all these components make a contribution to the total liquid content but only the surface Plateau borders and wetting films play an important role for the electrical conductivity. This is because the genuine Plateau borders are perpendicular to the electrical flow. The electrical potential is constant along the genuine Plateau borders and their liquid content has negligible influence on the conductivity. The films separating bubbles are always thin in comparison to the surface Plateau borders, that is why the conductivity through them can be neglected. A contribution of the wetting films can be taken into account as explained in Chapter 5. I will therefore pay attention in the further discussion of the quasi-2D foam structure only to the surface Plateau borders.

I consider here the case of two completely separated surface Plateau border networks characterized by a radius of curvature R_{sPb} much smaller than the gap between the plates, i.e. $R_{sPb} \ll H$. A corresponding cross-sectional view perpendicular to the walls is shown in Figure 8.1. In this case the surface networks can be considered as completely independent which significantly simplifies the theoretical description. Also, in the described geometry $R_{sPb} = d/2$ [23], the surface Plateau border radius of curvature can be easily extracted from the photos. So our discussion is limited only to this case and in the experiment the foam is always maintained in the above described regime.

It is worth explaining the difference of our geometry with one described by C. Gay et al. in [23] (see Chapter 2 for more details). In Gay's work different ratios between the surface Plateau border curvature and distance between plates R_{sPb}/H were considered, but only dry foams were studied. Our goal is to describe both dry and wet limits. However, for the sake of simplicity, we will limit our discussion only to high gaps between the plates. Of course, in the limit of dry foams and $R_{sPb} \ll H$, we should get comparable predictions.

The liquid content in the surface Plateau border network ε_{sPb} can be naturally determined as a ratio of the volume of the surface Plateau borders to the total volume of the foam.

However, defined in this manner the surface Plateau border liquid fraction has an important drawback. It depends on the gap between the glass plates and cannot represent the real state of the surface network. One can virtually increase the gap without any change of surface Plateau border structure. So it can not be used as a parameter characterizing the foam geometry in a unique manner. A value free of these disadvantages is a *layer liquid fraction*, which only considers the layer of height R_{sPb} as shown in Figure 8.1. It can be expressed as

$$\varepsilon_{sPb}^L = \varepsilon_{sPb} \frac{H}{d}. \quad (8.5)$$

Thus determined the layer liquid fraction reflects the real state of the network. The surface Plateau border network can be modelled as a stack of infinitely thin slices parallel to the wall (see Figure 8.1c). This allows the layer liquid fraction to be determined by integration

$$\varepsilon_{sPb}^L = \frac{2}{d} \int_0^{d/2} \varepsilon_{2D}(x) dx, \quad (8.6)$$

where $\varepsilon_{2D}(x)$ is a 2D liquid fraction in a slice at a height x . To further simplify the calculations an angle θ is introduced as shown in Figure 8.1c. Then the 2D liquid fraction in a given cut can be determined from simple geometrical arguments and written as

$$\varepsilon_{2D}(\theta) = 1 - G \left(1 - \frac{d}{D}(1 - \cos(\theta)) \right)^2, \quad (8.7)$$

where G is a *bubble shape factor* depending on the shape of the bubble cross-section in a given cut. Mathematically it can be defined as the ratio of the bubble area to the area of a circumscribed regular hexagon (see Figure 8.1c). Two important limiting cases for the bubble shape geometry can be distinguished: hexagonal and circular. The first regime is experimentally observed for dry foams (Figure 8.1a) while the second one is obtained for wet foams (Figure 8.1c). It can be easily shown that for circular bubbles $G = \frac{\pi}{2\sqrt{3}} \approx 0.906$, while for hexagonally-shape bubbles $G = 1$.

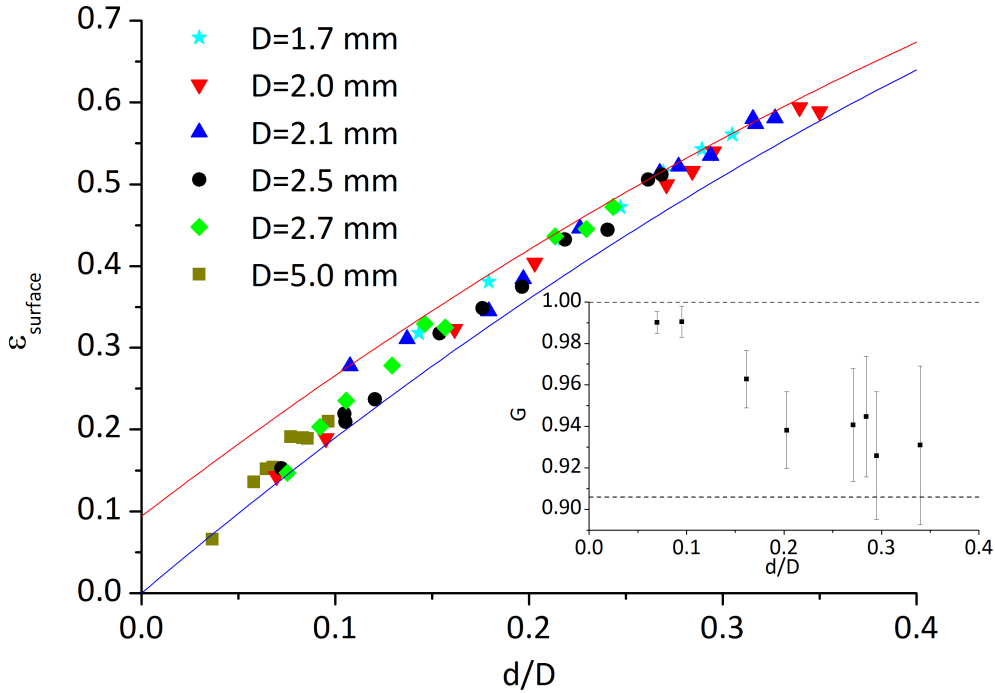


Figure 8.2: Wetted fraction of the wall $\varepsilon_{surface}$ vs d/D . Blue and red lines correspond to the prediction of the equation 8.8 in the dry ($G = 1$) and wet ($G = \pi/(2\sqrt{3})$) limits respectively. Inset: G vs d/D dependence.

For $\theta = \pi/2$ the 2D liquid fraction corresponds to a wetted fraction at the wall $\varepsilon_{surface}$ which can be extracted from the foam images such as shown in Figure 5.5. Inserting $\theta = \pi/2$ into the Equation (8.7) gives

$$\varepsilon_{surface} = \varepsilon_{2D}\left(\frac{\pi}{2}\right) = 1 - G + 2G\frac{d}{D} - G\left(\frac{d}{D}\right)^2. \quad (8.8)$$

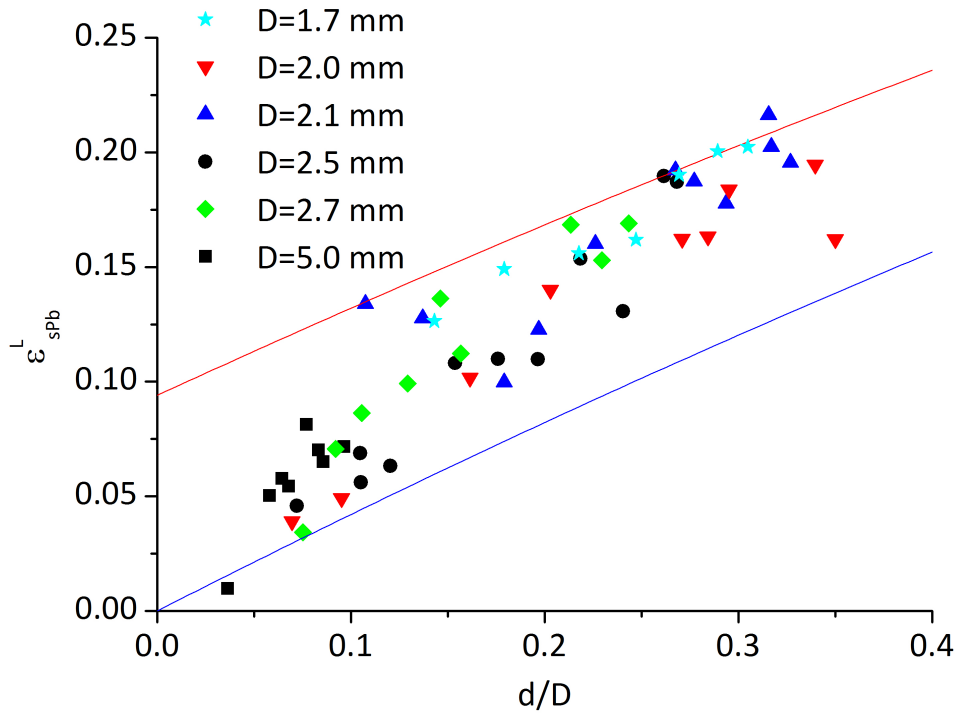


Figure 8.3: The layer liquid fraction ε_{sPb}^L as a function of d/D . Blue and red lines correspond to the prediction of the equation (8.10) in the dry ($G = 1$) and wet ($G = \pi/(2\sqrt{3})$) limits respectively.

Equation (8.8) gives us a way to evaluate G directly from the experimental data

$$G = \frac{1 - \varepsilon_{surface}}{(1 - \frac{d}{D})^2}. \quad (8.9)$$

Figure 8.2 shows the experimentally measured wetted fraction and G vs d/D . One can see that for small d/D foam can be considered as being dry ($G \approx 1$), while for d/D higher than 0.1 a transition to the wet limit can be clearly observed ($G \approx 0.906$). For small d/D and consequently dry foams G is close to 1 but with an increase of d/D it decreases. As it can be observed from photographs in Figure 5.5 bubbles get rounder as G increases.

The evaluation of the integral in Equation (8.6) in combination with Equation (8.7) finally gives an expression for the layer liquid fraction

$$\varepsilon_{sPb}^L = (1 - G) + \left(2 - \frac{\pi}{2}\right) G \frac{d}{D} + \left(\frac{\pi}{2} - \frac{5}{3}\right) G \left(\frac{d}{D}\right)^2. \quad (8.10)$$

The third term in Equation (8.10) is always small and can be neglected. So the layer liquid fraction can be expressed as a linear dependence on d/D

$$\varepsilon_{sPb}^L = (1 - G) + \left(2 - \frac{\pi}{2}\right) G \frac{d}{D}. \quad (8.11)$$

In the dry limit ($G \rightarrow 1, d/D \rightarrow 0$) the expression 8.10 simplifies to:

$$\varepsilon_{sPb}^L = \left(2 - \frac{\pi}{2}\right) \frac{d}{D}. \quad (8.12)$$

This approximation is in a good agreement with the theoretical results of previous work [23].

Equations (8.9) and (8.10) allow us to calculate the layer liquid fraction of the foam from the experimental data. In Figure 8.3 the values calculated from the data are shown as a function of d/D . One can see that the layer liquid fraction goes from the dry to the wet limit and reaches relatively high values (more than 20%). It is interesting to note that almost in the whole measured range the liquid fraction is directly proportional to d/D .

In the presented section three geometrical parameters were introduced to describe the quasi-2D foam geometry: the bubble shape factor G , the ratio between the surface Plateau border thickness and the bubble separation d/D and the surface liquid fraction $\varepsilon_{surface}$. Two of them, namely d/D and $\varepsilon_{surface}$, can be directly measured from the photos and the third one (G) can be calculated from Equation (8.9). But one can ask if d/D and $\varepsilon_{surface}$ can be changed independently. Our experimental results shown in Figure 8.2 indicate that in the axes d/D and $\varepsilon_{surface}$ all data lies on one master curve. It implies that there exists a unique dependence of $\varepsilon_{surface}$ on d/D . The exact form of this dependence should be established in the future from more detailed theoretical considerations or computer simulations. However, here I can offer a polynomial fit of the data

$$\varepsilon_{surface} \approx 2.38 \frac{d}{D} - 1.89 \left(\frac{d}{D}\right)^2. \quad (8.13)$$

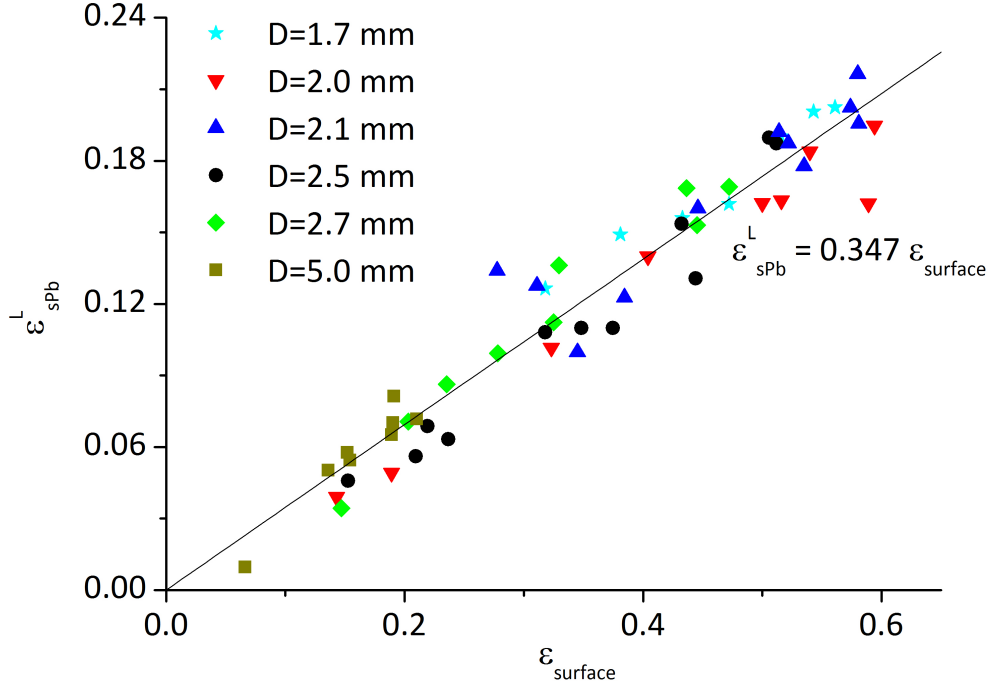


Figure 8.4: The layer liquid fraction ε_{sPb}^L vs the surface liquid fraction $\varepsilon_{surface}$

The fact that this dependence does exist means that the layer liquid fraction can be expressed as a function of one of the following variables: G , d/D or $\varepsilon_{surface}$. For future experimental work with quasi-2D foams a ε_{sPb}^L vs $\varepsilon_{surface}$ dependence is probably the most interesting, since the surface liquid fraction $\varepsilon_{surface}$ is the easiest parameter to estimate from photos. Combining Equations (8.9), (8.10) and (8.13) an approximation for $\varepsilon_{sPb}^L(\varepsilon_{surface})$ can be provided within the framework of the model

$$\varepsilon_{sPb}^L \approx 0.347 \varepsilon_{surface}. \quad (8.14)$$

Such a master curve can be very useful for experimentalists as it allows to make a fast and reliable estimation of the quantity of liquid in the network of the surface Plateau borders from the photos.

It can also be useful to note that almost in a whole measured range the liquid fraction ε_{sPb}^L is approximately directly proportional to d/D .

8.3 Electrical conductivity

First of all, one should state that in a quasi-2D foam an electrical current can pass only through the network of surface Plateau borders and through the wetting films. Genuine Plateau borders are perpendicular to the electric field and do not contribute to the conductivity. Also in most quasi-2D foams the liquid fraction in the bubble separating films is sufficiently small. It can be estimated that the

thin films contain about 10^{-3} of the total amount of liquid [99], so the conductivity through them can be neglected. The addition of the wetting film conductivity can be subtracted as explained in Chapter 5 to have a pure signal from the surface Plateau border networks. I do it systematically in all the presented data.

We consider the foam as two independent networks of surface Plateau borders as discussed in Section 8.2. It is useful to introduce a relative conductivity corresponding to one surface layer in exactly the same manner as I have already introduced the layer liquid fraction (Eqn. (8.5))

$$\sigma_{sPb}^L = \sigma \frac{H}{d}. \quad (8.15)$$

Determined in the described way *the layer conductivity* and *the layer liquid fraction* do not depend on the plate spacing and represent an actual physical state of the surface networks.

We can apply the approach used in Section 8.2 to calculate the liquid fraction. A single surface plateau border network can be represented as a parallel connection of infinitely thin conductive slices as shown in Figure 8.1. Then the relative conductivity of the whole layer can be calculated by integration

$$\sigma_{sPb}^L = \frac{2}{d} \int_0^{d/2} \sigma_{2D}(x) dx. \quad (8.16)$$

To perform an integration a link between the 2D layer conductivity σ_{2D} and the 2D liquid fraction ε_{2D} should be established.

By analogy with a 3D foam, two limiting cases for quasi-2D foams can be considered. In the limit of a dry foam each surface Plateau border can be considered as a thin straight conductor of a constant cross-sectional area and a resistance per unit length. Then the 2D Lemlich's formula (8.3) can be used. Taking into account Equation (8.10) the conductivity in the dry limit ($G \rightarrow 1, d/D \rightarrow 0$) can be written as

$$\sigma_{sPb}^L = \left(1 - \frac{\pi}{4}\right) \frac{d}{D}. \quad (8.17)$$

An alternative way to calculate the layer conductivity of the surface Plateau border networks is to apply the 2D Maxwell equation (8.4) linking a two-dimensional conductivity with the two-dimensional liquid fraction.

Using Equation (8.7) and performing a change of variable $x = \frac{d}{2} \sin \theta, \theta \in [0, \pi/2]$ the layer electrical conductivity can be represented as a function of d/D and G

$$\sigma_{sPb}^L \left(\frac{d}{D}, G \right) = -1 + 2 \int_0^{\pi/2} \frac{\cos(\theta)}{1 + G(1 - \frac{d}{D}(1 - \cos(\theta)))^2} d\theta. \quad (8.18)$$

The integral of the Equation (8.18) was numerically evaluated for different values of d/D . The results are plotted in Figure (8.5) for two limiting values of G . One can see that for the hexagonal bubbles Maxwell's approach gives a result very close to Lemlich's one for sufficiently dry quasi-2D foams. Also an enormous difference between the dry and the wet limits can be observed allowing us to anticipate that electrical conductivity can be used as a sensitive instrument to explore the three-dimensional structure of quasi-2D foams.

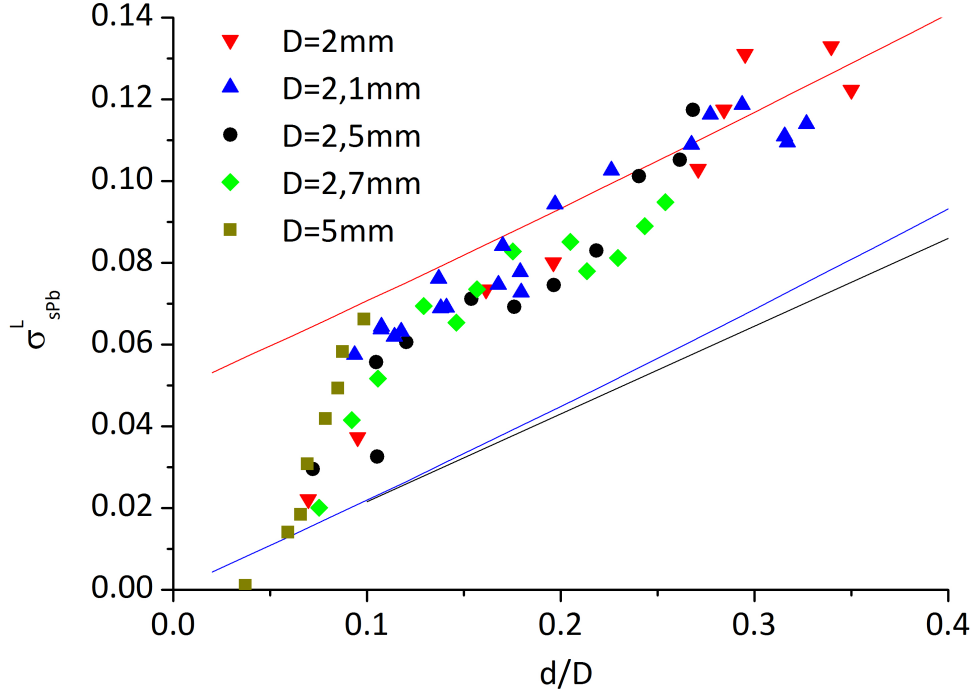


Figure 8.5: The layer electrical conductivity σ_{spb}^L vs d/D measured for different bubble sizes and liquid flow rates. Blue and red lines correspond to the prediction of the Maxwell model (Eqn. 8.18) in the dry ($G = 1$) and wet ($G = \pi/(2\sqrt{3})$) limits respectively. The black line corresponds to Lemlich's model (Eqn. 8.17).

Experimental data for the layer electrical conductivity are represented in Figure 8.5 for different liquid fractions and bubble sizes. Except for very dry foams the error bars normally do not exceed a few percent and are comparable with the symbol sizes. For dry foams ($d/D < 0.07$) a certain uncertainty in the wetting film thickness estimation can significantly influence the accuracy of electrical conductivity measurements. A clear transition between the dry and the wet limit is visible at $d/D \approx 0.1$. Such behaviour can be attributed to the transition of the foam structure from the dry to the wet limit. This can be explained by calculating the minimal surface area to make rounded bubbles. For dry foam only a hexagonal structure is possible: to curve bubbles and make them circular a certain amount of liquid is necessary. But as long as it is possible to make circular bubbles they will always have a smaller area and consequently a lower energy than the hexagonal ones. A geometrical calculation shows that the minimum liquid fraction required to make circular bubbles is about 0.094. This value corresponds to d/D about 0.11 in the hexagonal model. It means that above this value hexagonal bubbles should not exist. In practice it means that after this limit the circularity of bubbles significantly increases and the geometry dramatically changes. This corresponds extremely well with the experimentally observed transition in Figure 8.5.

The complicated geometry of quasi-2D foams can be taken into account by using

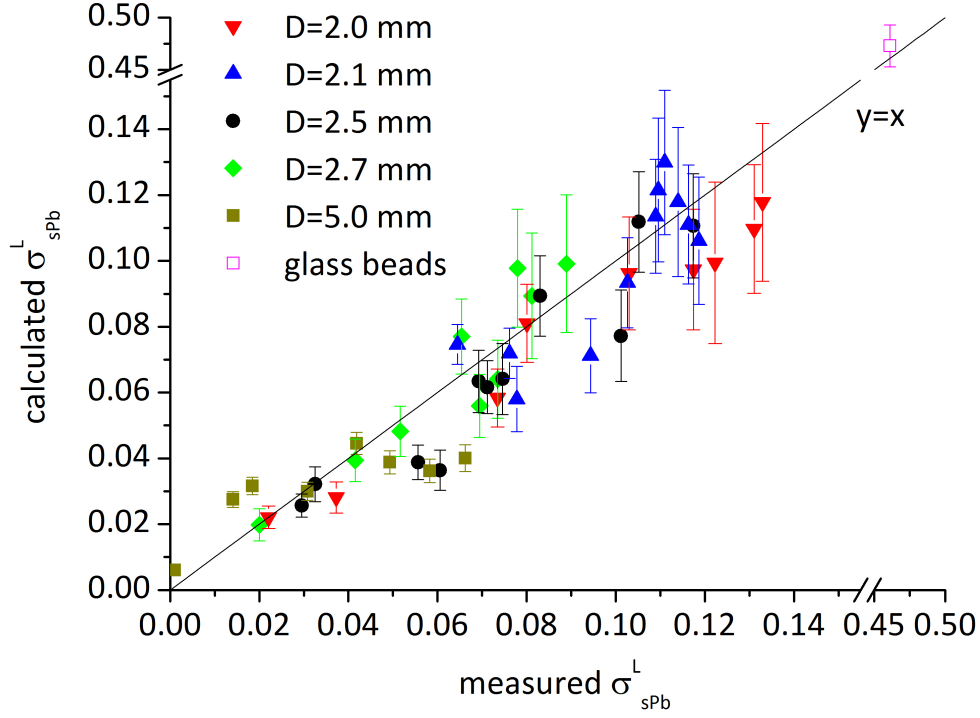


Figure 8.6: The layer electrical conductivity σ_{sPb}^L calculated by Equation (8.19) using the geometrical parameters extracted from photos vs the experimentally measured values.

the experimentally measured values of G . To simplify our calculations a linear approximation of the expression (8.18) can be used to predict σ_{sPb}^L

$$\sigma_{sPb}^L\left(\frac{d}{D}, G\right) \approx \frac{2}{\sqrt{G(1+G)}} \left(\operatorname{arctanh}\left(\sqrt{\frac{G}{1+G}}\right) - \sqrt{\frac{G}{1+G}} \right) \frac{d}{D} + \frac{1-G}{1+G}. \quad (8.19)$$

For the dry limit this approximation gives

$$\sigma_{sPb}^L\left(\frac{d}{D}\right) \approx 0.246 \frac{d}{D} \text{ (dry limit)}, \quad (8.20)$$

which agrees well with Lemlich's limit

$$\sigma_{sPb}^L\left(\frac{d}{D}\right) \approx 0.215 \frac{d}{D}. \quad (8.21)$$

In the wet limit one get

$$\sigma_{sPb}^L\left(\frac{d}{D}\right) \approx 0.240 \frac{d}{D} + 0.049 \text{ (wet limit)}. \quad (8.22)$$

The values of σ_{sPb}^L calculated by Equation (8.19) vs the experimentally measured ones are presented in Figure 8.6. The values of G are calculated from photos using

Equation (8.9). The results are in a good agreement with the experimental data and confirm our theoretical assumptions. The obtained approximations (8.20) and (8.22) can be very useful for future experimental work since they allow to estimate the electrical conductivity from photo treatment or to calculate the surface Plateau border thickness from the known conductivity data in two limiting cases of very dry and very wet foams. Along with the equation (8.10) it gives a straightforward way to evaluate the surface Plateau border liquid fraction from conductivity measurements in the above-mentioned limits.

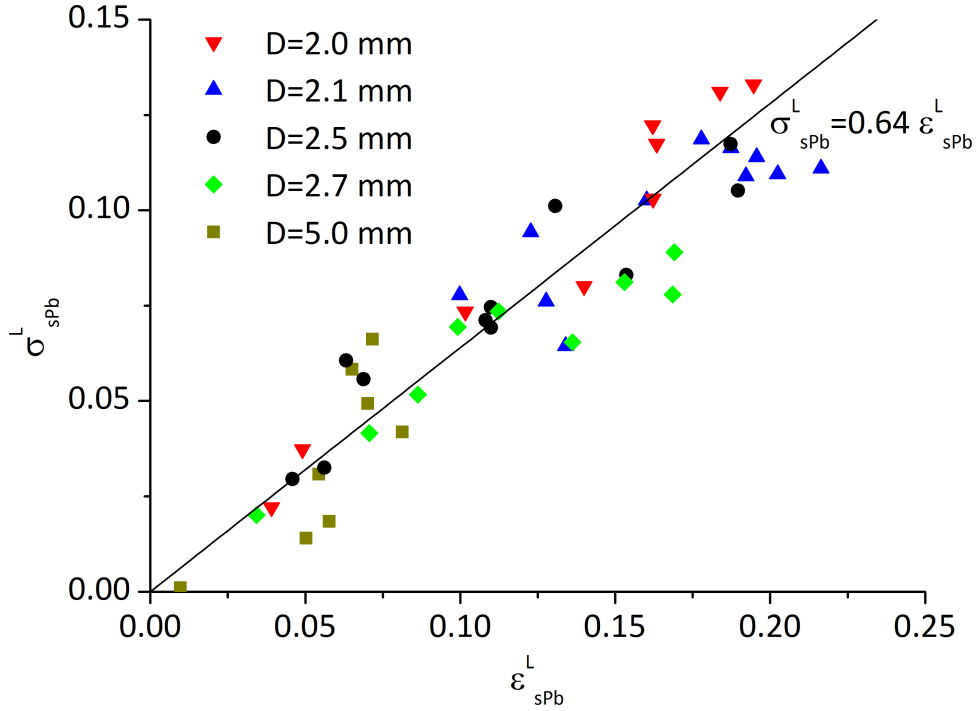


Figure 8.7: The layer electrical conductivity σ_{sPb}^L vs the layer liquid fraction ε_{sPb}^L for different bubble sizes

The dependence of the layer conductivity on the layer liquid fraction is shown in Figure 8.7. The data can be approximated by a linear relationship

$$\sigma_{sPb}^L \approx 0.64 \varepsilon_{sPb}^L. \quad (8.23)$$

This relationship can be used to rapidly estimate the liquid fraction from the electrical conductivity data.

The low error of layer electrical conductivity measurements and the high sensitivity to the change of the foam structure allows us to determine the geometry of the quasi-2D foam. To check the applicability of the developed approach for very high liquid fractions the conductivity of a glass bead monolayer surrounded by the same foaming solution was also measured. Such system corresponds to the case $d/D = 1$. The measured value of conductivity is in a full agreement with the prediction of the model as shown in Figure 8.6.

8.4 Flow conductivity

Making a complete analogy with the electrical conductivity one can state that the liquid can flow only through two networks of surface Plateau borders. It should be mentioned that the flow conductivity of the wetting film is negligible. A low velocity of the liquid close to a rigid wall has a negligible influence on the conductance of the whole foam. This assumption is also confirmed by an experimentally observed independence of the wetting film thickness on the liquid flow rate. To continue our analogy let us introduce a liquid flux through a single network of surface Plateau borders

$$Q_{sPb}^L = \frac{QH}{d}. \quad (8.24)$$

Now one can introduce *quasi-2D foam permeability* using Darcy's law as

$$K_{2D} = \frac{Q_{sPb}^L \mu}{S \nabla p_d}, \quad (8.25)$$

where S is a cross-sectional area of the foam in the plane perpendicular to the gravity field.

Two models, namely the channel- and node- dominated, can be written for 2D foams in analogy with the 3D case. The first one assumes that surface Plateau borders are straight conductors with a constant hydrodynamic resistance. If the foam is sufficiently dry, the nodes do not contribute to the viscous dissipation. Following the procedure described for 3D foam in Section 3.11 one gets in the quasi-2D foam case

$$K_{2D} = \frac{1}{2} A_{sPb} k_{sPb} \varepsilon_{sPb}^L, \quad (8.26)$$

where A_{sPb} is a cross-sectional area of a surface Plateau border and k_{sPb} is a permeability coefficient for a single surface Plateau border which depends on the surface mobility. For a completely rigid interface one finds $k_{sPb} \approx 0.02$ [58]. The prefactor $1/2$ arises from the averaging over all the surface Plateau border orientations in 2D.

Taking into account Equations 2.9 and 8.12 the permeability of quasi-2D foam in the channel-dominated limit can be finally written as

$$K_{2D} = \frac{1}{8} \left(2 - \frac{\pi}{2}\right)^2 k_{sPb} \frac{d^3}{D}. \quad (8.27)$$

In the rigid limit one has

$$K_{2D} = 4.5 \cdot 10^{-3} \frac{d^3}{D}. \quad (8.28)$$

For foams with higher liquid fractions the dissipation in the nodes may dominate. We will treat the node-dominated model for quasi-2D foams using exactly the same scaling arguments as applied earlier for 3D foams (see Section 3.11). Taking as a first order approximation that R_{sPb} and R_{Pb} have the same order of magnitude, the result for quasi-2D foam yields

$$K_{2D} \propto dD \varepsilon_{sPb}^L. \quad (8.29)$$

Assuming that the liquid fraction is directly proportional to d/D as it was discussed in Section 8.2, one can write

$$K_{2D} \propto d^2. \quad (8.30)$$

Rather unexpectedly in the node dominated model the permeability does not explicitly depend on the bubble size. Note that the channel- and node- dominated model for quasi-2D foams gives different scaling laws for the characteristic length scales d and D . A more detailed description of the drainage in 2D foams can be performed in the framework of the corresponding network model combining nodes and channels. However such a theory remains to be constructed.

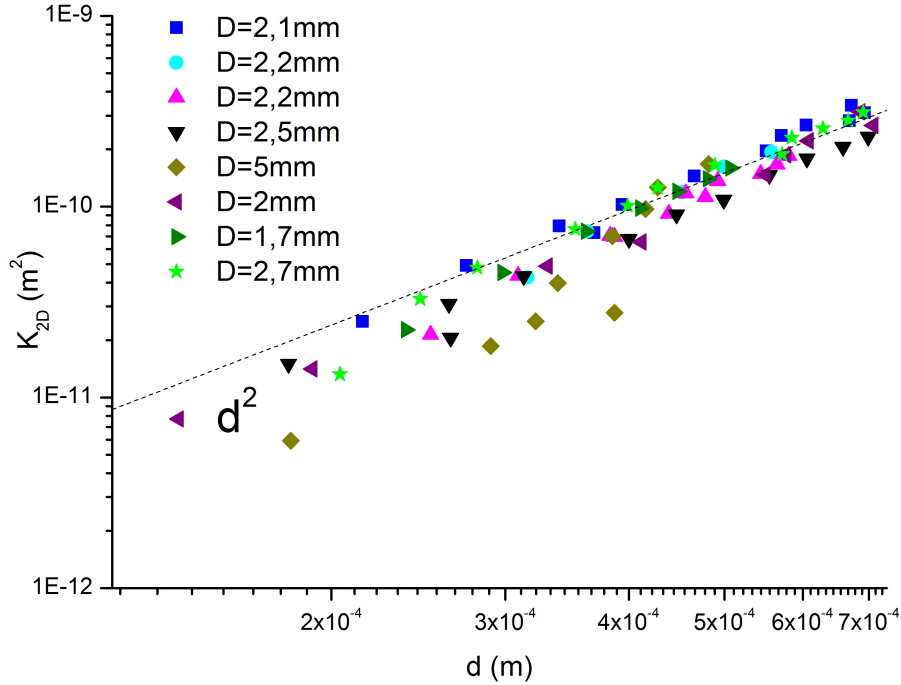


Figure 8.8: The quasi-2D foam permeability K_{2D} vs surface Plateau border size d for different bubble sizes.

Comparison with the experiment In Figure 8.8 the experimentally measured quasi-2D foam permeability is presented as a function of the surface Plateau border thickness d for different bubble sizes. It is clear that all data are on one master curve which means that the flow conductivity does not depend on the bubble size. The power-law is close to 2 in agreement with the node-dominated model.

It might seem surprising that all the data can be described using the node-dominated model. In 3D foams the channel-dominated model is preferential for either rigid interfaces or low liquid fractions while node-dominated regime is more probable for mobile interfaces at high liquid fractions. As shown in Figure 8.3, only

a few of our experiments have $G \approx 1$, and for most of the experimental points ε_{sPb}^L is sufficiently high corresponding to wet foam. This combined with the relatively low surface viscosity of SDS leads to the node-dominated behaviour of the system under investigation. A certain scattering of the results at small d can be accounted for by an influence of a flow resistance in the channels of these drier foams.

The reported behaviour is very similar to the electrical conductivity measurements mentioned above. In both cases the geometry of the vertices plays a crucial role in the correct theoretical description. The system can never be described as purely channel-dominated.

8.5 Conclusion

In this chapter a simple model to describe the geometry of a quasi-2D foam was introduced. This description was used to model the electrical and flow conductivities of quasi-2D foams. The models describe well the accompanying experiments over a wide range of liquid fractions. The experiments show that even foams at low liquid fractions have to be considered as "wet". This work can help in suggesting new approaches for the characterisation of foam properties. In particular, it should prove useful in the in-situ characterisation of foam flow in the presence of walls and in confining geometries, such as microfluidic applications [100, 101].

The described model can be applied to study foams with particles in quasi-2D configuration. The electrical conductivity can give information about the foaming solution fraction, while the image treatment gives a content of the aqueous and particle phases together. Using both techniques, the distribution of all phases can be calculated at different heights.

Chapter 9

Sedimentation of microparticles under confinement

9.1 Introduction

In the previous chapter a technique to measure the particle distribution at different positions in particle laden quasi-2D foams has been established. Now we will have a closer look on the particle sedimentation on a single Plateau border scale. A good understanding of this process is important for many practical applications. For example, it is well-known that particles can be captured in Plateau borders leading to a clogging of the foam network and arresting of the foam drainage [102, 103]. Thus the presence of particles help to make very stable foams [104].

The size of particles is usually comparable with the Plateau border radius of curvature. Thus the Plateau borders induce confinement constraints that could influence the transport properties of sedimenting particles [105]. We have seen in Chapter 3 that confinement has a strong impact on particle concentration and velocity fluctuations. Surprisingly, despite of the key role in different industrial applications many aspects of sedimentation under confinement are still poorly understood.

In this chapter we investigate the sedimentation of monodisperse polystyrene microparticles under confinement in circular capillaries. The last are used to imitate foam channels. Compared to the experiments in the quasi-2D foams, the capillaries are enclosed and do not lose matter due to liquid drainage and sedimentation of particles, making them a simpler model system.

Different ratios of capillary diameter D to particle diameter d are studied varying from 3 to 100. The experimental set-up and data treatment are described in Chapter 5.

9.2 Results and discussion

9.2.1 Sedimentation in vertical capillaries

We will start by determining a reference bulk sedimentation velocity in a non-confined media. To have the reference we consider the sedimentation of an initially homogeneous dispersion in a wide capillary, where confinement is not important

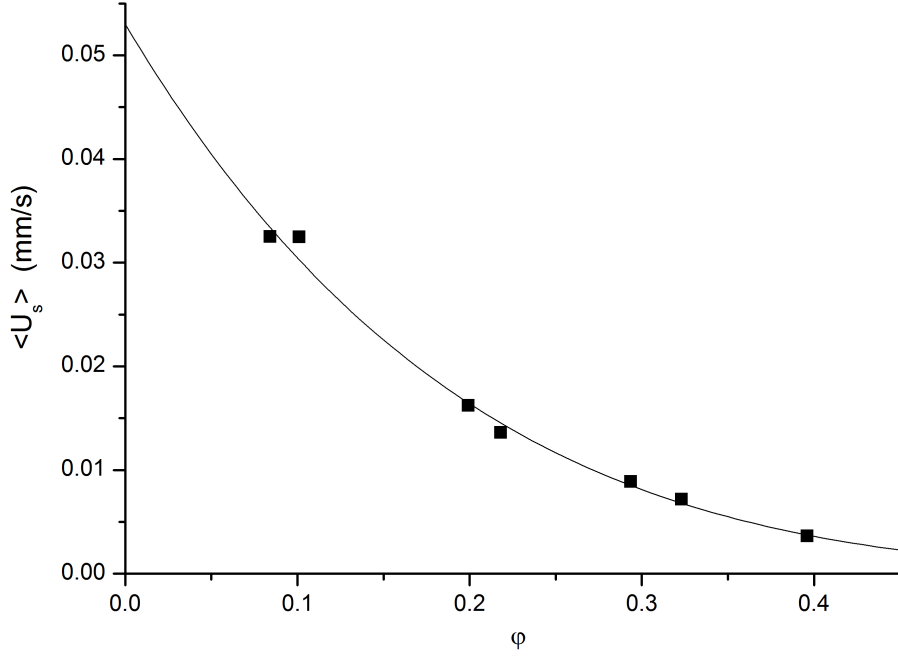


Figure 9.1: Bulk sedimentation velocity for different particle concentrations and fit with the Richardson-Zaki law (Equation 3.22, $U_p \approx 0.053$ mm/s and $n \approx 5.26$).

$D \gg d$. The measured bulk sedimentation velocity for $40 \mu m$ particles is shown in Figure 9.1 for different particle volume fractions. The experimental data can be fitted by the Richardson-Zaki law 3.22 with the exponent $n \approx 5.26$ and a Stokes velocity $U_p \approx 0.053$ mm/s. Using the experimentally measured Stokes velocity one can calculate the hydrodynamic diameter of the particles from Equation 3.19

$$d = \sqrt{\frac{18\mu U_p}{g(\rho_p - \rho)}} \approx 41.7 \mu m. \quad (9.1)$$

One can see that the hydrodynamic diameter is close to the value declared by the manufacturer indicating that the dispersion is stable against aggregation. Having confirmed that the particles sediment individually we can now continue with the study of sedimentation in circular capillaries.

The first difference between larger vials and small capillaries is that for smaller capillaries there exists an excluded volume near the walls. The particle centres cannot approach the walls closer than the particle radius $d/2$ (see Figure 5.12 in Chapter 5). This exclusion leads to an effective volume fraction in the capillaries that is higher than the corresponding bulk value

$$\varphi_{eff} = \varphi / (1 - d/D)^2. \quad (9.2)$$

The influence of the excluded volume becomes more important as D/d decreases,

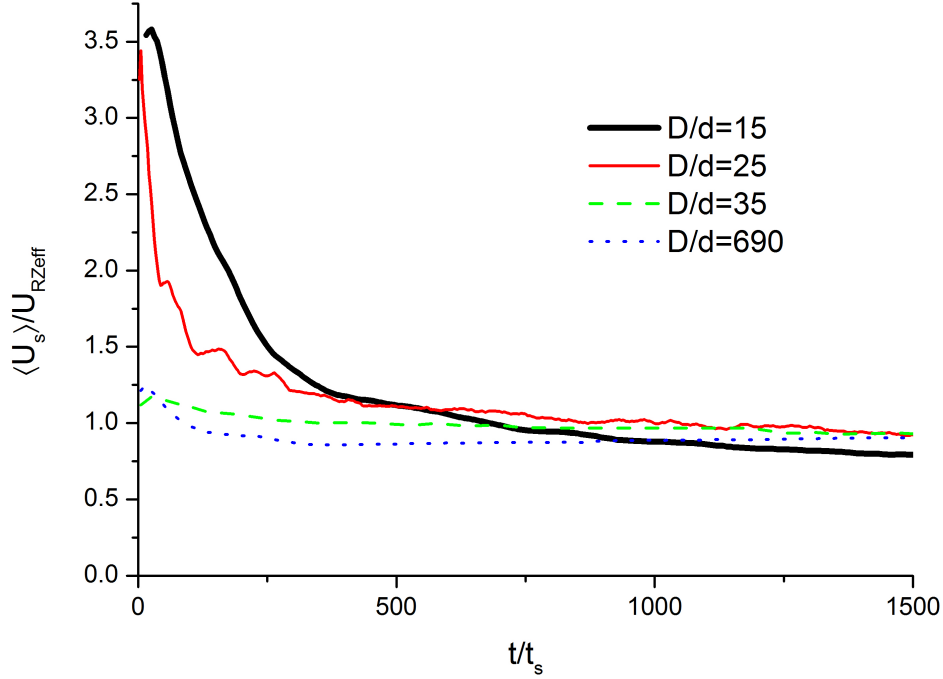


Figure 9.2: Suspension front velocity as a function of time for different confinement degree ($\varphi \approx 0.2$). The time scale is the Stokes time $t_s = d/(2U_p)$.

although already at $D/d = 30$ the maximum packing fraction has decreased from 0.64 to 0.57, and is only 0.50 at $D/d = 10$. Therefore we can expect that for the same average total volume fraction the sedimentation should be slower in smaller capillaries as the effective volume fraction is higher. This can be taken into account by inserting the effective volume fraction into the Richardson-Zaki law, and keeping n constant. One gets an effective bulk sedimentation velocity

$$U_{RZeff} = U_p(1 - \varphi_{eff})^n. \quad (9.3)$$

Figure 9.2 shows the sedimentation front velocity normalised by U_{RZeff} as a function of time for initially homogeneous dispersions in capillaries. Surprisingly, the experimental results show that at early stages just after the filling of capillaries the sedimentation velocity is higher than the effective bulk value. The velocity decays with time and reaches a steady-state close to the value predicted by the corrected Richardson-Zaki law 9.3. The described acceleration effect disappears as the capillary size increases.

The speeding-up of sedimentation under confinement has been recently described in [106]. It was suggested that the acceleration can be related with formation of stable concentration fluctuations. The fluctuations create particle-rich and particle-poor lanes so that the water backflow can rise through particle-poor regions with smaller hydrodynamic resistance. The fluctuations are shown to be important at initial stages of sedimentation and decay with time [41, 42]. The characteristic

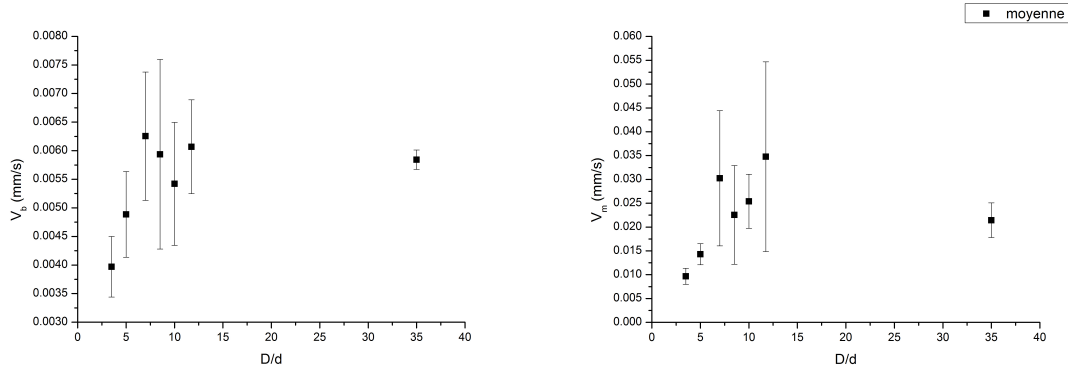


Figure 9.3: Velocity of the suspension/sediment front U_b (on the left) and the average sedimentation rate of particles U_m (on the right) for different confinement degrees D/d .

time-scale of fluctuation decay is comparable with the time during which the sedimentation velocity decreases in our experiments (see Figure 3.4 for comparison).

However, we should keep in mind that the observed behaviour can also be explained by a poor control of the initial state of the experiment. For example, the capillary rise, which is used to fill the capillaries, can result in a particle concentration gradient. If the dispersion is more dilute at the top, the front velocity is faster at the initial stage of sedimentation.

To better control the initial state I focus my attention on the plug configuration, where particles are collected at the top of the sample at the beginning of the experiment. The details of this configuration are described in Chapter 5. In the plug configuration the system consists of the plug at the top, sediment at the bottom and a homogeneous sedimenting suspension in the middle. The dynamics of the plug configuration can be described by three velocities: a velocity of the front between the plug and the suspension U_t , a velocity of the front between the sediment and the suspension U_b and the average sedimentation rate of particles in the suspension U_m . All three velocities can be measured experimentally and it turns out that the system rapidly reaches a stationary regime, where $U_t \approx U_b$. As we can reasonably assume that $\varphi_t \approx \varphi_b \approx \varphi_{effmax}$, the fraction of particles in the middle of the capillary remains constant during the sedimentation. This average particle fraction in the suspension φ_m can be calculated from Equation 5.5.

In the plug configuration I have never observed any time dependences for the velocity of sedimentation. The system always has enough time to homogenise and destroy any initial fluctuations. Figure 9.3 shows the velocities U_b and U_m as a function of confinement degree. Each experimental point is an average of at least 5 measurements. We can see that both velocities increase with D/d and reach a constant value at $D/d \sim 7$. The velocities U_b and U_m are used to calculate the suspension particle fraction φ_m , the results are presented in Figure 9.4. We note that the suspension particle fraction almost does not depend on D/d and is constant at around 0.10, it means that the velocities U_b and U_m self-adjust to keep φ_m constant.

The measured sedimentation velocities can be normalised by that expected from

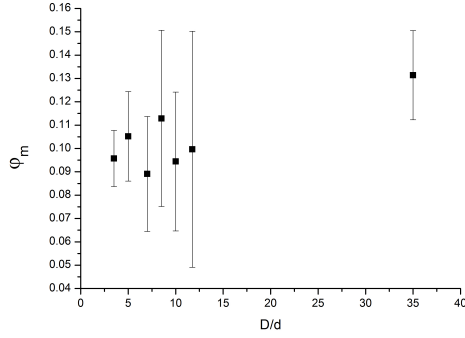


Figure 9.4: Particle volume fraction as a function of confinement degree D/d .

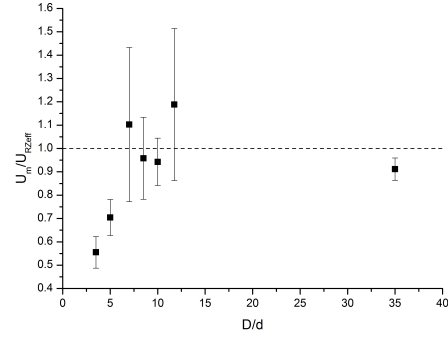


Figure 9.5: Normalised sedimentation velocity U_m/U_{RZeff} for different confinement degrees D/d .

the Richardson–Zaki for the given volume fraction as U_m/U_{RZeff} for different confinement degrees (see Figure 9.5). One can see that for $D/d \geq 7$ the experimental results are close to the values predicted by the corrected Richardson-Zaki law 9.3. For smaller D/d the relative velocity increases with the capillary size. This is due to hydrodynamic interactions between particles and walls, which slow down the liquid flow around the particles.

Summing up, we can conclude that in the plug configuration, where initial inhomogeneities and velocity fluctuations are not important, the influence of confinement is only due to excluded volume effect for sufficiently big capillaries ($D/d \geq 7$). For smaller capillaries the no slip condition for liquid flow close to the walls results in the decrease of sedimentation velocity.

9.2.2 A closer look on the onset of sedimentation: Rayleigh-Taylor instability

In the previous section we have explained the $U_m(\phi_m)$ dependence, however, it is still not clear, how the suspension/plug front velocity U_t is fixed. What controls the velocity at which the particles will sediment. To better understand the factors controlling the departure of particles from the plug, let us take a closer look at the beginning of the sedimentation using high-magnification lenses. It turns out that two types of behaviour can be observed: fluid-like and solid-like (see Figure 9.6).

In the solid-like case single particles leave the plug, the process looks like a melting of the solid phase. After the capillary has been turned almost around nothing happens for the first 20 or 30 seconds, it is only after this latency that individual particles start detaching. This process continues for a certain time until suddenly the whole plug is set in motion exactly as in the fluid case.

The fluid-like behaviour resembles the classic Rayleigh-Taylor instability at a liquid-liquid interface described in Chapter 3. In my experiments a single "finger" forms in the system. With time the finger penetrates in the water phase and takes a helix-like shape. The characteristic width of the finger d_f is shown to increase with the capillary size (see Figure 9.7). The helix configuration allows water to

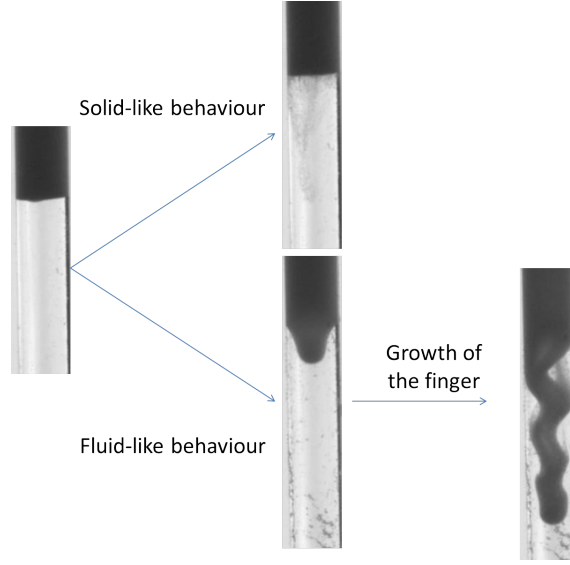


Figure 9.6: Different types of plug departure behaviour.

rise separately and it significantly increases the sedimentation velocity. The typical velocity of finger growth is about 1 mm/s, which is much higher than the Stokes velocity.

Both fluid-like and solid-like behaviour can be observed for the same sample and it is not very clear, how the system choose the preferential one. It seems from the experiments that the main parameter controlling the choice is the compactification time, which is the ageing time between the end of the sediment formation after filling and turning of the capillary. For higher compactification time the sediment has more time to form a more dense crystal-like solid phase. In this case the solid-like behaviour is preferential.

To explain and further understand the observed behaviour we are currently working with theoreticians performing Lattice Boltzmann simulations of the system under investigation. In this way the full particle trajectories can be followed and the whole process analysed. The preliminary results of the simulations starting with packed volume fractions slightly below close packed are qualitatively similar to the fluid-like behaviour of the system seen experimentally (see Figure 9.8). The simulations predict that there exist a critical initial particle fraction and even a slight increase of packing volume fraction above this limit results in formation of crystal-like solid phase, which melts before the sample starts to flow. A similar transition from solid flow behaviour to a fluid like Rayleigh-Taylor instability has been described for particle suspensions confined between two horizontal plates in [49].

9.2.3 Sedimentation in inclined capillaries: Boycott effect

In the previous sections the sedimentation in vertical capillaries has been considered. The effect of capillary inclination angle, θ , is also investigated. Figure 9.9 shows U_m and φ_m as a function of θ for different confinement degrees. For vertical capillaries $\theta = 0^\circ$ and for horizontal ones $\theta = 90^\circ$.

When $\theta < 15^\circ$ the particle velocity increases with the angle of inclination due to

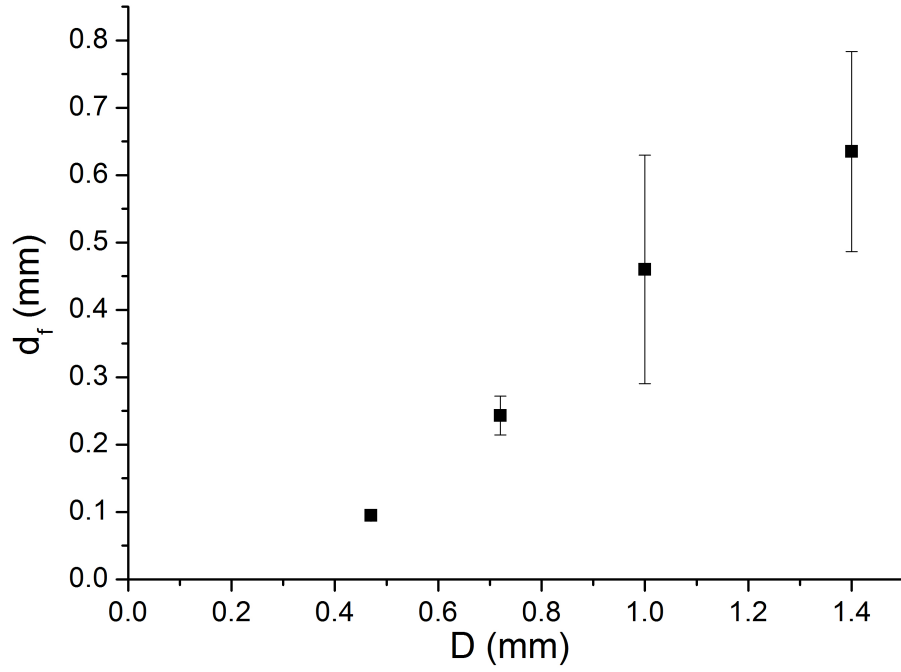


Figure 9.7: Characteristic width of the finger for different capillary diameters D . the results correspond to $10\ \mu m$ particles.

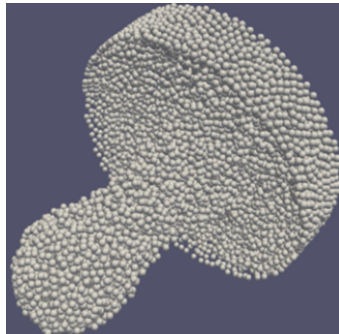


Figure 9.8: Simulation of sedimentation from plug configuration ($D/d = 40$).

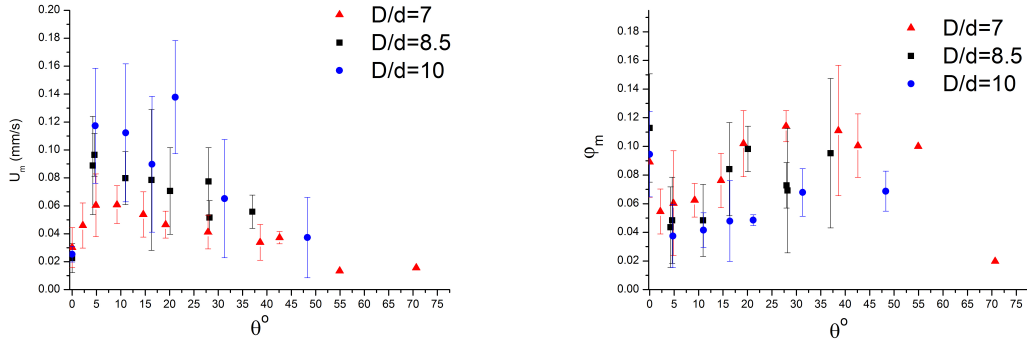


Figure 9.9: Particle sedimentation velocity U_m (on the left) and particle volume fraction φ_m (on the right) as a function of θ for different confinement degrees.

formation of separate water and suspension lanes. For bigger angles U_m start to decrease again with θ and the sedimentation slows down to almost 0 at approximately 55° . A similar behaviour has been previously reported for a buoyancy-driven flow of two fluids in narrow tubes starting from the plug configuration [107]. It was suggested that the fluid velocity goes down at high angles due to the decrease of gravity force component parallel to the tube $\Delta\rho g \cos(\theta)$ with increase of θ . The increase of the velocity with angle is more pronounced the larger the capillary, with $D/d = 10$ the increase is around 6-fold, while with $D/d = 7$ it is only 3 times higher at the maximum than in vertical capillaries. Surprisingly, the particle fraction is relatively high in vertical capillaries $\theta = 0^\circ$, but rapidly drops down as θ increases. With increasing θ the particle fraction φ_m increases up to a local maximum at about 35° . This increase is the most pronounced for the smallest D/d and it is almost absent for $D/d = 10$. Having seen that in the smallest capillaries φ_m increases with the expense of U_m as the capillary is tilted, and in the larger capillaries the effect is inverse one could imagine that the flux is roughly similar.

In order to check if this is so I calculate the particle flux through a unit area $Q/S = U_m \cdot \varphi_m$. One note that in Q/S vs θ axes all experimental data lie on a single master curve for different D/d (see Figure 9.10). This dependence also reveals a local maximum at $\theta \approx 20^\circ$. Interestingly the flux per unit area is independent of D/d .

9.3 Conclusion

In this chapter we have seen that the initial inhomogeneities and velocity fluctuations can play an important role in particle sedimentation in circular capillaries. An experimental technique allowing us to diminish these effects has been elaborated and experimentally tested. Using the initial plug configuration, it was shown that for $D/d \geq 7$ the confinement effect can be explained by the presence of the excluded volume close to the walls. The velocity in this case can be described by Richardson-Zaki law with an effective particle fraction. For smaller D/d the hydrodynamic interactions between the walls and the particles result in the deceleration of sedimentation.

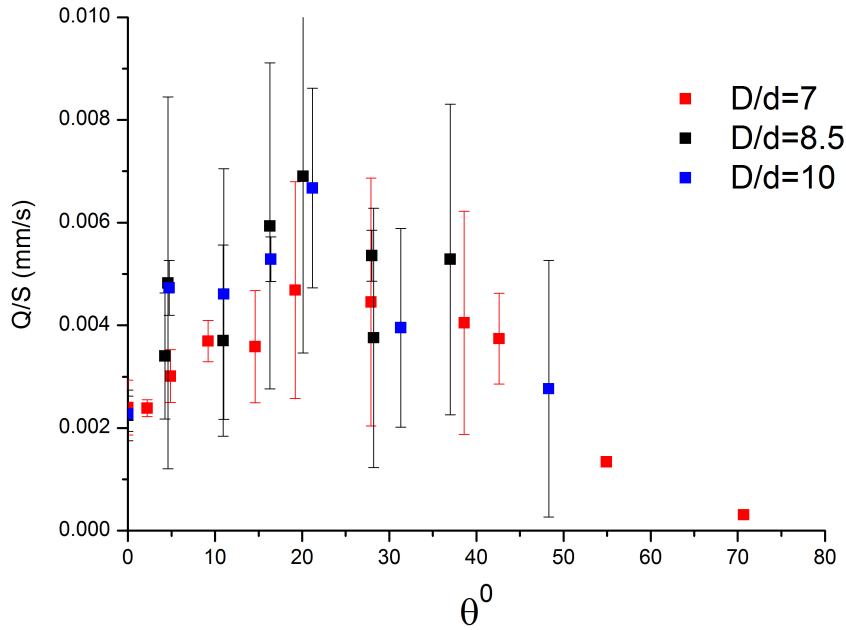


Figure 9.10: Flux of particles for different θ .

An influence of the capillary inclination angle has been studied. It was shown that sedimentation velocity and sedimentation flux exhibit local maxima at $\theta \sim 20 - 40^\circ$. At high angles $\theta > 70^\circ$ the sedimentation stops.

The development of perturbations have been studied in the plug configuration, where all particles are collected at the top of the capillary. It was shown that there exist two types of particle behaviour: solid-like and fluid-like. The former resembles the melting of the solid crystal, while the latter appears like a "classical" Rayleigh-Taylor instability at liquid/liquid interface.

Of course, all described results are applicable for a creaming of particles less dense than water.

Chapter 10

Antifoaming agents in microgravity

10.1 Introduction

In chapter 4 we discussed different mechanisms of foam destruction by fast antifoams. All these mechanisms imply that the antifoaming globules act in the foam films. Based on this description we could imagine that in bubbly liquids ($\varepsilon \gtrsim 0.36$), where bubbles are not deformed and the films between bubbles does not exist, fast antifoams should be inefficient. Unfortunately, on Earth it is difficult to study bubbly liquids. They are not stable due to fast drainage in the gravity fields. However, the microgravity gives a unique opportunity to generate and study bubbly liquids and foams in the absence of drainage.

The stability of wet foams with antifoams was studied on the International Space Station within the frame of an educational program of ESA. The foams were made by an astronaut who shook manually the samples, hence the gas-liquid efficiency was very limited. As a consequence only very wet foams/bubbly liquids having negligible amounts of films were generated and investigated. An extraordinary stability of wet foams in the presence of the antifoaming agents was clearly shown in these experiments [108].

However, with this simple technique it was impossible to generate dry foams. Dry foams have a lot of films and, naively, we should expect that in the presence of antifoams they collapse in the microgravity as fast as on Earth. All mechanisms of foam destruction by fast antifoams described in Chapter 4 do not explicitly depend on gravity. To check this hypothesis and to explore a domain of sufficiently dry foams with antifoams the parabolic flight experiments were carried out.

In this chapter, we will see that dry foams with antifoams are surprisingly much more stable in microgravity than in 1 g. This is due to importance of antifoam globule transport step, which takes more time in μg .

10.2 Results and discussion

The parabolic flight technique allows us to perform short (about 22 s) experiments in microgravity conditions. During each period of microgravity we generate

foam for the first 10 s and then follow the foam stability during the next 12 s. Using the recorded videos, the relative foam volume F (ratio between the volume of the foam and the volume of the cell) is estimated as a function of time for foams having different liquid content (from 10 to 70 %). More details about the experimental set-up can be found in Chapter 5.

A typical $F(t)$ dependence for a dry foam is shown in Figure 10.1. The samples with no added antifoam foam very well and are stable for the duration of the experiments. The results also confirm that in 1g the antifoam is effective at breaking the foam both during foam generation and afterwards. In comparison, the antifoam in μg is still effective during generation, although less so than in 1g, but it is very ineffective after generation, which is unexpected. We will start to understand the observed behaviour by considering the role of gravity during the generation of the foam.

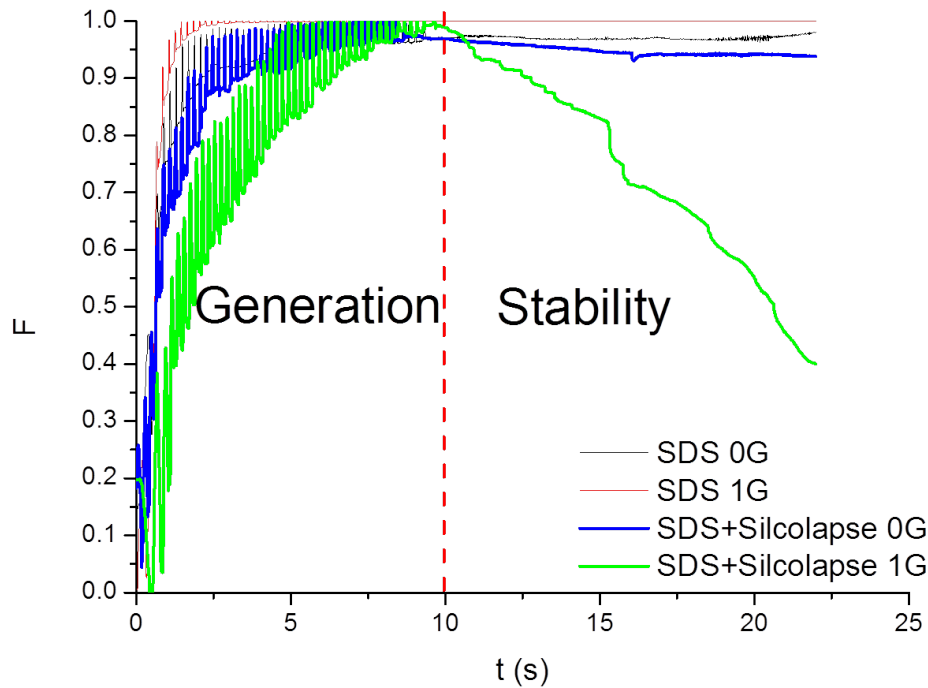


Figure 10.1: Relative foam volume F vs time for foam containing approximately 10 % of liquid after generation. A generation step, characterized by a big oscillation of the experimental data due the motor motion, is clearly seen.

Generation In Figure 10.2 one can see the average liquid fraction in the foam during the generation for the same samples as shown in Figure 10.1. The volume of foam generated increases just as fast for all the samples until an average liquid fraction of 0.36 is reached. At this point films start being formed in the foam and the antifoam breaks the foam slowing down the generation.

We can observe the same effect by measuring the average time taken to generate a foam for all the samples at different volume fractions (Figure 10.3). In our experiments the generation time t_{gen} is defined as a time necessary to fill 90 % of the cell by the foam. One can see that in the absence of the antifoam the generation time almost does not depend on the liquid fraction and is about 1 s, both in μg and in 1g. For foams with Silcolapse, the antifoam has no influence if the liquid fraction is above 0.36, however as the foam becomes drier the generation time increases. This confirms our expectation that fast antifoam can be effective only in the presence of films. With the decrease of the liquid fraction, the films becomes more important and the generation slows down. Interestingly we also see that for dry foams the extent to which the foam is destroyed during generation depends on gravity: the antifoam is more efficient during the generation in 1g than in μg .

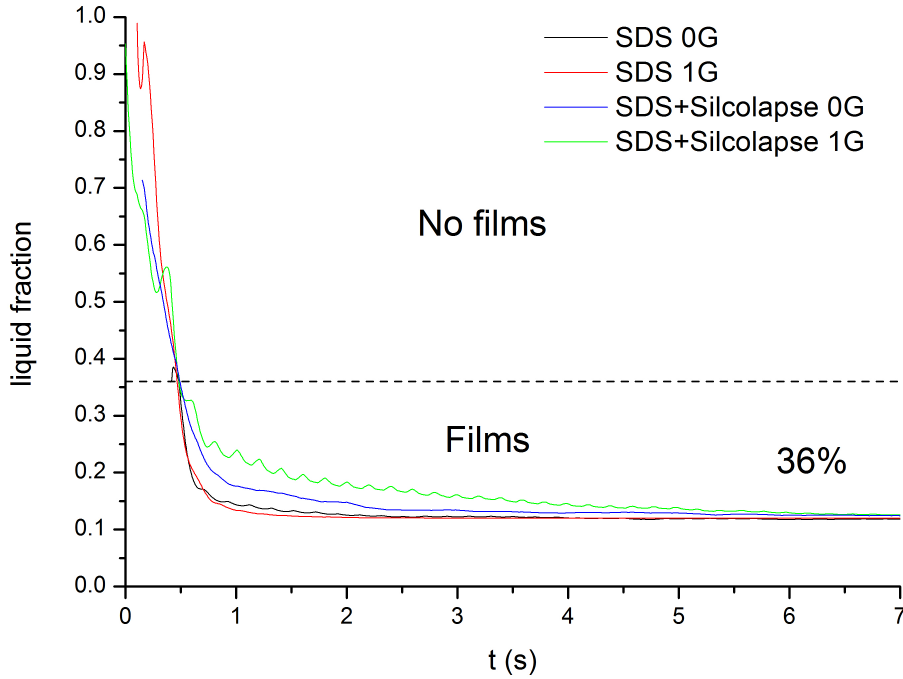


Figure 10.2: Liquid fraction vs time during generation for 10 % foam. Regions with and without films are shown.

It has been suggested that antifoams are more effective during generation because bubble surfaces are not fully covered by surfactants [64]. This should not depend on gravity and cannot be the sole reason why the antifoam is less efficient during generation in μg . Our foaming method is rather violent and the Froude number can be used to compare the role of gravity with that of inertia during generation

$$Fr = \frac{D_{osc}\nu^2}{g} \quad (10.1)$$

where D_{osc} and ν are the amplitude and the frequency of oscillations. In our case $D_{osc} = 5 \text{ cm}$ and $\nu = 5 \text{ Hz}$. This gives $Fr \approx 0.1$ meaning that vigorous foam

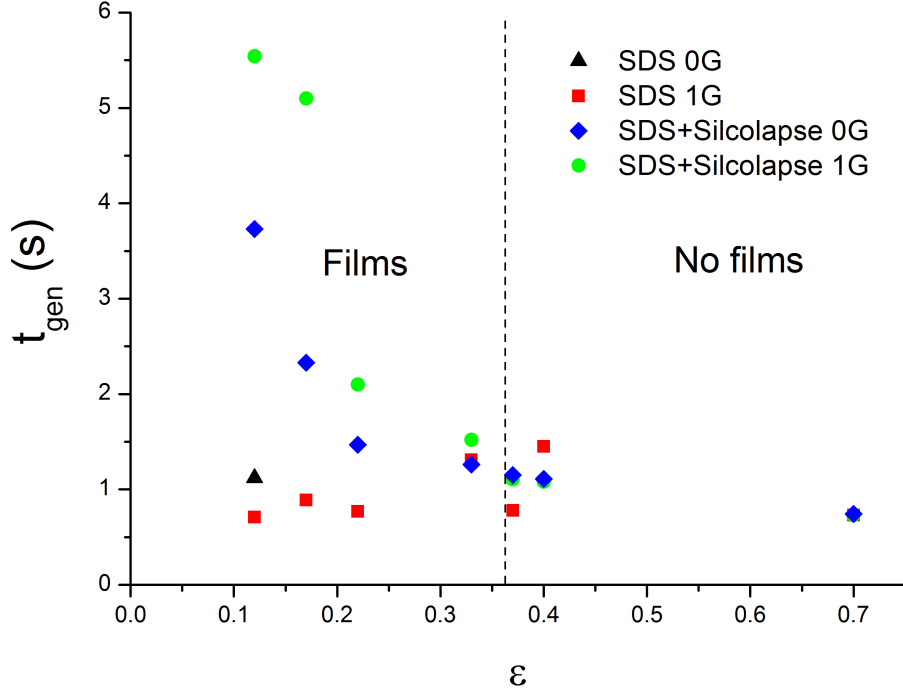


Figure 10.3: Foam generation time as a function of the final liquid fraction.

production is still rather weak in comparison with gravity. Antifoam is thus more effective in 1 g than in μg , as more films are formed at the top of the sample in 1 g because of gravity-driven drainage.

Stability We now turn our attention to the loss of antifoam activity after generation in μg . We can imagine that straight after generation the antifoam globules are evenly distributed throughout the foam. This means that some of them are found in films whilst others are in Plateau borders and nodes.

In μg once films are formed they thin because of the capillary pressure that sucks the liquid into the Plateau borders. Indeed, taking the radius of Plateau border as $R_{pb} \approx 10 \mu m$, the capillary pressure difference between the film and the adjacent plateau border is about 3000 Pa, which is much higher than hydrostatic pressure (less than 1 Pa), so film thinning should proceed in a very similar way in 1g and in μg . The antifoam globules in the films can either flow out with capillary pressure driven drainage, or they can stay and break the film as soon as it thins to a thickness comparable with their size. The time to drain to around $5 \mu m$ is a fraction of seconds. It means that in less than one second after the end of generation the antifoam should find themselves in Plateau borders, whether they have just broken a film or not.

To continue to be effective the antifoam now have to make their way back towards the films to break them. The particles move within the PBs because of drainage, sedimentation (antifoam density is not the same as water), and diffusion. We can

estimate the time it takes to cross a Plateau border (travel a distance of $10\ \mu m$) by means of each of these processes.

The permeability coefficient of SDS foam with $\varepsilon \approx 0.1$ is about $k \approx 10^{-5}$ [56]. In 1g, using Darcy's law 3.34 a typical drainage velocity for $100\ \mu m$ bubbles can be estimated as $10\ \mu m/s$, which gives the drainage time $t_{dr} \approx 1s$. The diameter of droplets d is about $5\ \mu m$, from which we calculate using Equation 3.19 a Stokes velocity of $0.4\ \mu m/s$ and the corresponding time of sedimentation $t_{sed} \approx 25s$. The characteristic time to diffuse the radius of a Plateau border R_{Pb} is $R_{Pb}^2/6D$, with the diffusion coefficient being $D = k_B T / (3\pi\mu d)$, which gives the diffusion time t_{diff} around 170 s. For the sake of clarity, all estimations are tabulated in the table 10.1. We see that drainage and sedimentation times are comparable with the time of experiment (12 s) and they are sufficiently fast to transport antifoam droplets, while the diffusion is too slow. Of course the fact that R_{Pb} decreases as the foam drains, further helps get the antifoam to the interfaces.

	1g	0.02g
t_{dr}	1 s	50 s
t_{sed}	25 s	1250 s
t_{diff}	170 s	170 s

Table 10.1: Characteristic times of drainage t_{dr} , sedimentation t_{sed} and diffusion t_{diff} in 1g and 0.02g.

In μg , drainage and buoyancy slow down by several orders of magnitude. In parabolic flight technique the gravity is not zero but rather oscillates around zero with the amplitude about 0.02g. We will take this level of gravity to estimate the minimal drainage and sedimentation times. The results of calculations are shown in the table 10.1. One can see that in μg all three mechanisms are not sufficiently fast to transport the antifoam toward the films to break the foam during the experimental time. This means that it is not sufficient to have an antifoam with low entry barrier P_c^{cr} to act efficiently, we also need to be able to transport the particles to the necks of the PBs leading to films.

During the generation, the oscillations of the motor produce a lot of motion, so the antifoam droplets can be easily transported from one film to another.

The obtained results can also help explain the mystery of the inefficiency of antifoam when the droplet size is below a few microns. In the last 20 years several proposals have been made to explain their inefficiency as the size decreases: P_c^{cr} increases when d decreases [109], the probability to trap an oil drop in the foam decreases [110] or buoyancy is no longer efficient to bring drops in the films [61]. We show that the arrest of sedimentation can help explain the observed behaviour.

10.3 Conclusion

In this chapter we highlight the importance of the transport step in the foam destruction by fast antifoams, which despite the extensive work carried out has been

largely neglected (except in [61]). We show that buoyancy has a significant role in the transport of antifoam globules. This result can also help explain why antifoams on Earth are inefficient when the drops are too small for buoyancy to work efficiently. As antifoams are used in many industrial processes (food processing, cosmetics, oil recovery, coatings...) the results have the potential to affect the handling of foamable liquids all over the world.

Chapter 11

General conclusion

This thesis work is focused on the studies on the gravity-driven flows in foams. In particular, two problems have been investigated: i) an influence of surface state on foam drainage during generation ii) sedimentation of microparticles confined in foams.

First of all, I have studied the surfactant adsorption dynamics. A solution of CTAB with 0.1 M of NaBr was used as a model system. Using the experimentally determined surface equation of state, the desorption of ionic surfactant with excess of salt has been studied. The measured desorption curves have been shown to be reasonably described by diffusion-limited model neglecting adsorption and desorption barriers. Foam generation usually induces a lot of convection accelerating surfactant transport in the bulk, so we can expect that for modelled system the surface tension can be always considered as being in equilibrium during generation. However, the kinetic of surfactant adsorption/desorption still can be important during foam ageing. For example, bubble coarsening results in the change of bubble surface area distribution, the big bubbles expands, the small ones shrink. We can reasonably expect that in this case the adsorption dynamic can play an important role.

The liquid fraction profile in rising foam has been studied using a classical model of foam drainage with Darcy's law. The pressure gradient includes both gravity and osmotic pressure, and through the permeability we account for the mobility of the interfaces using recent expressions obtained from forced drainage experiments. The model describes experimental data on systems with mobile interfaces very well. The results show that the liquid fraction depends very weakly on the ordering at the bottom of the foam and that in bidisperse bubble distributions the larger bubble sizes control the foam drainage. The model predicts higher liquid fractions if the interfaces are rigid. However, in the described experiments systems which behave as rigid in forced drainage, behave as mobile ones. This can be explained by considering that in rising foams the foam is always very wet at the bottom so that the Plateau borders are too big to produce a significant hydrodynamic resistance. As a result the Boussinesq number at the bottom is always relatively low both for mobile and rigid interfaces. The fast drainage at the bottom of the foam fixes the liquid flux leading to dryer foam than could have been expected. Through these results one can see once more that the concept of mobile or rigid interfaces should be treated with caution as it is not only dependent on the physical chemistry of the interfaces,

but also on the problem under consideration. Thus a system that behaves as rigid in one problem can behave as mobile in another.

Having studied some aspects of the influence of interfaces on foam generation, I have paid my attention to the gravity-driven flows in foamed emulsion and solid microparticle laden foams. These foams are complex systems, consisting of three bulk phases, which separate with time in a gravity field. To get a distribution of phases with height, the volume fractions of at least two of them should be determined experimentally at different positions in foam. The water fraction profile in foams is usually obtained from electrical conductivity measurements, while the content of air or non-conducting particle phase are difficult to measure separately. To simplify the system, I have focused on vertical quasi-2D foams, which are monolayers of bubbles squeezed between two plates. The local two-dimensional structure of quasi-2D foams can be directly observed and the image treatment can provide us with additional information about air content.

As far as I know, neither electrical conductivity nor detailed three-dimensional geometry of quasi-2D foams have never been studied systematically (except [23]). This is surprising, taking into account that quasi-2D foams are now widely used to access foam properties at the bubble scale and study different aspects of foam rheology, foam drainage, bubble coarsening and coalescence. In this thesis a model to describe the geometry of a quasi-2D foam was introduced, this description was used to model the electrical and flow conductivities of quasi-2D foams. The model was shown to describe well the accompanying experiments over a wide range of liquid fractions. In particular both electrical and flow conductivity measurements show that in the case of quasi-2D foams the liquid in the nodes needs to be taken into account even at low liquid content. The results may provide new approaches for the characterisation of foam properties and for the in-situ characterisation of the liquid content of foams in confining geometries, such as microfluidics. In future the described model can be applied to study foams with microparticles in quasi-2D configuration. The electrical conductivity can give information about the foaming solution fraction, while the image treatment gives a content of the aqueous and particle phases together. Using both techniques, the distribution of all phases can be calculated at different heights.

To imitate the particle movement in a single Plateau border, I have studied the particle sedimentation under confinement in circular capillaries. The sedimentation velocity have been studied for different confinement degrees expressed as a ratio between the capillary size D and the particle diameter d . It was shown that for a given particle volume fraction the decrease of capillary size results in sedimentation deceleration. For $D/d \geq 7$ the confinement effect can be explained by the presence of the excluded volume close to the walls. This excluded volume increases the effective particle fraction and therefore slows down the sedimentation as compared with bulk suspension. As D/d decreases the excluded volume effect becomes more pronounced and the velocity goes down. For $D/d \leq 7$ the excluded volume effect is not enough to explain the abrupt deceleration of sedimentation, the hydrodynamic interactions between the walls and the particles should be taken into account. An influence of the capillary inclination angle has been studied. It was shown that sedimentation velocity and sedimentation flux exhibit local maxima at $\theta \sim 20 - 40^\circ$. At high angles

$\theta > 70^\circ$ the sedimentation stops. Coming back to the foams, this result allows us to expect that the particles in foams should be arrested in horizontal or almost horizontal Plateau borders. I have also studied the development of perturbations in the plug configuration, where all particles are collected at the top of the capillary. It was shown that there exist two types of particle behaviour: solid-like and fluid-like. The former resembles the melting of the solid crystal, while the latter appears like a "classical" Rayleigh-Taylor instability at liquid/liquid interface.

Finally, by combining the knowledge of foam generation and particle transport in foams, the influence of gravity on the foam destruction by fast antifoams has been studied. To elucidate the role of gravity-induced flows, a foam with antifoaming agents was generated on Earth and in microgravity conditions obtained by parabolic flight technique. The experimental results show, for the first time, that gravity has a significant role in the transport of antifoam globules affecting their antifoaming activity. In microgravity, where buoyancy and gravitational drainage are strongly slowed down, diffusion leads to poor antifoam performance. The foam is stable for the duration of the experiment, whereas on Earth the foam starts to disappear immediately. Indeed, microgravity renders highly efficient antifoam practically useless. As antifoams are used in many industrial processes (food processing, cosmetics, oil recovery, coatings) the results have the potential to affect the handling of foamable liquids all over the world.

The main scope of this thesis was to show the importance of gravity-driven flows in foams, which was made using two examples: the drainage during the foam generation and foams with microparticles. The last now attract a significant scientific interest related to their importance in many industrial processes. In this thesis a base to microparticle-laden foam characterisation have been developed, some results in simplified systems has been obtained and accounted for. One can expect that in the nearest future these techniques will be applied to study real foamed emulsions and suspensions. At the same time the considered problems are important by their own and are potentially interest for various practical applications non-related directly with foams doped with microparticles.

Appendix A

Resumé substantiel de la thèse

A.1 Introduction

Les mousses liquides sont des dispersions de bulles dans l'eau et elles sont largement utilisées dans un grand nombre des applications industrielles. La grande quantité de surface par unité de volume dans les mousses fait qu'elles sont particulièrement attractive pour les opérations d'extraction et de séparation. L'exemple le plus connu est la flottation utilisée pour séparer les minéraux, comme le cuivre ou le plomb, de la gangue. La génération de la mousse est un moyen très efficace pour augmenter la viscosité du liquide de telle sorte que le système acquiert le comportement mécanique des matériaux solides. Cette propriété rend les mousses si attractives pour les produits cosmétiques et agroalimentaires. Une mousse suffisamment élastique coule lentement dans le champ de gravité et elle peut être utilisée pour couvrir des surfaces verticales, par exemple, dans les mousses à raser. La haute viscosité de mousses est utile pour déplacer le pétrole de milieux poreux dans la récupération assistée du pétrole. Comme le contenu de liquide dans les mousses peut être relativement faible, l'utilisation des mousses permet de réduire la quantité d'ingrédients actifs sans réduire leur effet. Cet effet est utilisé pour la décontamination, par exemple, les mousses de nettoyage sont largement exploitées dans le démantèlement d'installations nucléaires. Les mousses liquides peuvent être solidifiées pour obtenir des matériaux légers qui sont utilisés comme des excellents isolants thermiques et acoustiques.

Compte tenu de ces nombreuses applications le contrôle des propriétés des mousses, telles que la taille des bulles, la fraction de liquide, la contrainte de seuil, est nécessaire. Malheureusement, les mousses sont thermodynamiquement instables et se détruisent par des mécanismes divers de manière irréversible. Cela rend la génération de mousse stable avec les propriétés souhaitées une tâche extrêmement difficile. Parmi les différents effets déstabilisants, le drainage gravitationnel est l'un des plus importants. Le drainage induit l'écoulement de liquide contenu dans la mousse vers le bas et l'accumule dans la zone inférieure. La mousse sèche résultante est moins stable par rapport à d'autres mécanismes de déstabilisation, comme la coalescence, (la rupture d'un film entre deux bulles voisines) ou le mûrissement (le transfert de gaz entre bulles de tailles différentes en raison d'une différence de pression capillaire). La variation de contenu de liquide crée également des gradients de

propriétés optiques et mécaniques, qui sont souvent inacceptables dans des applications pratiques. Cela ne sera pas exagéré de dire que le ralentissement de drainage est une étape clé dans la production de mousses uniformes et stables.

L'exemple de drainage montre que la gravité joue un rôle très important dans les mousses. Ce travail de thèse se concentre sur deux problèmes concernant les écoulements gravitationnels dans les mousses: i) l'influence de l'état de surface sur le drainage de mousse lors de la génération ii) le transport des microparticules dans les mousses.

Tout d'abord, je m'intéresse à l'influence de l'état de surface sur le drainage de la mousse. La réponse mécanique de l'interface dépend de l'état chimique de l'interface et des coefficients cinétiques d'adsorption/désorption de tensioactifs. Je montre comment le changement de la mobilité de surface affecte la génération de mousse. Lors de la génération de mousse les interfaces fraîches sont constamment créées. Pour mieux comprendre comment cet effet-là peut influencer la mobilité de la mousse, j'étudie également la dynamique du peuplement de l'interface eau/air par des tensioactifs.

Une attention particulière est aussi accordée à la comportement hydrodynamique des mousses modifiées par la présence des particules micrométriques dans la phase liquide. Propriétés des mousses dopées avec des microparticules attirent maintenant un grand intérêt scientifique, les différents types de particules sont considérés: les particules solides et les gouttes d'huile potentiellement déformable à l'intérieur des mousses. La présence de particules augmente de manière significative la viscosité effective de liquide et peut stabiliser la mousse en ralentissant le drainage. Ces mousses ultra-stables sont maintenant largement utilisés dans l'industrie, par exemple dans les cosmétiques ou les produits alimentaires (comme la crème chantilly). En même temps, des émulsions d'huile de silicone ou des particules solides hydrophobes sont largement utilisées pour empêcher la formation des mousses indésirables, par exemple, dans la production du papier et de la peinture ou dans la récupération de pétrole. Les antimoussants utilisés dans l'industrie peuvent détruire d'énormes volumes de mousse en quelques secondes.

Ayant en général une densité différente de celle de l'eau, les particules migrent sous l'influence de la gravité. Dans le cas où les particules sont plus denses que l'eau ce processus s'appelle la sédimentation, tandis que pour les gouttes d'huile légères il se nomme le crémage. Ces écoulements gravitationnels influencent la redistribution des particules et modifient des propriétés du produit final.

Dans cette thèse, je considère essentiellement la sédimentation des particules dans les mousses, cependant, tous les résultats obtenus sont bien sûr valables pour le processus de crémage. On attend que le transport de particules dans des mousses est différent de la sédimentation d'une suspension en vrac. La mousse peut être considérée comme un réseau des canaux de liquide, ayant une taille caractéristique comparable avec le diamètre des particules. Donc les particules circulent dans une géométrie confinée, où l'influence des parois est important. Le couplage entre le drainage de la mousse et la sédimentation des particules doit aussi être pris en compte. En conséquence, en fonction de la formulation précise, les mélanges des particules et des bulles peuvent se séparer en quelques secondes ou être stable pendant des jours.

Pour étudier une distribution de particules dans les mousses j'ai choisi d'utiliser les mousses pseudo-bidimensionnelles verticales (les monocouches des bulles serrées entre deux plaques solides). Dans ma thèse, je montre comment la structure des mousses pseudo-bidimensionnelles peut être étudiée par des mesures de conductivité électrique et de traitement d'image. A l'avenir, les résultats obtenus peuvent potentiellement être appliqués à l'étude des mousses avec des microparticules.

A.2 Contexte de la thèse

La partie **I** de cette thèse présente une base théorique nécessaire pour comprendre les résultats expérimentaux. Cette partie se compose de 4 chapitres et représente différents aspects de la thermodynamique des surfaces, la structure des mousses à l'équilibre, l'hydrodynamique de sédimentation des particules et le drainage de la mousse, les propriétés des agents antimoussant.

La préparation des échantillons expérimentaux et la description des techniques expérimentales sont détaillées dans la partie **II**.

La partie **III** se compose de cinq chapitres discutants les résultats expérimentaux obtenus sur différents problèmes étudiés dans cette thèse.

Dynamique de désorption des tensioactifs aux interfaces liquide/air. Le chapitre 6 présente une étude de la dynamique d'adsorption et de désorption des tensioactifs aux interfaces liquide/air étudiés par une mesure de tension superficielle. Une solution de CTAB avec 0,1 M de NaBr est utilisée comme un système modèle. En utilisant l'équation d'état de la surface déterminée expérimentalement, la désorption de tensioactif ionique avec un excès de sel est étudiée. Les courbes de concentration surfacique peuvent être raisonnablement décrits par un modèle qui prend en compte que la diffusion de tensioactif et néglige des barrières d'adsorption et de désorption (voire figure A.1).

La génération de mousse induit généralement beaucoup de convection accélérant le transport tensioactif dans la volume. Nous pouvons nous attendre pour le système modélisé que la tension superficielle est toujours en équilibre lors de la génération. Cependant, la dynamique d'adsorption et de désorption est importante pour la vieillissement de la mousse. Par exemple, le murissement des bulles résulte dans un changement de la distribution de surface des bulles, les grosses bulles se dilatent, les petits se compriment. Nous pouvons raisonnablement espérer que, dans ce cas, la dynamique d'adsorption peut jouer un rôle important.

La génération des mousses en ascension par bullage. Dans le chapitre 7 le profil stationnaire de fraction liquide dans une mousse en ascension est étudié en utilisant un modèle classique de drainage de la mousse avec la loi de Darcy. Le gradient de pression inclut la gravité et la pression osmotique, et à travers la perméabilité je prend en compte la mobilité des interfaces en utilisant des expressions obtenus récemment à partir d'expériences de drainage forcés. Le modèle décrit les données expérimentales très bien pour les systèmes avec des interfaces mobiles. Les résultats montrent que la fraction de liquide dépend très peu de la mousse.

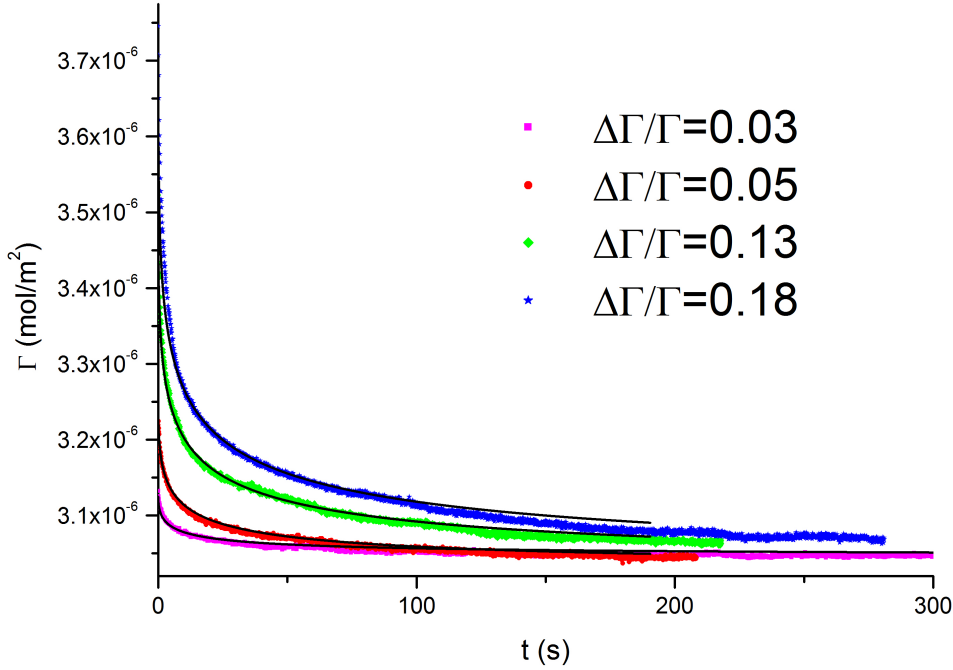


Figure A.1: La variation de la concentration de surface après une compression rapide pour différents degrés de compression. Les lignes noires indiquent les prédictions théoriques avec la coefficient de diffusion $D \approx 6 \cdot 10^{-6} \text{ m}^2/\text{s}$.

Le modèle prédit des fractions de liquide plus élevés si les interfaces sont rigides. Cependant, dans nos expériences les systèmes qui se comportent comme rigides dans les expériences de drainage forcé, se comportent tous comme les mobiles (Figure A.2).

Ceci peut être expliqué en considérant que dans la zone inférieure la mousse est toujours très humide et les bords de Plateau sont trop gros pour produire une résistance hydrodynamique significative. En conséquence, le nombre de Boussinesq au fond est toujours relativement faible pour les deux interfaces mobiles et rigides. Le drainage rapide au bas de la mousse fixe le courant de liquide conduisant à une mousse sèche. Grâce à ces résultats, nous voyons encore une fois que le concept des interfaces mobiles et rigides doit être traité avec prudence, car le comportement du système ne dépend pas seulement de la physicochimie des interfaces, mais aussi sur le problème hydrodynamique à l'étude. Ainsi donc, un système qui se comporte comme rigide dans un problème peut se comporter comme mobile dans un autre.

Les conductivités électriques et hydrodynamiques des mousses pseudo-bidimensionnelles. Ayant étudié certains aspects de l'influence des interfaces sur la génération de la mousse, j'ai fait attention sur les écoulement gravitationnelle dans les mousses chargées par des microparticules. Ces mousses sont des systèmes com-

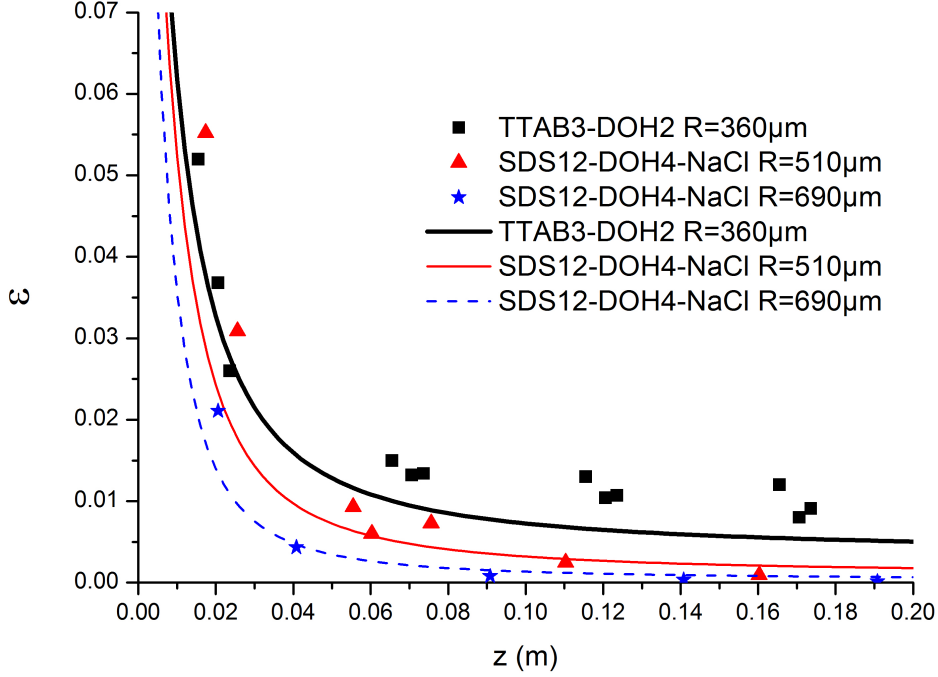


Figure A.2: Profils de fraction liquide pour les systèmes qui se comportent comme rigides dans le drainage forcé. Les lignes montrent des profils théorique calculés dans la limite rigide.

plexes et composent de trois phases qui séparent avec le temps dans un champ de gravité. Pour obtenir une distribution de phases avec hauteur, les fractions volumiques d'au moins deux d'entre eux devraient être déterminées expérimentalement à différentes positions dans la mousse. Le profil de fraction d'eau dans les mousses est généralement obtenu à partir des mesures de conductivité électrique, tandis que les teneurs de l'air et de la phase de particules non-conducteurs sont difficiles à mesurer séparément. Pour simplifier le système, je concentre sur les mousses pseudo-bidimensionnelles verticales, qui sont des monocouches de bulles serrées entre deux plaques. La structure locale de mousses pseudo-bidimensionnelles peut être directement observée et le traitement de l'image peut nous fournir des informations supplémentaires sur le contenu de l'air.

Pour autant que je sache, ni la conductivité électrique, ni la géométrie détaillée tridimensionnelle de mousses pseudo-bidimensionnelles ont jamais été étudiée de manière systématique (sauf [23]). Cela est surprenant, en tenant compte du fait que les mousses pseudo-bidimensionnelles sont maintenant largement utilisées pour accéder aux propriétés de la mousse à l'échelle de la bulle et étudier les différents aspects de rhéologie des mousses, de drainage, de murissement et de coalescence des bulles. Dans le chapitre 8 un modèle pour décrire la géométrie d'une mousse pseudo-bidimensionnelles est introduit, cette description est utilisée pour modéliser

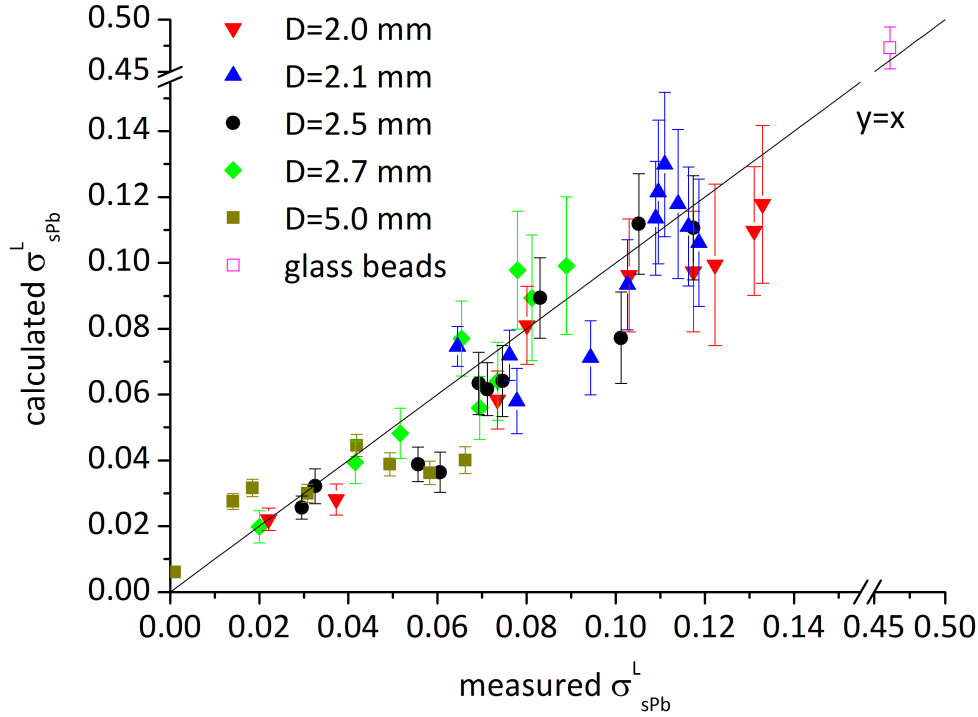


Figure A.3: La conductivité électriques théoriques vs les valeurs mesurées expérimentalement pour les tailles des bulles différentes D .

les conductivité électrique et le drainage forcé des mousses pseudo-bidimensionnelles. Le modèle présenté décrit bien les expériences accompagnant sur une large gamme de fractions liquides (Figure A.3). Les résultats peuvent fournir de nouvelles approches pour la caractérisation des propriétés de la mousse et pour la caractérisation in situ de la teneur en liquide de mousses dans des géométries confinées, comme dans la microfluidique. Dans l'avenir, le modèle présenté peut être appliqué à l'étude des mousses avec des microparticules dans la configuration pseudo-bidimensionnelles. La conductivité électrique peut donner des informations sur la fraction liquide de la mousse, tandis que le traitement d'image donne une teneur des phases aqueuse et de particules ensemble. En utilisant ces deux techniques, la distribution de toutes les phases peut être calculé à des hauteurs différentes.

La sédimentation des microparticules dans un milieu confiné. Pour imiter le mouvement des particules dans un bord de Plateau, j'étudie la sédimentation des particules confinées dans les capillaires circulaires. Dans le chapitre 9 la vitesse de sédimentation est étudiées pour différents degrés de la confinement exprimés comme le rapport entre la taille de capillaire D et le diamètre des particules d . Les résultats montrent que la vitesse de sédimentation augmente avec D/d (Figure A.4). Pour $D/d \geq 7$ l'effet de confinement peut être expliqué par la présence du volume exclu près des murs. Le volume exclu augmente la fraction des particules effective et

ralentit la sédimentation en comparaison avec une suspension non confiné. Quand D/d diminue l'effet de volume exclu devient plus prononcée et la vitesse descend. Pour $D/d \leq 7$ l'effet de volume exclu ne suffit pas à expliquer la brusque décélération de la sédimentation, les interactions hydrodynamiques entre les murs et les particules doivent être prises en compte.

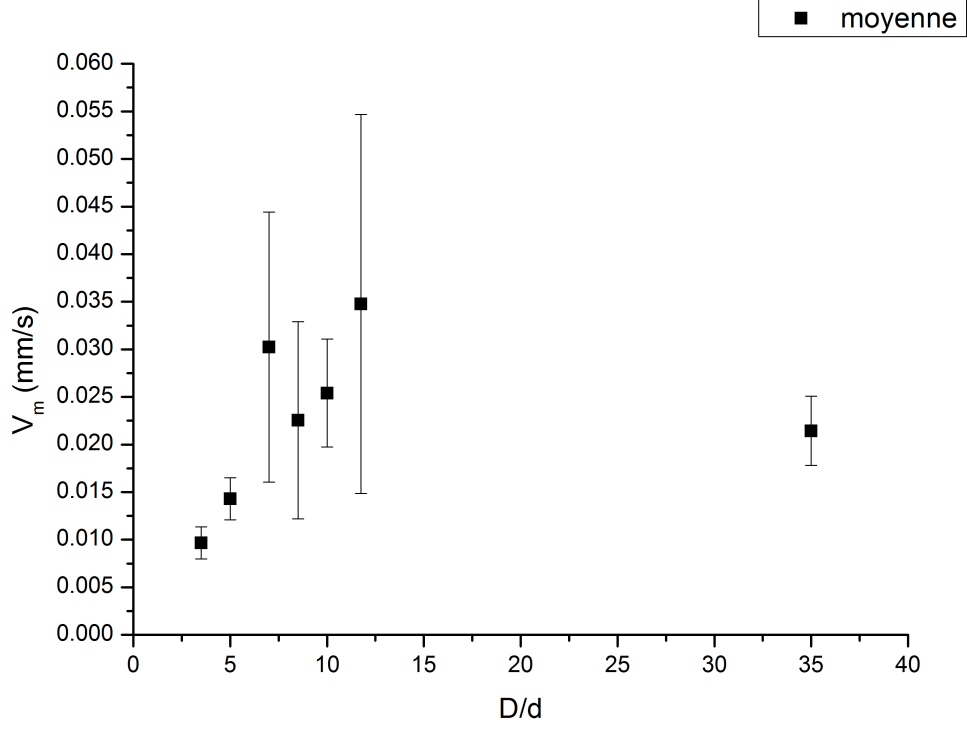


Figure A.4: La vitesse de sédimentation vs le degré de la confinement D/d .

Une influence de l'angle d'inclinaison du capillaire est aussi étudiée. La vitesse de sédimentation et le débit volumique par unité de surface présentent des maxima locaux vers $\theta \sim 20 - 40^\circ$. Aux plus grandes angles $\theta > 70^\circ$ la sédimentation s'arrête. J'étudie également le développement des perturbations dans la configuration du bouchon, où toutes les particules sont initialement accumuler en haut du capillaire. Les résultats montrent qu'il existe deux types de comportement des particules: solide et fluide (Figure A.5). L'ancien ressemble à la fonte du solide, tandis que le second apparaît comme une instabilité "classique" de Rayleigh-Taylor à l'interface liquide/liquide.

Les agents antimoissants en microgravité. Enfin, en combinant la connaissance de la production de mousse et de transport de particules dans des mousses, l'influence de la gravité sur la destruction de la mousse par des agents antimoissants rapides est étudiée dans le chapitre 10. Pour élucider le rôle des écoulements induits par la gravité, une mousse avec des agents antimoissants a été généré sur Terre et dans des conditions de microgravité obtenus par la technique du vol parabolique. Les

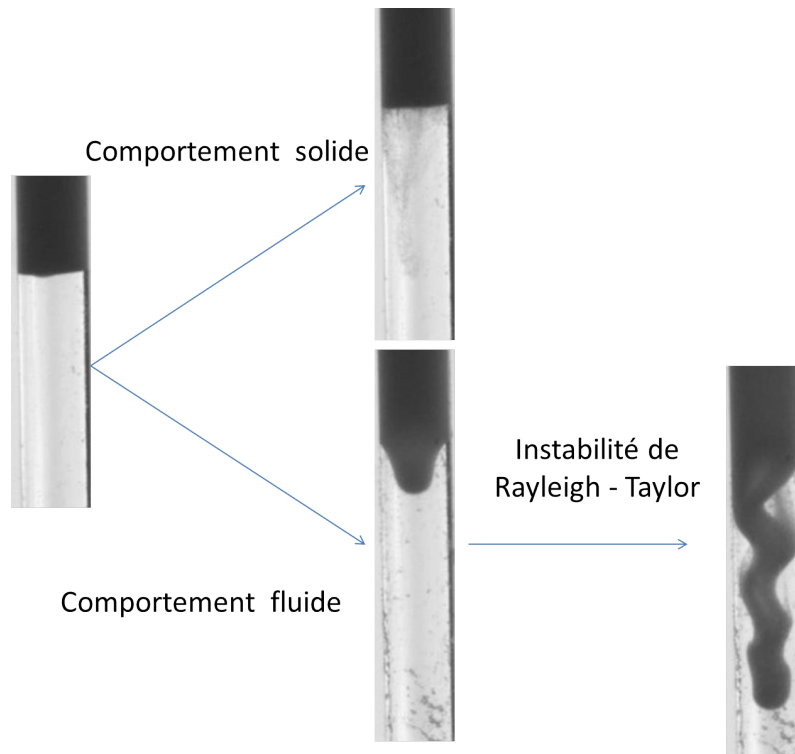


Figure A.5: Différents types de départ des particules.

résultats expérimentaux montrent, pour la première fois, que la gravité joue un rôle important dans le transport des globules antimoussant et influence leur activité. En microgravité, où la flottabilité et le drainage gravitationnel sont fortement ralenties, la diffusion conduit à une pauvre performance de l'antimousse. Les mousses sont stables pendant la durée de l'expérience, alors que sur Terre les mousses commencent à disparaître immédiatement. En effet, la microgravité rend les antimousses très efficaces pratiquement inutiles. Comme les agents antimoussants sont utilisés dans de nombreux procédés industriels (production des aliments, des cosmétiques, la récupération du pétrole) les résultats ont le potentiel d'affecter la manipulation des liquides moussants partout dans le monde.

Le but principale de cette thèse est de montrer l'importance des écoulements gravitationnels dans les mousses à l'aide de deux exemples: le drainage lors de la génération de la mousse et des mousses avec des microparticules. Ce dernier point attire actuellement un grand intérêt dans de nombreux procédés industriels. Dans cette thèse, une base pour la caractérisation des mousses chargées des microparticules est développée, certains résultats dans des systèmes simplifiés sont obtenus et interprétés. Différents types de particules sont pris en compte: les particules solides et les gouttes d'huile qui peuvent être déformés à l'intérieur des mousses. On peut penser que dans l'avenir proche ces techniques seront appliquées pour étudier les émulsions et les suspensions des mousses réelles. Dans le même temps les problèmes considérés sont importants par eux-mêmes et sont potentiellement intéressant pour diverses applications pratiques non liées directement avec des mousses dopées par

des microparticules.

Bibliography

- [1] K. G. Baikerikar and R. S. Hansen. Inference of surface excess and its high activity limit in monolayer adsorption from interfacial tension and activity data. *Langmuir*, 7(9):1963–1968, 1991.
- [2] D. F. Evans and H. Wennerström. *The colloidal domain: Where physics, chemistry, biology, and technology meet*. Wiley-VCH, New York, 1994.
- [3] P. A. Kralchevsky, K. D. Danov, G. Broze, and A. Mehreteab. Thermodynamics of ionic surfactant adsorption with account for the counterion binding: Effect of salts of various valency. *Langmuir*, 15(7):2351–2365, 1999.
- [4] A. J. Prosser and E. I. Franses. Adsorption and surface tension of ionic surfactants at the air-water interface: review and evaluation of equilibrium models. *Colloids Surf. A Physicochem. Eng. Asp.*, 178(1-3):1 – 40, 2001.
- [5] J. Eastoe and J. S. Dalton. Dynamic surface tension and adsorption mechanisms of surfactants at the air-water interface. *Adv. Colloid Interface Sci.*, 85(2-3):103 – 144, 2000.
- [6] C. J. Radke. Gibbs adsorption equation for planar fluid-fluid interfaces: Invariant formalism. *Adv. Colloid Interface Sci.*, 2014.
- [7] C.-H. Chang and E. I. Franses. Adsorption dynamics of surfactants at the air/water interface: a critical review of mathematical models, data, and mechanisms. *Colloids Surf. A Physicochem. Eng. Asp.*, 100:1 – 45, 1995.
- [8] A. F. H. Ward and L. Tordai. Time dependence of boundary tensions of solutions i. the role of diffusion in time effects. *J. Chem. Phys.*, 14(7):453–461, 1946.
- [9] S. Y. Lin, K. McKeigue, and C. Maldarelli. Diffusion-controlled surfactant adsorption studied by pendant drop digitization. *AIChE J.*, 36(12):1785–1795, 1990.
- [10] X. Li, R. Shaw, G. M. Evans, and P. Stevenson. A simple numerical solution to the ward-tordai equation for the adsorption of non-ionic surfactants. *Comput. Chem. Eng.*, 34(2):146 – 153, 2010.
- [11] H. Diamant and D. Andelman. Kinetics of surfactant adsorption at fluid-fluid interfaces. *J. Phys. Chem.*, 100(32):13732–13742, 1996.

- [12] H. Diamant, G. Ariel, and D. Andelman. Kinetics of surfactant adsorption: the free energy approach. *Colloids Surf. A Physicochem. Eng. Asp.*, 183-185:259 – 276, 2001.
- [13] D. Langevin. Influence of interfacial rheology on foam and emulsion properties. *Adv. Colloid Interface Sci.*, 88(1-2):209 – 222, 2000.
- [14] L. Liggieri R. Millett, editor. *Interfacial rheology*. Brill, 2009.
- [15] R. Miller, J. K. Ferri, A. Javadi, J. Krägel, N. Mucic, and R. Wustneck. Rheology of interfacial layers. *Colloid Polym. Sci.*, 288(9):937–950, 2010.
- [16] I. Cantat, S. Cohen-Addad, F. Elias, F. Graner, R. Höhler, O. Pitois, F. Rouyer, and A. Saint-Jalmes. *Foams: structure and dynamics*. Oxford University Press, 2013.
- [17] W. Drenckhan and S. Hutzler. Structure and energy of liquid foams. *Adv. Colloid Interface Sci.*, 2015.
- [18] D. Weaire and R. Phelan. A counter-example to kelvin’s conjecture on minimal surfaces. *Philos. Mag. Lett.*, 69(2):107–110, 1994.
- [19] S. A. Koehler, S. Hilgenfeldt, and H. A. Stone. A generalized view of foam drainage: Experiment and theory. *Langmuir*, 16(15):6327–6341, 2000.
- [20] S. J. Neethling, H. T. Lee, and J. J. Cilliers. A foam drainage equation generalized for all liquid contents. *J. Phys.: Condens. Matter*, 14(3):331–342, 2002.
- [21] T. C. Hales. A proof of the kepler conjecture. *Ann. Math.*, 162(3):1065–1185, 2005.
- [22] S. J. Cox and E. Janiaud. On the structure of quasi-two-dimensional foams. *Philos. Mag. Lett.*, 88(9-10):693–701, 2008.
- [23] C. Gay, P. Rognon, D. Reinelt, and F. Molino. Rapid plateau border size variations expected in three simple experiments on 2d liquid foams. *EPJ E*, 34(1):2, 2011.
- [24] H. M. Princen. Rheology of foams and highly concentrated emulsions: I. elastic properties and yield stress of a cylindrical model system. *J. Colloid Interface Sci.*, 91(1):160 – 175, 1983.
- [25] S. A. Khan and R. C. Armstrong. Rheology of foams: I. theory for dry foams. *J. Nonnewton. Fluid Mech.*, 22(1):1 – 22, 1986.
- [26] S. Cox, D. Weaire, and J. A. Glazier. The rheology of two-dimensional foams. *Rheol. Acta*, 43(5):442–448, 2004.
- [27] C. Raufaste, A. Foulon, and B. Dollet. Dissipation in quasi-two-dimensional flowing foams. *Phys. Fluids*, 21(5):053102, 2009.

- [28] S. Costa, S. Cohen-Addad, A. Salonen, and R. Höhler. The dissipative rheology of bubble monolayers. *Soft Matter*, 9:886–895, 2013.
- [29] J. A. Glazier, S. P. Gross, and J. Stavans. Dynamics of two dimensional soap froths. *Phys. Rev. A*, 36(1):306–312, 1987.
- [30] J. Stavans. Evolution of two-dimensional cellular structures: The soap froth. *Physica A*, 194:307 – 314, 1993.
- [31] A. E. Roth, C. D. Jones, and D. J. Durian. Bubble statistics and coarsening dynamics for quasi-two-dimensional foams with increasing liquid content. *Phys. Rev. E*, 87(4), 2013.
- [32] J. Duplat, B. Bossa, and E. Villiermaux. On two-dimensional foam ageing. *J. Fluid Mech.*, 673:147–179, 2011.
- [33] G. K. Batchelor. Sedimentation in a dilute dispersion of spheres. *J. Fluid Mech.*, 52:245, 1972.
- [34] J. F. Richardson and W. N. Zaki. The sedimentation of a suspension of uniform spheres under conditions of viscous flow. *Chem. Eng. Sci.*, 3(2):65–73, 1954.
- [35] R. D. Felice. The sedimentation velocity of dilute suspensions of nearly mono-sized spheres. *Int. J. Multiphase Flow*, 25(4):559 – 574, 1999.
- [36] S. Koo. Estimation of hindered settling velocity of suspensions. *J. Ind. Eng. Chem.*, 15(1):45 – 49, 2009.
- [37] H. Nicolai, B. Herzhaft, E. J. Hinch, L. Oger, and E. Guazzelli. Particle velocity fluctuations and hydrodynamic self-diffusion of sedimenting non-brownian spheres. *Phys. Fluids*, 7(1):12–23, 1995.
- [38] E. Guazzelli and J. F. Morris. *A physical introduction to suspension Dynamics*. Cambridge University Press, 2012.
- [39] E. Guazzelli and J. Hinch. Fluctuations and instability in sedimentation. *Annu. Rev. Fluid Mech.*, 43(1):97–116, 2011.
- [40] E. J. Hinch. Sedimentation of small particles. In Etienne Guyon, Jean-Pierre Nadal, and Yves Pomeau, editors, *Disorder and Mixing*, volume 152 of *NATO ASI Series*, pages 153–162. Springer Netherlands, 1988.
- [41] E. Guazzelli. Evolution of particle-velocity correlations in sedimentation. *Phys. Fluids*, 13(6):1537–1540, 2001.
- [42] D. C. Gomez, L. Bergougnoux, E. Guazzelli, and J. Hinch. Fluctuations and stratification in sedimentation of dilute suspensions of spheres. *Phys. Fluids*, 21:093304, 2009.
- [43] P. Segrè, E. Herbolzheimer, and P. Chaikin. Long-range correlations in sedimentation. *Phys. Rev. Lett.*, 79:2574 – 2577, 1997.

- [44] A. E. Boycott. Sedimentation of blood corpuscles. *Nature*, 104:532, 1920.
- [45] A. Acrivos and E. Herbolzheimer. Enhanced sedimentation in settling tanks with inclined walls. *J. Fluid Mech.*, 92:435–457, 1979.
- [46] E. Ponder. On sedimentation and rouleaux formation. *Q. J. Exp. Physiol.*, 15(3):235 – 252, 1925.
- [47] H. Nakamura and K. Kuroda. La cause de l’accélération de la vitesse de sédimentation des suspensions dans les récipients inclinés. *Keijo J. Med*, 8:256–296, 1937.
- [48] C. P. Royall, J. Dzubiella, M. Schmidt, and A. van Blaaderen. Nonequilibrium sedimentation of colloids on the particle scale. *Phys. Rev. Lett.*, 98:188304, 2007.
- [49] A. Wysocki, C. P. Royall, R. G. Winkler, G. Gompfer, H. Tanaka, A. van Blaaderen, and H. Lowen. Direct observation of hydrodynamic instabilities in a driven non-uniform colloidal dispersion. *Soft Matter*, 5(7):1340 – 1344, 2009.
- [50] H. Darcy. *Les fontaines publiques de la ville de Dijon*. V. Damont, Paris, 1856.
- [51] H. M. Princen and A. D. Kiss. Osmotic pressure of foams and highly concentrated emulsions 2: Determination from the variation in volume fraction with height in an equilibrated column. *Langmuir*, 3(1):36–41, 1987.
- [52] D. Weaire and S. Hutzler. *The Physics of Foams*. Clarendon press, Oxford, 2005.
- [53] R. Höhler, Y. Yip Cheung Sang, E. Lorenceau, and S. Cohen-Addad. Osmotic pressure and structures of monodisperse ordered foam. *Langmuir*, 24(2):418–425, 2008.
- [54] A. Maestro, W. Drenckhan, E. Rio, and R. Höhler. Liquid dispersions under gravity: volume fraction profile and osmotic pressure. *Soft Matter*, 9:2531–2540, 2013.
- [55] S. A. Koehler, S. Hilgenfeldt, and H. A. Stone. Foam drainage on the microscale: Modeling flow through single plateau borders. *J. Colloid Interface Sci.*, 276(2):420 – 438, 2004.
- [56] E. Lorenceau, N. Louvet, F. Rouyer, and O. Pitois. Permeability of aqueous foams. *EPJ E*, 28(3):293–304, 2009.
- [57] A. Saint-Jalmes. Physical chemistry in foam drainage and coarsening. *Soft Matter*, 2(10):836–849, 2006.
- [58] P. Stevenson. *Foam Engineering: Fundamentals and Applications*. Wiley, 2012.

- [59] S. A. Koehler, S. Hilgenfeldt, and H. A. Stone. Liquid flow through aqueous foams: The node-dominated foam drainage equation. *Phys. Rev. Lett.*, 82(21):4232–4235, 1999.
- [60] F. Rouyer, O. Pitois, E. Lorenceau, and N. Louvet. Permeability of a bubble assembly: From the very dry to the wet limit. *Phys. Fluids*, 22(4), 2010.
- [61] V. Bergeron, P. Cooper, C. Fischer, J. Giermanska-Kahn, D. Langevin, and A. Pouchelon. Polydimethylsiloxane (pdms)-based antifoams. *Colloids Surf. A Physicochem. Eng. Asp.*, 122:103 – 120, 1997.
- [62] N. D. Denkov. Mechanisms of foam destruction by oil-based antifoams. *Langmuir*, 20(22):9463–9505, 2004.
- [63] C. A. Miller. Antifoaming in aqueous foams. *Curr. Opin. Colloid Interface Sci.*, 13(3):177 – 182, 2008.
- [64] N. D. Denkov, K. G. Marinova, and S. S. Tcholakova. Mechanistic understanding of the modes of action of foam control agents. *Adv. Colloid Interface Sci.*, 206:57 – 67, 2014.
- [65] P. R. Garrett. Defoaming: Antifoams and mechanical methods. *Curr. Opin. Colloid Interface Sci.*, 20(2):81 – 91, 2015.
- [66] P. R. Garrett. Preliminary considerations concerning the stability of a liquid heterogeneity in a plane-parallel liquid film. *J. Colloid Interface Sci.*, 76(2):587 – 590, 1980.
- [67] K. Feitosa, S. Marze, A. Saint-Jalmes, and D. J. Durian. Electrical conductivity of dispersions: from dry foams to dilute suspensions. *J. Phys.: Condens. Matter*, 17(41):6301–6305, 2005.
- [68] S. Mukherjee and H. Wiedersich. Morphological and viscoelastic properties of dense foams generated from skin cleansing bars. *Colloids Surf. A Physicochem. Eng. Asp.*, 95:159 – 172, 1995.
- [69] W. Drenckhan and A. Saint-Jalmes. The science of foaming. *Adv. Colloid Interface Sci.*, 222:228–259, 2015.
- [70] S.-H. Hsu, W.-H. Lee, Y.-M. Yang, C.-H. Chang, and J.-R. Maa. Bubble formation at an orifice in surfactant solutions under constant-flow conditions. *Ind. Eng. Chem. Res.*, 39(5):1473–1479, 2000.
- [71] A. Salonen, R. Lhermerout, E. Rio, D. Langevin, and A. Saint-Jalmes. Dual gas and oil dispersions in water: production and stability of foamulsion. *Soft Matter*, 8:699–706, 2012.
- [72] R. Pan, J. Green, and C. Maldarelli. Theory and experiment on the measurement of kinetic rate constants for surfactant exchange at an air/water interface. *J. Colloid Interface Sci.*, 205(2):213 – 230, 1998.

- [73] Y. He, Y. Shang, H. Liu, D. Langevin, and A. Salonen. Surfactant adsorption onto interfaces: Measuring the surface excess in time. *Langmuir*, 28(6):3146–3151, 2012.
- [74] Y. He, P. Yazhgur, A. Salonen, and D. Langevin. Adsorption-desorption kinetics of surfactants at liquid surfaces. *Adv. Colloid Interface Sci.*, 222:377 – 384, 2015. Reinhard Miller, Honorary Issue.
- [75] C. D. Taylor, D. S. Valkovska, and C. D. Bain. A simple and rapid method for the determination of the surface equations of state and adsorption isotherms for efficient surfactants. *Phys. Chem. Chem. Phys.*, 5:4885–4891, 2003.
- [76] S. Y. Lin, K. McKeigue, and C. Maldarelli. Diffusion-limited interpretation of the induction period in the relaxation in surface tension due to the adsorption of straight chain, small polar group surfactants: theory and experiment. *Langmuir*, 7(6):1055–1066, 1991.
- [77] Y.-C. Lee, K. J. Stebe, H.-S. Liu, and S.-Y. Lin. Adsorption and desorption kinetics of cme8 on impulsively expanded or compressed air-water interfaces. *Colloids Surf. A Physicochem. Eng. Asp.*, 220:139 – 150, 2003.
- [78] Y. Jayalakshmi, L. Ozanne, and D. Langevin. Viscoelasticity of surfactant monolayers. *J. Colloid Interface Sci.*, 170(2):358 – 366, 1995.
- [79] Y. Jayalakshmi and D. Langevin. Surface tension and viscoelasticity of alkane solubilized surfactant monolayers. *J. Colloid Interface Sci.*, 194(1):22 – 30, 1997.
- [80] A. M. Ganan-Calvo. Perfectly monodisperse microbubbling by capillary flow focusing: An alternate physical description and universal scaling. *Phys. Rev. E*, 69:027301, 2004.
- [81] A. A. Kulkarni and J. B. Joshi. Bubble formation and bubble rise velocity in gas-liquid systems: A review. *Ind. Eng. Chem. Res.*, 44(16):5873–5931, 2005.
- [82] S. J. Neethling, H. T. Lee, and J. J. Cilliers. The recovery of liquid from flowing foams. *J. Phys.: Condens. Matter*, 15(10):1563, 2003.
- [83] P. Stevenson. The wetness of a rising foam. *Ind. Eng. Chem. Res.*, 45(2):803–807, 2006.
- [84] P. Stevenson. Hydrodynamic theory of rising foam. *Miner. Eng.*, 20(3):282 – 289, 2007.
- [85] S. Hutzler, D. Losch, E. Carey, D. Weaire, M. Hloucha, and C. Stubenrauch. Evaluation of a steady-state test of foam stability. *Philos. Mag.*, 91(4):537–552, 2011.
- [86] S. Hutzler, S. T. Tobin, A. J. Meagher, A. Marguerite, and D. Weaire. A model system for foam fractionation. *Proc. R. Soc. A*, 469(2154):20120727, 2013.

- [87] K. Feitosa and D. J. Durian. Gas and liquid transport in steady-state aqueous foam. *EPJ E*, 26(3):309–316, 2008.
- [88] P. Stevenson and C. Stevanov. Effect of rheology and interfacial rigidity on liquid recovery from rising froth. *Ind. Eng. Chem. Res.*, 43(19):6187–6194, 2004.
- [89] P. Stevenson, C. Stevanov, and G. J. Jameson. Liquid overflow from a column of rising aqueous froth. *Miner. Eng.*, 16(11):1045 – 1053, 2003.
- [90] A. Saint-Jalmes, M. U. Vera, and D. J. Durian. Uniform foam production by turbulent mixing: new results on free drainage vs. liquid content. *EPJ B*, 12(1):67–73, 1999.
- [91] K. Koczó, L. A. Lobo, and D. T. Wasan. Effect of oil on foam stability: Aqueous foams stabilized by emulsions. *J. Colloid Interface Sci.*, 150(2):492 – 506, 1992.
- [92] Y.-L. Yan, C. Shan, Y. Wang, and Q. Deng. Effects of oil on aqueous foams: Electrical conductivity of foamed emulsions. *ChemPhysChem*, 15(14):3110 – 3115, 2014.
- [93] R. Lemlich. A theory for the limiting conductivity of polyhedral foam at low density. *J. Colloid Interface Sci.*, 64(1):107–110, 1978.
- [94] M. Durand, J.-F. Sadoc, and D. Weaire. Maximum electrical conductivity of a network of uniform wires: the lemlich law as an upper bound. *Proc. R. Soc. A*, 460(2045):1269–1284, 2004.
- [95] J.C. Maxwell. *Electricity and Magnetism*, volume 1. Clarendon press, Oxford, 1873.
- [96] R. Lemlich. Semitheoretical equation to relate conductivity to volumetric foam density. *Ind. Eng. Chem. Process Des. Dev.*, 24(3):686–687, 1985.
- [97] P. Yazhgur, C. Honorez, W. Drenckhan, D. Langevin, and A. Salonen. Electrical conductivity of quasi-two-dimensional foams. *Phys. Rev. E*, 91:042301, 2015.
- [98] W. Drenckhan and D. Langevin. Monodisperse foams in one to three dimensions. *Curr. Opin. Colloid Interface Sci.*, 15(5):341 – 358, 2010.
- [99] L. Saulnier, W. Drenckhan, P.-E. Larré, C. Anglade, D. Langevin, E. Janiaud, and E. Rio. In situ measurement of the permeability of foam films using quasi-two-dimensional foams. *Colloids Surf. A Physicochem. Eng. Asp.*, 473:32–39, 2015.
- [100] P. Marmottant and J.-P. Raven. Microfluidics with foams. *Soft Matter*, 5:3385–3388, 2009.

- [101] A. Huerre, V. Miralles, and M.-C. Jullien. Bubbles and foams in microfluidics. *Soft Matter*, 10:6888–6902, 2014.
- [102] G. Verbist, D. Weaire, and A. M. Kraynik. The foam drainage equation. *J. Phys.: Condens. Matter*, 8(21):3715–3731, 1996.
- [103] B. Haffner, Y. Khidas, and O. Pitois. Flow and jamming of granular suspensions in foams. *Soft Matter*, 10:3277–3283, 2014.
- [104] E. Rio, W. Drenckhan, A. Salonen, and D. Langevin. Unusually stable liquid foams. *Adv. Colloid Interface Sci.*, 205:74 – 86, 2014. Special Issue in honor of Bjorn Lindman.
- [105] F. Rouyer, C. Fritz, and O. Pitois. The sedimentation of fine particles in liquid foams. *Soft Matter*, 6:3863–3869, 2010.
- [106] S. Heitkam, Y. Yoshitake, F. Toquet, D. Langevin, and A. Salonen. Speeding up of sedimentation under confinement. *Phys. Rev. Lett.*, 110:178302, 2013.
- [107] T. Séon, J.-P. Hulin, D. Salin, B. Perrin, and E. J. Hinch. Buoyancy driven miscible front dynamics in tilted tubes. *Phys. Fluids*, 17(3):031702, 2005.
- [108] H. Caps, N. Vandewalle, A. Saint-Jalmes, L. Saulnier, P. Yazhgur, E. Rio, A. Salonen, and D. Langevin. How foams unstable on earth behave in microgravity? *Colloids Surf. A Physicochem. Eng. Asp.*, 457:392 – 396, 2014.
- [109] E. S. Basheva, D. Ganchev, N. D. Denkov, K. Kasuga, N. Satoh, and K. Tsujii. Role of betaine as foam booster in the presence of silicone oil drops. *Langmuir*, 16(3):1000–1013, 2000.
- [110] K. Koczó, J. K. Koczó, and D. T. Wasan. Mechanisms for antifoaming action in aqueous systems by hydrophobic particles and insoluble liquids. *J. Colloid Interface Sci.*, 166(1):225 – 238, 1994.